The MOSAiC Distributed Network: observing the coupled Arctic system with multidisciplinary, coordinated platforms

Benjamin Rabe[1*], Christopher J. Cox[2], Ying-Chih Fang[3], Helge Goessling[4], Mats A. Granskog[5], Mario Hoppmann[6], Jennifer K Hutchings[7], Thomas Krumpen[8], Ivan Kuznetsov[9], Ruibo Lei[10], Tao Li[11], Wieslaw Maslowski[12], Marcel Nicolaus[13], Don Perovich[14], Ola Persson[15], Julia Regnery[16], Ignatius Rigor[17], Matthew D. Shupe[18*], Vladimir Sokolov[19], Gunnar Spreen[20], Tim Stanton[21], Daniel M. Watkins[22], Ed Blockley[23], H. Jakob Buenger[24], Sylvia Cole[25], Allison Fong[26], Jari Haapala[27], Céline Heuzé[28], Clara J.M. Hoppe[29], Markus Janout[30], Arttu Jutila[31], Christian Katlein[32], Richard Krishfield[33], Long Lin[34], Valentin Ludwig[35], Anne Morgenstern[36], Jeff O'Brien[37], Alejandra Quintanilla Zurita[38], Thomas Rackow[39], Kathrin Riemann-Campe[40], Jan Rohde[41], William Shaw[42], Vasily Smolyanitsky[43], Amy Solomon[44], Anneke Sperling[45], Ran Tao[46], John Toole[47], Michel Tsamados[48], Jialiang Zhu[49], Guangyu Zuo[50]

[1] Alfred-Wegener-Institut Helmholtz Zentrum für Polar-und Meeresforschung, Bremerhaven, Germany

[2] NOAA Physical Sciences Laboratory (PSL), Boulder, USA

[3] Alfred-Wegener-Institut Helmholtz Zentrum für Polar-und Meeresforschung, Bremerhaven, Germany; Department of Oceanography, College of Marine Sciences, National Sun Yat-sen University, Kaohsiung, Taiwan

[4] Alfred-Wegener-Institut Helmholtz Zentrum für Polar-und Meeresforschung, Bremerhaven, Germany

[5] Norwegian Polar Institute, Fram Centre, Tromsø, Norway

[6] Alfred-Wegener-Institut Helmholtz Zentrum für Polar-und Meeresforschung, Bremerhaven, Germany

[7] Oregon State University, Corvallis, Oregon, USA

[8] Alfred-Wegener-Institut Helmholtz Zentrum für Polar-und Meeresforschung, Bremerhaven, Germany

[9] Alfred-Wegener-Institut Helmholtz Zentrum für Polar-und Meeresforschung, Bremerhaven, Germany

[10] Polar Research Institute of China, China

[11] College of Oceanic and Atmospheric Sciences, Ocean University of China, Qingdao, China; Pilot National Laboratory for Marine Science and Technology, Qingdao, China

[12] Alfred-Wegener-Institut Helmholtz Zentrum für Polar-und Meeresforschung, Bremerhaven, Germany

[13] Alfred-Wegener-Institut Helmholtz Zentrum für Polar-und Meeresforschung, Bremerhaven, Germany

[14] Thayer School of Engineering, Dartmouth College, Dartmouth, USA

[15] Cooperative Institute for Research in Environmental Sciences, University of Colorado; Physical Sciences Laboratory, National Oceanic and Atmospheric Administration, Boulder, USA

[16] Alfred-Wegener-Institut Helmholtz Zentrum für Polar-und Meeresforschung, Bremerhaven, Germany

[17] University of Washington, Seattle, USA

[18] Cooperative Institute for Research in Environmental Sciences, University of Colorado; Physical Sciences Laboratory, National Oceanic and Atmospheric Administration, Boulder, USA

[19] Arctic and Antarctic Research Institute, St. Petersburg, Russia

[20] University of Bremen, Institute of Environmental Physics, Bremen, Germany

[21] Naval Postgraduate School and Moss Landing Marine Laboratories, Monterey, USA

[22] Brown University, Providence, RI, USA; Oregon State University, Corvallis, OR, USA

[23] Met Office Hadley Centre, FitzRoy Road, Exeter, UK

[24] Alfred-Wegener-Institut Helmholtz Zentrum für Polar-und Meeresforschung, Bremerhaven, Germany

[25] Woods Hole Oceanographic Institution, Woods Hole, USA

[26] Alfred-Wegener-Institut Helmholtz Zentrum für Polar-und Meeresforschung, Bremerhaven, Germany

[27] Finnish Meteorological Institute, Helsinki, Finland

[28] Department of Earth Sciences, University of Gothenburg, Gothenburg, Sweden

[29] Alfred-Wegener-Institut Helmholtz Zentrum für Polar-und Meeresforschung, Bremerhaven, Germany

[30] Alfred-Wegener-Institut Helmholtz Zentrum für Polar-und Meeresforschung, Bremerhaven, Germany

[31] Alfred-Wegener-Institut Helmholtz Zentrum für Polar-und Meeresforschung, Bremerhaven, Germany; Finnish Meteorological Institute, Helsinki, Finland

[32] Alfred-Wegener-Institut Helmholtz Zentrum für Polar-und Meeresforschung, Bremerhaven, Germany

[33] Woods Hole Oceanographic Institution, Woods Hole, USA

[34] Polar Research Institute of China, China

[35] Alfred-Wegener-Institut Helmholtz Zentrum für Polar-und Meeresforschung, Bremerhaven, Germany

[36] Alfred-Wegener-Institut Helmholtz Zentrum für Polar-und Meeresforschung, Bremerhaven, Germany

[37] Woods Hole Oceanographic Institution, Woods Hole, USA

[38] Alfred-Wegener-Institut Helmholtz Zentrum für Polar-und Meeresforschung, Bremerhaven, Germany

[39] European Centre for Medium-Range Weather Forecasts (ECMWF), Bonn, Germany

[40] Alfred-Wegener-Institut Helmholtz Zentrum für Polar-und Meeresforschung, Bremerhaven, Germany

[41] Alfred-Wegener-Institut Helmholtz Zentrum für Polar-und Meeresforschung, Bremerhaven, Germany

[42] Naval Postgraduate School and Moss Landing Marine Laboratories, Monterrey, USA

[43] Arctic and Antarctic Research Institute, St. Petersburg, Russia

[44]Cooperative Institute for Research in Environmental Sciences, University of Colorado; Physical Sciences Laboratory, National Oceanic and Atmospheric Administration; Boulder, USA

[45]Alfred-Wegener-Institut Helmholtz Zentrum für Polar-und Meeresforschung, Bremerhaven, Germany

[46]Alfred-Wegener-Institut Helmholtz Zentrum für Polar-und Meeresforschung, Bremerhaven, Germany

[47]Woods Hole Oceanographic Institution, Woods Hole, USA, Woods Hole, USA

[48]Centre for Polar Observation and Modelling, Earth Sciences, UCL, London, UK

[49]College of Oceanic and Atmospheric Sciences, Ocean University of China

[50]College of Electrical and Power Engineering, Taiyuan University of Technology, Taiwan

21

22 *corresponding authors: benjamin.rabe@awi.de, matthew.shupe@noaa.gov

Abstract

Central Arctic properties and processes are important to the regional and global coupled climate system. The Multidisciplinary drifting Observatory for the Study of Arctic Climate (MOSAiC) Distributed Network (DN) of autonomous ice-tethered systems aimed to bridge gaps in our understanding of temporal and spatial scales, in particular with respect to the resolution of Earth system models. By characterizing variability around local measurements made at a Central Observatory the DN covers both the coupled system interactions involving the ocean-ice-atmosphere interfaces as well as three-dimensional processes in the ocean, sea ice, and atmosphere. The more than 200 autonomous instruments ("buoys") were of varying complexity and set up at different sites mostly within 50 km of the Central Observatory. During an exemplary midwinter month, the DN observations captured the spatial variability of atmospheric processes on sub-monthly time scales, but less so for monthly means. They show significant variability in snow depth and ice thickness, and provide a temporally and spatially resolved characterization of ice motion and deformation, showing coherency at the DN scale but less at smaller spatial scales. Ocean data show the background gradient across the DN as well as spatially dependent time variability due to local mixed layer sub-mesoscale and mesoscale processes, influenced by a variable ice cover. The second case (May–June 2020) illustrates the utility of the DN during the absence of manually obtained data by providing continuity of physical and biological observations during this key transitional period. We show examples of synergies between the extensive MOSAiC remote sensing observations and numerical modelling, such as estimating the skill of ice drift forecasts and evaluating coupled system modelling. The MOSAiC DN has been proven to enable analysis of local to mesoscale processes in the coupled atmosphere-ice-ocean system and has the potential to improve model parameterizations of important, unresolved processes in the future.

1. INTRODUCTION

a. Arctic processes, global climate models and MOSAiC

The Arctic is a region of prime importance for ongoing global change, showing significant sea ice retreat (Lindsay and Schweiger, 2015; Meredith et al., 2019; Intergovernmental Panel on Climate change, 2022), near-surface air temperature rising at more than twice the global rate (e.g., Rantanen et al., 2022), and "Atlantification" in the Eurasian part of the Arctic Ocean (e.g., Polyakov et al., 2017; Ingvaldsen et al., 2021). The largely enclosed nature of the basin and the extensive continental shelves make the Arctic Ocean much smaller in both area and volume than the Indian, Atlantic and Pacific oceans, yet it receives on the order of 10% of the world's continental runoff (Haine et al., 2015; GRDC, 2023). Moreover, the Arctic Ocean is closely linked to the adjacent oceans and seas, where it can have potentially profound impact on regional or global ocean circulation (e.g., Häkkinen, 1999; Haak et al., 2003) and atmospheric temperatures (e.g., Wu et al., 2013) at lower latitudes, and, ultimately, global climate (e.g., Koenigk et al., 2007; Rennermalm et al., 2007).

Basin-wide budgets and circulation patterns are determined not only by basin-scale forcing but also by many processes that play out from mesoscales (von Appen et al., 2022, and references therein) to small-scale turbulence (Rippeth and Fine, 2022, and references therein) and further to the (diffusive) molecular scale (Rudels et al., 2009; Shibley et al., 2017). The regionally varying seasonal and perennial sea ice cover and surface snow add challenges to understanding the regional coupled climate system. Feedbacks among the atmosphere, sea ice and snow, and liquid ocean are complex, varying in all three dimensions and in time. The vertical column is particularly important, as it allows radiation and turbulence to directly transport energy, mass, and other constituents across different layers in the coupled system (e.g., Sirevaag et al., 2011; Tjernström et al., 2014). Lateral processes, including long-range atmospheric transport, sea ice melt and freeze, as well as frontal dynamical processes and eddies in the ocean and atmosphere, boundary layer turbulence, and cloud macrophysical and microphysical properties (e.g., Timmermans et al., 2012; Jonassen et al., 2020; George et al., 2021), lead not only to lateral but also to vertical fluxes. This combination of lateral and vertical fluxes has been shown to strongly link atmosphere-ice-ocean features such as cloud liquid water content and ice growth rates at the ice-ocean interface (Persson et al., 2017). Both local small-scale processes as well as mesoscale features are highly heterogeneous in space and time, across the disciplines of physics, chemistry and biology (e.g., d'Ovidio, 2010; Levy and Martin, 2013; Mahadevan, 2016). Hence, how well any single point in space and time may represent the conditions across a larger domain, such as

80 an ocean basin or a climate model grid box, is not clear. Even a time series at one point in space
81 or a quasi-synoptic survey along a single line may not capture all of the important variability. A
82 spatial network of sensors measuring key variables at high temporal resolution is needed.
83
84 The Multidisciplinary drifting Observatory for the Study of Arctic Climate (MOSAiC) set out to
85 measure a multitude of variables at a variety of spatial scales in the coupled atmosphere-ice-
86 ocean system along the transpolar drift throughout a whole annual cycle, with the ultimate aim to
87 enhance our understanding of regional and local processes and improve coupled climate
88 modeling. From October 2019 to July 2020 the German icebreaker RV *Polarstern* (Alfred-
89 Wegener-Institut Helmholtz-Zentrum für Polar- und Meeresforschung, 2017) served as the base
90 of operations and was moored to an ice floe, drifting across the Eurasian basin from north of the
91 Laptev Sea to Fram Strait. The vessel was then relocated to a different ice floe in the central
92 Arctic during the final phase of the experiment in August and September 2020, capturing the
93 autumn freeze-up. The Central Observatory of the experiment consisted of many fixed
94 installations on RV *Polarstern* itself, as well as a wide array of sampling and measurement
95 activities on the main ice floe within about 2 km of the vessel. Further details on the disciplinary
96 work can be found in overviews by the scientific teams, covering the atmosphere (Shupe et al.,
97 2022), physical oceanography (Rabe et al., 2022), sea ice and snow (Nicolaus et al., 2022), the
98 ecosystem (Fong et al., n.d.), and biogeochemistry (overview publication expected in this special
99 feature, led by E Damm). These works also contain details on the scientific conceptual design,
100 logistics and legs of the expedition that we do not detail here.
101
102 *b. Gaps in knowledge and community needs*
103 Despite numerous efforts to observe and model the Arctic coupled atmosphere-ice-ocean system
104 there are significant gaps in our knowledge of the relevant processes (Meredith et al., 2019). Prior
105 to MOSAiC, much observational data was lacking for the atmosphere (Bourassa et al., 2013;
106 Shupe et al., 2022), the sea ice and snow (Nicolaus et al., 2022), and the ocean (Rabe et al.,
107 2022; Weingartner et al., 2022). The horizontal grid resolution in current global climate or Earth
108 system models used for multi-decadal simulations ranges from 8–250 km, typically 8–100 km in
109 the ocean and coarser in the atmosphere, 25–250 km (Haarsma et al., 2016; Roberts et al., 2019).
110 Numerical Weather Prediction and regional climate and ocean-ice models reach resolutions with
111 a spacing of less than 10 km (Rackow et al., 2019), with some approaching 1 km, in both the
112 atmosphere (Wedi et al., 2020), the sea ice and the ocean (Wang et al., 2020). Increasingly, such
113 models are resolving variability at scales that are finer than the typical grid boxes of multi-decadal

114 global climate model simulations outlined above, and hence require process-level observations
115 at fine scales. Key variabilities include mesoscale ocean eddies (e.g., Wang et al., 2020) on scales
116 of around 5–10 km (e.g., Nurser and Bacon, 2014; Sein et al., 2017); sea ice thickness,
117 deformation, and roughness (e.g., Bouchat et al., 2022; Hutter et al., 2022a); snow depth,
118 mesoscale variability of cloud structure and associated dynamics, and mesoscale wind variations;
119 and variability of surface energy and momentum fluxes. These fluxes are dependent on the
120 variability of clouds and snow/ice surface characteristics. An improved representation of these,
121 often multidisciplinary, processes, either through increased model resolution or advanced
122 parameterizations, is critical for reducing uncertainty in models and their predictions of Arctic
123 climate change (Maslowski et al., 2012; Jin et al., 2018; Roberts et al., 2019; Clement Kinney et
124 al., 2022; Jung et al., 2022; Heuzé et al., 2023).
125
126 Autonomous observations have gained importance in the Arctic Ocean in recent decades and
127 bring the potential to fill many of the observational needs. The development of technologically
128 advanced ice-tethered systems, capable of measuring and sending data while drifting with sea
129 ice, has closed significant gaps in seasonal and regional observing. Examples of these kinds of
130 instrument systems are the JAMSTEC Compact Arctic Drifter (J-CAD; Hatakeyama et al., 2001),
131 Metocean Polar Ocean Profiling System (POPS; Kikuchi et al., 2007), Woods Hole
132 Oceanographic Institution Ice-tethered Profiler (WHOI-ITP; Toole et al., 2011; Krishfield et al.,
133 2008), Naval Postgraduate School Autonomous Ocean Flux Buoys (AOFB; Stanton et al., 2012),
134 Ice-Atmosphere Arctic Ocean platforms (IAOOS; Koenig et al., 2016; Athanase et al., 2019),
135 several kinds of sea ice mass balance buoys (Richter-Menge et al., 2006; Jackson et al., 2013;
136 Planck et al., 2019; Lei et al., 2022a), and snow buoys (hereafter "Snow Buoys"; Nicolaus et al.,
137 2021a). An overarching coordinating effort, the International Arctic Buoy Programme (IABP; Rigor
138 et al., 2002; IABP, 2023; Ermold and Rigor, 2023), has been supporting the basin-wide
139 deployment of autonomous ice-tethered instruments across the whole Arctic Ocean region, which
140 also includes regionally focused efforts.
141
142 *c. The MOSAiC Distributed Network (DN)*
143 One of the unique ideas laid out in the MOSAiC Science and Implementation plans (MOSAiC
144 Consortium, 2016; 2018) was to observe a drifting 'unit' of sea ice, approximately the size of a
145 typical model grid box, to quantify the "sub-grid scale" variability and the representativeness of
146 individual measurements throughout the atmosphere-ice-ocean column. This concept specifically
147 motivated the design of the MOSAiC DN, where numerous autonomous measurement systems

were installed within a radius of a few tens of kilometers of RV *Polarstern* to obtain continuous observations of key variables that were also observed at the Central Observatory (Shupe et al., 2022; Nicolaus et al., 2022; Rabe et al., 2022). This DN has enabled observations to:

- examine heterogeneity and spatial variability at scales smaller than global climate model grid boxes to assess the representativeness of local measurements for regional processes and provide essential perspectives on upscaling of key measurements and process understanding;
- link processes across key interfaces of the coupled system;
- explore the influences of large-scale forcing on local processes, including the basin-scale variability in atmospheric forcing, sea ice-thickness distribution, ocean-mixed layer depth, and more, by measuring local spatial gradients of properties and capturing floe-scale ice and snow variability; and
- study two-dimensional and three-dimensional processes and their evolution in time.

These overarching concepts lend themselves to addressing a number of specific scientific questions. For example, what role do transient processes play in ocean vertical mixing, how do ice dynamics contribute to the temporal evolution of the ice thickness distribution and the heat flux between ocean and atmosphere, or how is surface momentum transfer shaped by mesoscale atmospheric divergence? In addition to focusing on local and regional processes around the drifting MOSAiC setup, the DN autonomous observing systems also helped to link the MOSAiC observations to a pan-Arctic network of autonomous buoy observations coordinated by the International Arctic Buoy Programme.

This work gives a descriptive account of the performance of the MOSAiC DN and shows the added value by examples of specific scientific cases, in particular with respect to the spatial variability in the observations. In Section 2, we summarize the approach and implementation of the DN, also in the context of prior work. We detail its performance and show exemplary results and analysis in Section 3. Section 4 provides a summary and discussion of the results in Section 3, further highlighting synergies with remote sensing measurements and numerical modelling studies. We conclude with an overall assessment of the MOSAiC-DN approach and its resultant implications for scaling in observations and numerical models.

2. METHODS: Observational approach and instrumentation

In this section, we give a detailed overview of the MOSAiC DN of autonomous instrument platforms ("buoys"), from the initial concept and planning, through the description of the different

181 instruments and platforms, to the final implementation. While the general approach covers all
182 implementations of this DN, we mainly describe the initial setup that occurred from October
183 2019 into July 2020. A second, less extensive network was implemented after relocation of the
184 observatory to the central Arctic in August 2020.
185
186 *A. Overall concept of the DN: scales and layout*
187 The MOSAiC DN covered different scales of variability inherent to the individual sub-systems of
188 the Arctic Ocean:
189   • In the atmosphere, mesoscale variability occurs at scales from approximately 2 km up to
190   several 100 km, representing spatial variability in storm structure, wind patterns, cloud
191   formation/structure, precipitation regimes, and other related processes.
192   • Sea ice and snow properties and processes can vary on similar scales as the atmosphere,
193   but also have key modes of inter-floe versus intra-floe variability that can manifest on
194   scales much smaller than 5 km.
195   • Ocean mesoscale variability is expected to be around 5–10 km, the size of the local first-
196   mode baroclinic Rossby radius. Submesoscale variability is expected to be on the order
197   of 1 km.
198 Importantly, the DN design needed to support observations that would link across these various
199 scales in the different subsystems to enable the study of coupled processes. The optimal
200 observation of isotropic anomalies uses a radially outward-oriented network of nodes (Chan et
201 al., 1996). During the installation phase at the beginning of the MOSAiC field experiment, we
202 implemented several of those nodes (hereafter referred to as "sites") arranged in horizontal circles
203 at different radii from the Central Observatory. To resolve the above-mentioned scales, we initially
204 established 3 large (L) sites, 9 medium (M/LM) sites, and 86 single buoy geographic position (P)
205 sites in the DN. These sites were planned to track cascading scales of 2 km, 5 km, 10 km and 15
206 km away from the Central Observatory, with a few additional units at even larger scales to link
207 with the International Arctic Buoy Programme network ("Extended Network" in Figure 1); details
208 are given in the supplemental material (Text S1 and Figures S1 and S2). However, the ice
209 conditions and deployment opportunities required a much more flexible and diverse layout (Figure
210 1), where several sites were placed at greater distance due to the lack of ice floes sufficiently thick
211 and close to the Central Observatory. The observations of the ocean and atmosphere from ice-
212 tethered platforms, however, allowed coverage of scales beyond the spacing of sites and
213 instruments due to measuring quasi-steady spatial variability while drifting with the sea ice. The
214 final layout was influenced by additional constraints, such as not deploying too many buoys in a

215 "logistics" corridor used for approaching supply vessels (see Text S1 and Figure S1), and the
216 number of buoys the consortium was able to provide for deployment. Several fully autonomous
217 instruments were also deployed at the Central Observatory along with all of the attended
218 instrumentation at that site, making the Central Observatory one of the buoy sites within the DN,
219 and allowing direct comparisons between DN instrumentation and Central Observatory
220 instruments not otherwise deployed in the DN.

221 This DN had to be dismantled as it approached the ice edge in Fram Strait at the end of July
222 2020, with a few buoys still working until 2022. In August 2020, a new buoy array was established
223 in and around a new Central Observatory in the central Arctic near 87°N, though it was less
224 extensive and featured only a small subset of the instrumentation of the first DN. The second,
225 "mini" DN (hereafter termed "mDN") is briefly described in Text S2 which also provides references
226 for further details. Here, we focus on the first DN (simply referred to as "DN").

227

228 **Figure 1. Actual layout of the Distributed Network after completing all initial deployments**
229 **on October 22, 2019.**

230

231 *b. Platforms and Instrumentation in the DN*
232 The measurement concept of the DN is based on more than 30 different types of autonomous
233 buoy platforms, as summarized in Table 1. Each type is unique with respect to technical
234 specifications, measured variables, vertical and temporal resolution and data concept (formats,
235 transmission, storage and data flow). In total, 234 buoys were deployed on, in, and under the sea
236 ice during MOSAiC (Figure 2). Here we briefly describe the general characteristics of the different
237 platform types. The list is sorted by the main sensors on each platform associated with
238 atmospheric, snow and sea ice, and oceanographic measurements.

239

240 Atmospheric conditions were monitored with Atmospheric Surface Flux Stations (ASFS; Cox et
241 al., 2023a; Figure 2a), measuring all components of the surface energy and momentum budgets,
242 including up/down shortwave and longwave radiation, eddy-covariance based turbulent-sensible
243 and latent-heat fluxes and momentum flux, and the snow-ice conductive heat flux derived from
244 flux plates. These stations also measured near-surface air pressure, temperature, relative
245 humidity, winds, radiometrically derived surface skin temperature, localized relative surface height
246 (used to derive snow depth), and geographic position and heading. As the most complex surface
247 stations, they were maintained whenever possible during their drift. The Central Observatory
248 meteorological installation included a 3-level meteorological tower that measured a set of

11

249 variables similar to the Atmospheric Surface Flux Stations (Shupe et al., 2022; Cox et al., 2023a).

250 Wind measurements from the array of three L sites and the Central Observatory have been used

251 to estimate low-level (approximately 3.8 m height) atmospheric divergence on an approximate 25

252 km scale. In addition, several other buoy types measured air temperature, radiative fluxes, and

253 barometric pressure, but without any maintenance (e.g., Figure 2b, d and i).

254

255 Snow and sea ice mass balance were measured with different kinds of ice mass balance buoys

256 (IMBs, Figure 2b, d, e, p and r), including thermistor strings providing profiles of temperature and

257 thermal conductivity with a resolution of 0.02 m (Jackson et al., 2013), seasonal IMBs (Planck et

258 al., 2019), and Snow Buoys that measure relative changes in snow depth (Nicolaus et al., 2021a;

259 Figure 2c). Measurements of solar irradiance above and below the sea ice, including derivations

260 of albedo and transmittance, were performed with different radiation stations (Figure 2b and q).

261 Some radiation stations and IMBs also included measurements of additional bio-physical

262 variables of the uppermost ocean. Sea ice drift and deformation was recorded by various types

263 of geographic position-tracking buoys, including ice-Surface Velocity Profilers (iSVP; Figure 2o),

264 ice trackers and the geographic position data provided by most other buoys. Some of these units

265 reported barometric pressure and surface temperature. In addition, most of the units floated,

266 which increased their chances of surviving ice deformation and complete melt out. Most position-

267 tracking buoy and Snow Buoy data were transmitted to the Global Telecommunication System

268 (GTS) by the World Meteorological Organization (WMO) and thus were available for near-real

269 time analysis and inclusion in numerical weather forecasting. Surface photography was obtained

270 by digital cameras on various units.

271

272 The backbone of oceanographic observations are measurements of conductivity, temperature,

273 and pressure (Conductivity Temperature Depth, hereafter referred to as "CTD") at various vertical

274 levels and in different configurations, with salinity and depth derived directly from those variables.

275 Woods Hole Ice-tethered profilers (Krishfield et al., 2008; Toole et al., 2011; 2016; Cole et al.,

276 2015; Figure 2j), installed at the L sites, were among the most complex systems. Some of these

277 profilers provided not only temperature and salinity, but also three-dimensional velocity, dissolved

278 oxygen and bio-optical variables of the water column from 760 m to 7 m depth at a vertical

279 resolution of about 1 m (1 dbar) at time intervals of a few hours to 1.5 days. The bio-optical

280 variables included optical backscatter and fluorescence at different wavelengths related to the

281 concentration of chlorophyll *a* and chromophoric dissolved organic matter (CDOM). Similar

282 systems, the Drift-Towing Ocean Profiler (DTOP; e.g., Li et al., 2021a; Ocean Univeristy of China,

283   2024), covered most of these variables from under the ice to about 120 m depth. Other systems
284   carried CTD sensors at fixed depths (e.g., Figure 2l and h) measuring at time intervals of a few
285   minutes (Hoppmann et al., 2022a). A few of those systems also carried sensors for bio-optical
286   variables, similar to those on the Woods Hole Ice-tethered Profilers, measuring close to the ice
287   bottom. Eddy-correlation flux systems as part of the Autonomous Ocean Flux Buoys (e.g., Shaw
288   et al., 2008; Stanton et al., 2012, Lee et al., 2022; Rabe et al., 2022; Figure 2m) directly observed
289   the vertical fluxes of momentum, heat and salt in the ocean just underneath the ice, with
290   Autonomous Ocean Flux Buoys making concurrent high-resolution profiles of horizontal current
291   velocity in the upper 60 m. These profiles included the ocean mixed layer and the upper halocline
292   (pycnocline) during much of the expedition, as well as dissipation-based thermal diffusivity and
293   heat flux measurements at 50 m depth within the pycnocline. The combined, distributed
294   deployment of these systems covered a depth range from just underneath the ice down to about
295   760 m as well as temporal scales of a few seconds to days.

296

297   The Unmanned (uncrewed) Ice Station combined measurements from all realms: the atmosphere,
298   sea ice and snow, and the ocean (Lei et al., 2022a; Figure 2d). Compared with the traditional sea
299   ice mass balance buoy, the special design of this buoy is to increase the observations of multi-
300   spectral shortwave radiation of five layers within the ice to obtain the light attenuation coefficients
301   of sea ice with different textures and to extend the measurements downward, focusing on the
302   oceanic mixed layer, obtaining temperature and salinity at six layers with depths of 5–40 m.

303

304   *c. Sites: Distribution of instruments within the DN*
305   The three L sites contained the most comprehensive measurements of the atmosphere-ice-ocean
306   system in the DN, including biological and biogeochemical variables in both water and sea ice
307   (Table 1, Figure 2 and Table S1). They provided measurements in different local conditions (e.g.,
308   ice thickness, floe size and shape) and put the observations at the Central Observatory into
309   context with the remainder of the region covered by the DN. The installation of Atmospheric
310   Surface Flux Stations together with Autonomous Ocean Flux Buoys, Woods Hole Ice-tethered
311   Profilers and IMBs enables a full characterization of the energy and momentum transfer across
312   the coupled atmosphere-ice-ocean system. Deploying Atmospheric Surface Flux Stations in the
313   DN afforded the opportunity to collect data suitable for examining the spatial variability in surface
314   energy transfer related, for example, to differences in sea ice or snow thickness. At L3, the
315   Unmanned (uncrewed) Ice Station was deployed, featuring various ice, ocean and air
316   measurements (for details see above). Several IMBs of various types (SIMB3, SIMBA, IMBflex

317   and IMB combined with radiation stations; see Table 1) and Snow Buoys were deployed to
318   monitor the seasonal changes of ice thickness, snow depth and vertical temperature profile
319   through the snow-covered ice layer across a range of initial ice thicknesses. Some of these buoys
320   also measured biooptical and biogeochemical variables. The different buoy types were distributed
321   within individual sites according to the scales detailed in Section 2a. For example, while one ocean
322   profiler and one Atmospheric Surface Flux Station were sufficient to capture the conditions above
323   and below the ice at an individual site, that site often had multiple IMBs to represent intra-floe
324   variability in snow and sea ice.
325
326   The 9 M sites aimed to observe ocean mesoscale variability in the upper approximate 100 m, as
327   well as snow and ice thickness, temperature, and basic local meteorological conditions. A few
328   systems also recorded biological and biogeochemical variables. The main platforms at the M sites
329   were a Snow Buoys and a variety of IMBs, and Salinity Ice Tether buoys measuring ocean
330   properties with CTD sensors at selected depths (Table 1, Figure 2). Several M sites additionally
331   had Drift-Towing Ocean Profilers. The scales covered by the M sites are suitable to validate the
332   ice growth rate derived from satellite altimeter observations (e.g., Koo et al., 2021) and climate or
333   sea ice forecast models (e.g., Pithan et al., 2023). The LM site was equipped differently than the
334   other 8 M sites and the 3 L sites, featuring upper-ocean CTD measurements only close to the ice
335   and additional instrumentation for radiation, more complex biophysical measurements and a
336   sediment trap, in addition to IMB and Snow Buoys, as well as various non-telemetered devices.
337   This site was accessible from the Central Observatory most of the time and was visited frequently
338   for manual measurements and sampling, such as coring first-year and second-year ice. The LM
339   site is counted as an M site throughout this paper.
340
341   The 86 P sites of the DN were distributed to capture ice deformation across the region around the
342   Central Observatory. The priorities for placing P sites were to: (i) ensure that horizontal sea ice
343   deformation was monitored in the 5 km surrounding the Central Observatory and L sites; (ii)
344   capture deformation on 10, 20 and 40 km scales around the Central Observatory; and (iii) monitor
345   deformation around the M sites. In addition, a few P site buoys were deployed along the
346   icebreaker transits, several hundreds of kilometers away from the Central Observatory, to capture
347   large-scale characteristics of sea ice kinematics and to obtain additional barometric pressure
348   data. The platforms on the P sites consisted of different kinds of position-tracking buoys, and four
349   IMBs (SIMBA, Table 1; Figure 2).
350

Figure 2. Photographs of selected autonomous platforms (buoys) deployed in the two implementations of the Distributed Network.

Table 1. Types of autonomous buoy systems used during MOSAiC.

d. Implementation of the main Distributed Network

The initial setup of the DN was accomplished in 12 days (October 5–16, 2019) from the Russian ice breaker *Akademik Fedorov*, which accompanied RV *Polarstern* during the initial MOSAiC setup phase. Details of this operation can be found in the cruise report by Krumpen and Sokolov (2020). During this time all 3 heavy equipment L sites, 8 of the 9 M sites and various geographic position tracking P sites were installed. The L sites required local icebreaker support for deployment and were revisited using a helicopter during the drift. Revisits allowed instrument maintenance and additional contextual measurements and sampling. The M sites were mostly deployed with helicopter support, and the P sites only by helicopter. These installations were a significant logistical challenge because of the very thin first year ice conditions, the limited space onboard the vessel, the short time window to complete deployment before loss of daylight and increasing sea ice formation. This task was achieved by having concurrent science teams prepare L site instrumentation in the large forward hold of *Akademik Fedorov*, while the rear of the ship was used to stage the M site and position-tracking buoy systems. A separate science team located the best available ice floes using high-resolution satellite-borne Synthetic Aperture Radar (SAR) imagery and helicopter surveys integrated with the M and P site instrument deployments. In addition, the availability of predictive model results (Krumpen et al., 2020) was of great benefit. Installations on the ice were performed by instrumentation groups, including early-career researchers from the onboard MOSAiC school and journalists who actively assisted in the deployments. This strategy allowed each L site (and parts of the M and P sites) to be surveyed and instrumented in less than 1.5 days. Parts of the deployment operations are sketched as digital drawings in Krueger and Rackow (2020). Concurrent to L site operations next to the ship, one of the two contracted MI-8 helicopters on *Akademik Fedorov* was employed to deploy instruments at the M and P sites.

In addition to the buoy installations, visual ice observations were carried out from the bridge by a group of three specially trained ice observers onboard *Akademik Fedorov*. Detailed descriptions of the methodology and protocols applied are provided in Alekseeva et al. (2019) and AARI (2011), all congruent with the WMO Sea Ice Nomenclature (2017). At each L site, a full floe survey

15

385 was initiated by the science team and early-career researchers from the MOSAiC school. This
386 survey included snow thickness measurements and ground-based electromagnetic induction
387 surveys of ice thickness. In addition to the three L sites, extensive ice and snow thickness surveys
388 were performed at M4 and M7 located within approximately 20 km of the Central Observatory.
389 Details about the initial ice thickness and snow depth at the individual L sites are given in Krumpen
390 and Sokolov (2020, their Chapter 2.1) and in Krumpen et al. (2021).

391

392 The deployent and conditions during the setup resulted in different scales covered by the DN, as
393 shown in the map shortly after deployment (Figure 1). The L sites were at a distance similar to
394 that planned and represent a compromise between logistically maintainable buoy sites (regular
395 helicopter visits every few weeks), sufficient distance from the Central Observatory to measure a
396 variety of local conditions, and the ability to capture mesoscale variability in the atmosphere. Due
397 to lack of sufficiently thick ice floes close to the Central Observatory, the M sites ended up almost
398 an order of magnitude farther away from the Central Observatory than planned. Section 4a
399 includes a brief discussion of the consequences of observable scales.

400

401 During spring, helicopter deployment of additional buoys filled in gaps that had appeared in the
402 DN and added another 15 km-diameter ring of position-tracking buoys around the Central
403 Observatory. One position-tracking buoy was also placed about 80 km to the east of the Central
404 Observatory, allowing synoptic scale drift and deformation monitoring. While RV *Polarstern* was
405 away from the Central Observatory between mid-May and mid-June 2020 to facilitate a personnel
406 rotation, the L2 Atmospheric Surface Flux Station (#30) operated from the Central Observatory to
407 collect measurements in place of the temporarily decommissioned atmospheric installations there
408 (at "Met City"; see Shupe et al., 2022; Cox et al., 2023a). In late April, Atmospheric Surface Flux
409 Station #50 (originally from L3) was installed at the Central Observatory and operated there for
410 much of the time until the end of July.

411

412 Although ice dynamics damaged several buoys during the drift, requiring additional maintenance
413 where possible (e.g., Figure 3a), the majority of the DN was recovered in August 2020. The three
414 L sites (L1–L3), LM, M1 and M3 were recovered by RV *Polarstern* between August 1 and August
415 7. In addition, M4, M5, and M6 were recovered by *Akademik Tryoshnikov*, which supported the
416 rotation of personnel and equipment during much of August. The recovery included dismantling
417 both broken units and still-active devices. All ice-tethered units were close to the end of their
418 functionality in the broken and melting ice pack in Fram Strait; for example, a Woods hole Ice-

419 tethered Profiler and a Snow Buoy shown in Figure 3b and c, respectively. Some floating systems
420 (mostly position-tracking buoys) continued measurements and transmitted data from the North
421 Atlantic Ocean into summer 2022. All buoy deployments with sites, dates and labels are given in
422 Table S2.
423
424 **Figure 3. Photographs of conditions during recovery of the Distributed Network platforms**
425 **in 2020.**
426
427 *e. Methodological comparison to prior drift efforts*
428 Spatially distributed autonomous measurements have been made as part of particular regional
429 and temporally limited field campaigns, including, e.g., the Surface Heat Budget of the Arctic
430 (SHEBA; Perovich et al., 1999; Andreas et al., 1999; 2010b; Perovich and Elder, 2002; Uttal et
431 al., 2002; Shaw et al., 2009), the Tara drift (Gascard et al., 2008), AIDJEX (Untersteiner et al.,
432 2009) and the 2015 Norwegian young sea ICE (N-ICE2015; Itkin et al., 2017; Granskog et al.,
433 2018). Further efforts, such as the Marginal Ice Zone program in the Canada Basin (Lee et al.,
434 2017) or the "Switchyard" in the central Arctic (SWITCHYARD, 2023; see also Falkner et al.,
435 2005), had a strong focus on specific processes in selected regions. The MOSAiC approach
436 differs methodologically from previous efforts insofar as its DN included not only more
437 comprehensive observing systems but also covered spatial scales designed to resolve the
438 mesoscale in the ocean and the lower end of the mesoscale in the atmosphere. In addition, the
439 network spanned a greater variety of ice thicknesses and operated during a full year. During
440 SHEBA, comprehensive autonomous observing systems were distributed within about 3 km
441 distance from a Central Observatory, consisting of stations for atmospheric variables and fluxes
442 as well as ice and snow mass balance (Perovich et al., 1999; Andreas et al., 1999; 2010a; 2010b;
443 Perovich and Moritz, 2002); comprehensive ocean observations were only carried out at the
444 Central Observatory. Another example is N-ICE2015, where 42 autonomous systems were
445 located within 5–100 km from the ship, but the majority were ice mass balance and ice position-
446 tracking buoys (Itkin et al., 2017), without any distributed ocean observations. The Marginal Ice
447 Zone Project (https://apl.uw.edu/project/project.php?id=miz) distributed different atmosphere-ice-
448 ocean observing systems across several hundred kilometers in the central Canada Basin,
449 synoptically covering a larger area with measurements but with lower effective spatial resolution
450 than the MOSAiC DN. Thus, the MOSAiC DN combined the scales covered with the multitude of
451 instrumentation in an unprecedented way, with the largest deployment of ice-tethered position-

452 tracking buoys to date, over scales capturing individual active leads up to the kinematic response

453 to synoptic weather patterns (see Watkins et al., 2023).

454

3. Results

456 We illustrate the results that can be obtained from the DN, first briefly outlining the performance

457 and drift tracks of the whole network for the full duration of MOSAiC. We then show examples of

458 the coupled-system observations during a period in winter and a period in early summer; the

459 former represents a little-observed season in the central Arctic, while the latter covers the period

460 when the ship and all personnel had left the MOSAiC domain leaving only autonomous

461 observations. Aspects of the full seasonal cycle of specific variables have been analyzed

462 elsewhere (e.g., Lei et al., 2022a; Nicolaus et al., 2022; Rabe et al., 2022; Bliss et al., 2023; Itkin

463 et al., 2023), and a detailed description is beyond the scope of this overview paper. We do not

464 detail the results of the mDN in this work either and refer, instead, to the analyses already

465 published or expected to be submitted (e.g., Katlein et al., 2020; Flores et al., 2023). All

466 times/dates are given in UTC.

467

468 *a. Operation and drift tracks of the DN*

469 Figure 4 shows that all DN sites generally followed the drift of the Central Observatory (see Shupe

470 et al., 2020, their Figure 2). Text S3 and Table S3 detail the source of each position track defining

471 the individual DN sites. The life cycle of each buoy is detailed in Figure S6. Figure 5 shows that

472 the DN drifted with the transpolar drift, crossed Fram Strait and drifted into the Greenland Sea.

473 The transpolar drift was faster than expected, generally faster than the previous 15 years,

474 including the N-ICE2015 drift (see Section 2e); only one year had faster drift speeds in Fram Strait

475 (Krumpen et al., 2021; Dethloff et al., 2022). After the buoys came close to the edge of the

476 marginal ice zone in the Greenland Sea in August, 2020, those buoys that were not recovered

477 continued to drift, some circulating through the sea ice over the Greenland shelf and some exiting

478 the marginal ice zone into open water (Watkins et al., 2023).

479

480 **Figure 4. Drift tracks of the main sites of the Distributed Network.**

481

482 During the DN drift (Figure 5), the original relative distribution remained approximately intact for

483 the entire winter drift across the central Arctic, even though deformation on various scales within

484 the DN (see Section 3c) led to damage of some of the instrumentation (e.g., Figure 3a). Several

18

485 snapshots of L3 during mid-winter (Figure 6) show that significant deformation took place during
486 January and February. In particular, a large crack crossed the site and subsequently developed
487 into a pressure ridge that destroyed several of the nearby buoy systems (see Figure 6). L1
488 suffered deformation during late November/early December and late February, whereas L2 was
489 more stable. Further, ice surface roughness increased overall through April and May 2020 (von
490 Albedyll et al., 2022), and significant melting ensued after late May. As the DN approached the
491 northern end of Fram Strait in early May, the DN site distribution began to strain along a south-
492 southwest to north-northeast line, which became more distinct as it passed through Fram Strait
493 in June and July. The overall timing of the drift has been analyzed in Dethloff et al. (2022) and is
494 discussed further in Section 4a.

495

496 **Figure 5. Evolution of the Distributed Network from mid-October 2019 to late July 2020.**

497

498 **Figure 6. Surface elevation maps of site L3 in mid-winter from airborne laser scanner**
499 **observations.**

500

501 To illustrate DN observations during the Arctic winter, in Sections 3b to 3d, we show data from
502 various buoys, descriptively identifying vertical coupling and three-dimensional spatial features
503 associated with different physical processes. We focus on a 30-day period from December 20,
504 2019, to January 19, 2020, when the DN drifted primarily from southeast to northwest, with
505 deviations from the almost-straight track near the beginning and the end (Figure 7).

506

507 **Figure 7. Geographic position of sites within the Distributed Network from late December**
508 **to late January.**

509

510 *b. Wintertime variability in the atmosphere and feedback with sea ice, snow and ocean*
511 Some meteorological processes are associated with transient atmospheric forcing, such as
512 clouds or synoptic/mesoscale variability, occurring on scales that are set by the Rossby radius of
513 deformation, which is close to the scale of the DN measurements. Other processes are associated
514 with heterogeneity of the sea ice, which has smaller spatial length scales (see Section 3c).

515

516 Figure 8 shows the atmospheric conditions at the 4 sites in the DN that featured detailed,
517 temporally high-resolution atmospheric observations during this 30-day mid-winter period, when
518 the distances from each site to the Central Observatory did not vary in time by more than 1 km.

519 The near-surface air temperature (T_a; Figure 8a) varied with time, ranging from –37.6°C
520 (December 29) to –16.1°C (December 22), a range of values that is similar to that observed during
521 winter in the Beaufort Sea (Persson et al., 2002), while larger wintertime variability has been
522 observed over sea ice closer to the North Atlantic (Cohen et al., 2017). The spatial differences
523 (Figure 8a) were smaller than the temporal range, being no more than 5°C, and generally
524 transient. Figure 8b shows the large temporal variation of the downwelling longwave radiation
525 (LW_d), which is the primary forcing of T_a (Figure 8a) during winter, similar to that shown in the
526 western Arctic winter by Persson et al. (2002). The spatial variability was usually much lower than
527 the temporal variability (up to 80 W m^{-2}), but could briefly approach similar values during transition
528 periods. In the dark of winter, the net atmospheric energy flux to the surface is given by $F_{atm} =$
529 $LW_d – LW_u – Hs – H_l$, where LW_u is the upwelling longwave radiation, and H_s (H_l) is the turbulent
530 sensible (latent) heat flux. During the winter period, the spatial variability (range across sites) of
531 the mean LW_d, T_a, and F_{atm} were 1.8 W m^{-2}, 0.3°C, and 2.4 W m^{-2}, respectively (Table 2). The
532 variability for LW_d was less than the accuracy of the pyrgeometers used (Cox et al., 2023a) and,
533 therefore, does not indicate a measurable spatial difference in the mean LW_d. That the
534 atmospheric forcing supplied by LW_d was uniform on average across the DN is not surprising due
535 to the spatial extensiveness and predominance of stratiform clouds, as observed during SHEBA
536 (Stramler et al., 2011; Persson et al., 2017; see also Section 2e). The spatial variability of the
537 other two variables was slightly larger than their expected accuracies; while the differences were
538 still small, these may reflect spatial differences in the means caused by sensitivity of T_a and F_{atm}
539 to differences in the snow depth and/or ice thickness between the sites. This sensitivity is briefly
540 discussed in Section 3d.

541

542 **Figure 8. Time series of 10-minute means for meteorological measurements from late**
543 **December to late January.**

544

545 **Table 2. Mean values of downwelling longwave radiation (LW_d), near-surface air**
546 **temperature (T_a), and net surface energy flux (F_{atm}) measured at the 4 atmospheric sites**
547 **in the Distributed Network December 20, 2019–January 19, 2020.**

548
549 During the selected winter period, no strong storms passed over the DN and winds remained less
550 than 10 m s^{-1} at the observed heights. However, there were several time periods of large changes
551 in wind direction, with two of them associated with high pressure (December 20–22; January 9),
552 one during the extended period of lower pressure (December 31–January 1) and another long

553   one with the passage of a low-pressure center (January 16–19). Significant spatial variability in
554   wind direction occurred during some of these transition times, though the wind speed was often
555   weak. The atmospheric divergence calculated from the wind measurements at the L sites is one
556   measure of spatial variability in low-level winds (Figure 8f), and during this relatively quiet period
557   divergence mostly remained less than 10^{-4} s^{-1}. One longer period of atmospheric convergence
558   occurred for 48 h during January 1–2 when the easterly wind speed was modest (7–10 m s^{-1}) and
559   varied across the DN, with the wind at the southwestern side of the DN (L1) being the weakest.
560   The wind direction also varied slightly across the DN, producing this extended period of low-level
561   convergence. The DN was at this time affected by the outer fringes of a strong low-pressure
562   center (968 hPa) located in the Kara Sea far to the south (see NCEP reanalysis at NOAA; Kalnay
563   et al.,1996), though with no obvious frontal passage within the DN effecting a shift in wind
564   direction.
565
566   Figure 8 suggests that there were timing differences in the large temporal changes in T_a and LW_d
567   between the L sites, producing short periods of significant spatial variability. To illustrate the ability
568   of the atmospheric measurements within the DN to capture the spatial variability of lower
569   atmospheric processes, in this case the effects of clouds, Figure 9 shows a detailed time series
570   of LW_d, T_a, and F_{atm} at the three L sites and the Central Observatory over a 12 h time period. This
571   time interval exhibited spatial variability of 50–80 W m^{-2} in LW_d, up to 5°C in T_a, and up to 50 W
572   m^{-2} in F_{atm}, with significant temporal variability in this spatial variability. This variability was caused
573   by the transient passage of areas of variable cloud cover over horizontal scales less than the
574   extent of the DN (see also Kay et al., 2016) that are discussed briefly in Section 4a.
575
576
577   **Figure 9. Time series of atmospheric variables between 17:00 December 26 and 06:00**
578   **December 27 in 2019.**
579
580   *c. Wintertime ice dynamics and feedback with atmosphere and ocean*
581   Buoys measuring geographic position at 47 sites were active during this 30-day winter period,
582   enabling characterization of motion and deformation at a range of scales. The ensemble mean
583   drift speed followed the wind speed in time (Figure 10a). While the correlation between the wind
584   speed and ice drift time series is high (Pearsons's correlation coefficient equal to 0.9), the ice was
585   not in free drift and experienced forces other than the local wind drag, including internal ice
586   stresses and ocean drag. There were clearly quiescent intervals in the DN drift variance (Figure

21

587   10b), indicating times when the whole array was moving as one (notably December 25–29 and
588   January 3–5). As most of the buoys were separated by small to moderate distances, the ensemble
589   standard deviation responds more strongly to deformation at scales similar to the distance across
590   the L site triangle, and most events with high ensemble standard deviation coincided with high
591   shear or divergence in the L site array. Turning angles (difference between the ice drift direction
592   and wind direction) were generally about 27 degrees to the right during these 30 days (Figure
593   10d) with intermittently strong variability. Though the mean ice drift to wind speed ratio (drift speed
594   ratio) was 0.02, it was not constant throughout the time series (Figure 11e), with time periods
595   when the ice moved more in response to the wind (e.g., December 31–January 3; January 16–
596   18; high drift speed ratio) and others when the ice was converging and the apparent wind factor
597   reduced (January 6–8; January 18–19; low drift speed ratio). The latter indicates times when ice
598   internal stresses were dissipating wind momentum transferred to the ice. During periods of large
599   ice drift speed ratios, momentum transfer to the ice and the ocean was enhanced. Of the 11 large-
600   scale shearing events (Figure 10g), only four (December 31, and January 8, 18 and 19) coincided
601   with large local shifts in wind direction. These events are associated with small drift speed ratios
602   (a higher fraction of wind momentum being transferred to internal ice stress) and large turning
603   angles. Under convergent conditions, the ice pressure that leads to local ridging may have been
604   produced by wind shifts at a distance well beyond the L sites, rather than locally. Both the drift
605   ratios and the turning angles exhibited spatial variability between the sites that was generally
606   much smaller than the temporal variability, though a few brief periods had more pronounced
607   spatial variability (e.g., the drift speed ratio at L1 is much larger for part of January 1).
608
609   As sea ice deformation and shear occur heterogeneously at different scales (Marsan et al., 2004;
610   Hutchings et al., 2012; Itkin et al., 2017), we analyze the hourly divergence and shear (Figure 11f
611   and g) at two scales: from the ring of buoys on the DN perimeter, representing the larger scale of
612   the full DN, to a smaller scale from the triangle linking the three L sites. The difference between
613   deformation of the triangle formed by the L sites and the perimeter of the DN (Figure 10f)
614   demonstrates how local deformation can vary from the larger-scale aggregate motion. Figure 11f
615   and g show that the local shearing event on January 13 occurred within the L site triangle, which
616   opened and sheared, and is associated with ridging (convergence and decrease in area) across
617   the full DN, while only moderate shear was observed at the large scale. Conversely, on January
618   6, strong convergence and shear occurred on the large scale, with very weak convergence and
619   little shear occurring on the small scale.
620

621   Sea ice divergence and shear occur along quasi-linear active leads and ridges which arrange into
622   shear zones (Kwok, 2001; Spreen et al., 2017). These shear zones can extend hundreds of
623   kilometers, and during December 20–January 19 we observed 11 distinct large-scale shearing
624   events that extended across the DN and produced a shear signature on the large scale (Figure
625   10g). These events are apparent in the drift trajectories and are marked by large-scale shear
626   above 1 x 10^6 s^{-1}. Shear events happen across a continuum and thus the number of events
627   depends on the threshold used. Most of these events occurred between December 30–January
628   2. Interestingly, few large-scale shearing events coincided with shear events calculated from the
629   L sites, indicating that most large-scale events did not split the L site triangle, as evidenced by
630   the stable distances between sites (see also Section 3b). Furthermore, the times of many of these
631   large-scale shearing events did not coincide with the shifts in local wind direction and speed seen
632   in Figure 11a and c, suggesting the remote wind forcing discussed earlier. Local deformation and
633   spatial variability in deformation can be related to the physical response of the ice to the local
634   wind forcing and sub-diurnal changes in ocean currents. Those large-scale shearing events that
635   split the DN into two pieces can often be identified both from the differential motion of buoys
636   (Watkins et al., 2023b) and/or an increase in variance of the buoy speeds during the events
637   (Figure 10b). Both large drift speeds and large variances are associated with six large-scale ice
638   dynamics events between December 30–January 18. The first five of these coincided with shear
639   that extended across the full DN. During January 16–17, ice drift variance increased without
640   shearing, which only first occurred at the end of this period near the beginning of January 18 and
641   into January 19. This time period is associated with a transition from the predominantly high
642   atmospheric pressure conditions driving ice convergence during most of the 30 days to lower
643   pressure with more variable divergence across the DN (see Figures 8e and 12f).

644

645   **Figure 10. Time series of ice drift and deformation from late December to late January.**

646

647   We see a semi-diurnal fluctuation in mean ice drift with an amplitude of approximately 0.01 m s^{-1}
648   (Figure 10), indicative of ocean forcing from tides and/or inertial motion in the upper ocean (e.g.,
649   Hinkins, 1967; McPhee, 1978; Gimbert et al., 2012). At individual L sites this semi-diurnal variation
650   was more prominent during periods of strong wind (Figure 10a). These fluctuations illustrate the
651   coupling between the ice and the ocean (see also Section 3e), while the atmosphere shows no
652   semi-diurnal cycles. These cycles are also not apparent in the ice divergence and shear,
653   indicating that, during the majority of the period, the response was coherent at the scale of the
654   DN, as expected for inertial motions, and had a loss of coherence on smaller spatial scales. The

23

655   mechanical dissipation in the ice was episodic, and during convergence we do not see the semi-
656   diurnal upper ocean currents modulating the deformation. The ocean response is discussed
657   further in Section 3e.

658

659   *d. Wintertime ice thermodynamics and feedback with the atmosphere and ocean*
660   Distributed measurements of snow and ice were made throughout the DN to sample variability in
661   ice and snow thermodynamics and mass balance. The snow depth between different sites and
662   within individual sites was variable. During the winter period, the observations from 13 IMB buoys
663   (SIMBA, see Table 1) deployed over the DN, the Central Observatory, and the L and M sites,
664   were available for the analysis of sea ice thermodynamic mass balance processes and their
665   feedback to the atmospheric forcing (Lei et al., 2022a). The 30-day average snow depth ranged
666   from 0.14–0.33 m (Figure 11a), with both the largest and the smallest snow depths observed at
667   the Central Observatory (approximately 2 km from the ship) and the LM site, respectively. These
668   results indicate that, at the DN scale, there was no significant difference in snow depth on level
669   ice among the sites. However, at the scale of an individual floe, the ice surface topography around
670   the location of individual buoys and snow redistribution processes affected the spatial distribution
671   of snow depth. This effect has been confirmed in the transect measurements of snow depth at
672   the Central Observatory (Itkin et al., 2023), where the regions near ice ridges preferentially
673   accumulated snow. On average, there was no significant accumulation of snow based on the 13
674   IMBs during the 30 days. The variability in snow depth at various sites indicates snow
675   redistribution and local effects.

676

677   At the beginning of the winter period, the ice thickness range was 0.80–1.80 m across the sites
678   (Figure 11b). The ice bottom at all sites had entered the growth stage, with a 30-day mean ice
679   growth rate ranging from 0.003–0.008 m d^{-1}. Therefore, the sea ice thickened by 0.10–0.24 m
680   over 30 days. The differences in ice growth rates were regulated mainly by sea ice thickness
681   (Stefan, 1891; Maykut and Untersteiner, 1971; Maykut, 1978). The ice thickness can explain 44%
682   of the ice growth rate at these 13 sites ($P < 0.05$); that is, thin ice has a higher growth rate due to
683   the higher conductive heat flux through the ice layer.

684

685   The ice temperature was regulated mainly by the net atmospheric energy flux (F_{atm} in Section 3b,
686   Figure 8), which includes both radiative and turbulent atmospheric fluxes, and the conductive
687   fluxes modulated by snow and sea ice thickness (Figure 11). From December 20 to January 2,
688   the ice layer was generally in a gradually cooling state (Figure 11c). The bulk-average ice

689   temperature through the ice layer decreased from –7.0°C to –8.7°C during this period, which can

690   be attributed mainly to the overall negative values of F_{atm} and contributed to the weakly negative

691   trend in T_a (Figure 8a). Subsequently, the bulk-average ice temperature remained relatively

692   stable, and even increased slightly by the end of these 30 days (Figure 11c), as the air

693   temperature was relatively steady and the thickness of sea ice gradually increased (Figure 11b).

694   The conductive heat flux at the top ice layer (0–0.10 m) is often balanced by the heat released

695   from the snow-covered ice layer to the near-surface atmosphere (F_{atm}), assuming that the

696   conductive heat flux at the snow-sea ice interface is continuous. We have not directly calculated

697   the conductive heat flux through the snow layer, as the texture of the snow layer at various

698   measurement sites showed significant differences, which increases the uncertainty of the

699   calculation. Instead, we use the conductive heat flux at the top of the ice layer to illustrate the

700   contribution of the snow-covered ice layer to the surface heat balance. This heat flux reveals

701   strong spatial differences, with the 30-day averages in the range of 32–118 W m^{-2}. The lowest

702   heat flux was obtained from the Central Observatory because of the largest snow depth; the

703   highest heat flux was at L3 because of the relatively small snow depth (0.17 m) and ice thickness

704   (1.09 m). The observed heat flux does not show a clear temporal trend, with the multiple-site

705   average in the range of 41–75 W m^{-2}. The changes in near-surface air temperature can explain

706   55% of the temporal variability of this heat flux (P < 0.001).

707

708   *e. Vertical forcing in the upper ocean and mesoscale horizontal variability*

709   During the 30-day case study, the drifting DN spanned a spatial gradient in absolute salinity in

710   the upper-ocean mixed layer with generally higher values in the southwest and lower values in

711   the northeast of the area surveyed, as seen in the absolute salinity at the M sites (Figure 12). This

712   DN-scale gradient is embedded in the large-scale gradient in near-surface salinity and freshwater

713   content between the Eurasian and Amerasian basins (e.g., Steele et al., 1998; Rabe et al., 2011).

714   Note that the instantaneous distance across all sites was approximately 50 km, and their relative

715   distances were stable to within 1–2 km (see also Figure 7). We observed interspersed mesoscale

716   and smaller-scale features, represented by variations in absolute salinity over a few kilometers or

717   less. These features are noticeable even at depths of 75–100 m (Figure 13).

718

719   **Figure 11. Snow and sea ice mass balance data from late December to late January.**

720

721   **Figure 12. Horizontal distribution of absolute salinity at 10 m depth from late December**

722   **to late January.**

Figure 13. Absolute salinity at discrete depths across the Distributed Network from late December to late January.

The upper-ocean mixed layer, based on profiles of density (derived from pressure, conservative temperature and absolute salinity) at the L sites, exhibited variability on weekly to sub-daily time scales (Figure 14). In particular, the observations at L3 captured short-term variability due to rapid sampling, with profiles every 3 hours. Overall, a thickening mixed layer was observed, though the trend was much smaller than the short-term variability. The changes at the different sites were 0.17–0.30 m day^{-1}, equivalent to a thickening of 4–9 m from December 20 to January 19 (Figure 14). This compares to a thickening between October to March of around 30 m (Rabe et al., 2022, their Figure 9) and seasonal ranges in the eastern Arctic generally 50 m or higher, though based on observations largely near the continental slopes (Peralta Ferriz and Woodgate, 2015). Note that the short-term variability observed at L3 shows stronger peaks as the mesoscale and smaller-scale processes were better sampled, unlike L1 and L2 where the signal from these processes is aliased. The overall thickening of the mixed layer was likely forced primarily by the continuous surface cooling (negative net atmospheric energy flux; Section 3b, Table 2, Figure 10d) and ice growth (Section 3c, Figure 11) adding brine and, hence, leading to haline convection in the upper water column (see, e.g., Foster, 1969; Smith and Morison, 1998; Backhaus and Kaempf, 1999). The depth was also limited by the central Arctic end-of-melting-season stratification, different to less stratified regions (e.g., as much as 100 m north of Svalbard in winter; Koenig et al., 2016; Meyer et al, 2017). Intermittently, however, the depth of the mixed layer was strongly governed by the interplay of surface-forced momentum flux and changing stratification, as outlined below.

Figure 14. Time series of mixed layer depth at sites L1–3 from late December to early January.

We hereafter focus on the ocean velocity magnitude response and upper ocean stratification at sites L1 and L3 from measurements by the Autonomous Ocean Flux Buoys; the eddy correlation turbulence measurements and resulting heat, salt and momentum fluxes are analyzed elsewhere (B Shaw and T Stanton, personal communication). The two sites were located approximately 35 km apart and illustrate important similarities and differences seen at this scale, in particular the ocean response to atmosphere-ice forcing. Differences between the wind speed and ice speed (Figure 16a and d) reflect a combination of ice mobility, deformation and lead formation, discussed

26

in Section 3c, and potentially differing atmosphere-ice and ice-ocean drag coefficients through the time series (see also Cole et al., 2017). The time series of current speed profiles (Figures 16b and e) show the formation of shallow wind-forced turbulent layers (see also Shaw et al., 2008; Cole et al., 2014) extending down from the ice-ocean interface during each of the stronger wind events. This effect is most clearly seen in wind events during December 29 to January 4 and January 9–18. The strong, transient forcing of these winds resulted in significant levels of inertial ringing in the water column (and ice), revealed as near-diurnal vertical stripes in current magnitude superimposed on the lower frequency mean response. The penetration depth of these ice-ocean shear-forced Ekman layers was strongly dependent on the water column stratification. Even small vertical density gradients in the water column rapidly diminished local turbulent mixing as turbulent kinetic energy was expended while entraining less buoyant fluid from below.

Surprisingly high levels of stratification were observed shallower than the strong winter halocline (pycnocline) depth at about 35 m during this period. The high levels of mesoscale density structure in the mixed layer (Figure 16c and f) profoundly affected upper ocean mixing and momentum transfer from the ice into the ocean (B Shaw and T Stanton, personal communication). The strong salt-stratified density gradients at the top of the halocline, or bottom of the mixed layer, were also observed as transitions in vertical current structure reflecting high shear levels at this interface. The sloped vertical stripes in Figure 15b and e within the strongly stratified pycnocline indicate inertial motions propagating into the deeper ocean. Examples of the reduction of turbulent mixing depth by these weak vertical density gradients can be seen by comparing the full mixed layer depth (35 m; Figure 14) Ekman layer at L1 (Figure 15b and c) formed during the strong January 13 winds with the much shallower penetration of the enhanced current layer at L3 (Figure 15e and f). There, near-surface vertical density gradients as shallow as 15 m depth (Figure 15f) shoaled between January 13 and 15. As this wind event continued January 14–17, L3 drifted over part of a strong halocline eddy feature seen clearly in enhanced currents at the top of the domed pycnocline that shoaled as shallow as 25 m depth. Currents arising from this eddy were largely isolated from the mixed layer above by the strong halocline density gradient, and thus did not affect the ice speed.

Figure 15. Wind, ice and ocean speed, and ocean density, from late December to late January .

Figure 16. Wind speed, upper ocean currents and ice inertial band motion, late December to late January.

Significant differences in vertical and horizontal density structure between L1 and L3 (Figure 15) within the mixed layer emphasize the small scale of the upper-ocean mesoscale features. Although the feature centered on December 24 was clearly observed in the profiling Woods Hole Ice-tethered Profiler at both L sites and the 10-minute records of conservative temperature and absolute salinity at M4 (Figure 13a), the following feature at L1, centered on December 30, was encountered 1–2 days later at L3, M1 and M6 as more diffuse features (Figures 13b and 15f). The mesoscale features are associated with strong changes in density profile structure, varying over distances comparable to the 1st-mode baroclinic Rossby radius and have been identified at different times during the operation of the DN (e.g., Hoppmann et al., 2022a). They can reach downward well into the upper halocline and even touch the lower halocline, here around 60–100 m (see, e.g., Rabe et al., 2022, their Figure 10). Smaller-scale differences between sites as well as synoptic variability are visible at all depths, evident in particular at 75 m throughout the time period (Figure 13).

Time series of surface winds, upper ocean current magnitude, inertial-band energy, and ice inertial band motion for L1, L3 and the Central Observatory (Figure 16) show accelerations of the upper mixed layer currents concurrent with the onset of high levels of inertial motion in the ocean-ice coupled layer, in response to a strong transient wind event starting on December 29. This inertial ringing of the ice coupled into the ocean mixed layer is seen widely in the Arctic (e.g., Brenner et al., 2023), but usually in conditions of lower ice coverage and high ice mobility in late summer and fall. The ocean inertial currents at each of the three sites (Figure 17c) show some spatial variability compared with the more coherent spatial response of the ice (Figure 16d), largely because of differences in the mixing layer depth through which the inertial momentum is distributed at each site. The actively mixing layer did not always extend to the bottom of the mixed layer (e.g., Schulz et al., 2022, their Figure 4) that had been homogenized previously. Overall, this strong inertial response in mid-winter is indicative of the relatively weak and mobile ice pack encountered during the MOSAiC drift. Differences in the magnitude of the ice inertial oscillations between the three DN observation stations (Figure 16d) are likely indicative of the local mobility of the ice pack.

f. DN observations during the temporal gap in Central Observatory measurements

825   The two main benefits of the autonomous DN instrumentation are the spatially distributed nature
826   of the observations and their ability to fill temporal gaps in the manual measurements at the
827   Central Observatory. Even when the latter had to be suspended from May 16 to June 18, 2020,
828   due to RV *Polarstern* leaving for a personnel exchange, the DN continued to obtain data from
829   83.4°N to about 82.4°N (dashed-line box in Figure 4). We can clearly see the near-freezing T_a
830   after melt onset (Light et al., 2022) on May 25 (Figure 17d), indicative of a melting ice and snow
831   surface (Figure 17) from excess surface energy flux (Persson et al., 2012) and eventually leading
832   to increasing radiation into the upper ocean after about June 4 (Figure 18c).

833

834   **Figure 17. Late-spring snow and sea ice mass balance and conductive heat flux at the ice**
835   **surface.**

836

837   As shown in Figure 17a–c the cold interior of the sea ice warmed gradually (see also Lei et al.,
838   2022a; Salganik et al., 2023) from May to June 2020, through warming from both above and
839   below. The increased sea ice temperature suggests that the volume fraction of brine was
840   gradually increasing and gradually enhanced its permeability (Golden et al., 1998). Intermittent
841   surface cooling (e.g., June 2–12), however, led to superimposed ice in June, that can be identified
842   in data from IMB (SIMBA, Table 1) heat cycles at L2 and L3 and that is not visible in the
843   temperature data alone (Lei et al., 2022a). The snow cover had completely melted away at L1
844   and L2 by June 8 and 16, 2020, respectively (Figure 17a and b). At the L3 IMB (SIMBA, Table 1)
845   the snow cover thinned to 0.10 m by June 18 and melted completely by June 24. Similarly, snow
846   melt continued until June 29 when all the snow had melted and surface ice melt began, as
847   observed by another L2 IMB (SIMB3, Table 1; Perovich et al., 2023). These observations indicate
848   the spatial heterogeneity of surface snow melting, mainly due to initial snow depth and surface
849   topography, that was documented thoroughly by the IMB observations and the manual surveys
850   during the early setup of the DN.

851

852   The conductive heat flux at the surface 0.1 m layer of ice cover was affected mainly by near-
853   surface air temperature, with the daily near-surface air temperature explaining 25% (P < 0.01) of
854   the conductive heat flux (Figure 17). After the relatively warm period May 25–30, 2020, the snow
855   began to melt faster and exhibited greater spatial differences, which gradually increased the
856   spatial differences in conductive heat flux at the sea ice surface. Overall, the conductive heat flux
857   on the sea ice surface remained negative (downward), except for the temporary positive heat
858   conduction (upward) caused by relatively low air temperatures on May 17. The dominant heat flux

859   indicates that during this period May 16–June 18, the sea ice layer mainly acquired heat from the
860   atmosphere, which is the main source of energy that warmed and melted the ice. Especially during
861   the warmer periods, May 26–30 and after June 16, the downward conductive heat flux was more
862   pronounced.

863

864   There are obvious spatial differences at times when the bottom of the sea ice began to melt,
865   ranging between May 17 and June 20, 2020, across 15 IMB (SIMBA, Table 1) in the DN, which
866   mainly depends on the thicknesses of sea ice and the overlying snow cover (Lei et al., 2023a).
867   While the seawater temperature forcing under all DN sites was similar, the relatively thin sea ice
868   at some locations made the ice layer more sensitive to seasonal surface warming, leading to
869   earlier melt onset at those locations. Basal ice melt at various IMB (SIMBA, Table 1) at L1, L2
870   and L3 commenced on June 15, June 20 and June 12, respectively (Figure 17), concurrent with
871   an ocean-to-ice heat flux of around 10 W m^{-2}, about 5 times the December-to-April mean (Lei et
872   al., 2022a). In addition, a seasonal IMB (SIMB3, Table 1) deployed at L2 observed the bottom ice
873   melt at this site beginning June 11, 2020 (Perovich et al., 2023). At the Central Observatory the
874   earliest basal melt was observed on May 27 (Salganik et al., 2023), and melt ponds started to
875   form at the same time (Webster et al., 2022). Freshening just under the ice with the formation of
876   under-ice meltwater layers was observed by the IMB (SIMBA, Table 1) temperature profiles, at
877   L1 and L2 on July 31 and June 26, respectively, but at L3 already on June 16 (Lei et al., 2022a).
878   Also, in the Central Observatory the earliest record of under-ice meltwater layers was on June 16
879   (Smith et al., 2022; Salganik et al., 2023). The difference in timing of under-ice meltwater layers
880   may be related to the thinner ice present at L3 and part of the Central Observatory. This thinner
881   ice could have allowed earlier meltwater drainage, lower draft or higher occurrence of ridges at
882   these sites, each of which could have controlled the accumulation of meltwater below the ice
883   (Salganik et al., 2023).

884

885   In the ocean, there was a shoaling of the upper-ocean mixed layer toward the end of the time
886   period (see Rabe et al., 2022, their Figure 10, for Woods Hole Ice-tethered Profiler data from L1
887   without data gaps; see also Schulz et al., n.d.). The seawater temperatures were close to freezing,
888   almost as low as the lowest observed in the DN further north during April. At the same time,
889   absolute salinity was generally closest to that of Fram Strait inflow of Atlantic Water (Figure 18).
890   One Salinity Ice Tether (SIT, Table 1) recorded almost equal conservative temperature and
891   absolute salinity in the top 100 m at M3 until early June with a small increase thereafter (Figure
892   19), suggesting that the base of the mixed layer stayed deeper than that until June 15 at this

893 location about 20 km from L2. However, a few warm spells occurred at M3 around 100 m depth
894 and from about June 10 between about 50 m and 100 m depth (not shown). The deep signal is
895 hinted at in the L2 Woods Hole Ice-tethered Profiler values deeper in the water column (Figure
896 18a) before the profiler was no longer able to reach the upper water column.

897

898 The automated observations in the DN at L2 were particularly important for the description of the
899 phytoplankton bloom under the MOSAiC floe, which developed during the absence of RV
900 *Polarstern* following the increase in photosynthetically active radiation in the water column under
901 the ice (Figure 18c). This timing coincided not only with a general increase in incoming solar
902 radiation (not shown) but also with the gradual melting of snow at L2 during June which, although
903 differing across the floe, shows the overall disappearance of the snow cover. While the under-ice
904 bloom was fully developed by the time that discrete sampling began again in the Central
905 Observatory on June 16 (not shown), the Woods Hole Ice-tethered Profiler chlorophyll *a*
906 fluorescence data indicate that the ecologically important onset of biomass increases occurred in
907 the upper 30 m at the beginning of June, with subsequent deepening of biomass down to 70 m
908 (Figure 18d). Despite the large-scale gradient in stratification shallower than 100 m from the
909 Amundsen to the Nansen basins (Rabe et al., 2022, their Figure 10) the change in
910 photosynthetically active radiation coincided with a small increase in upper ocean stratification
911 starting on June 4 that covered approximately the top 100 m (Figures 18a and 19). Turbulent
912 mixing, however, was still focused on the top 40–70 m most of the time in early May and late
913 June, making likely that similar conditions prevailed during the time we focus on here (Schulz et
914 al., 2022) and, thus, allowing phytoplankton to stay in that depth range (Figure 18d). Furthermore,
915 the Woods Hole Ice-tethered Profiler chlorophyll *a* fluorescence data potentially indicates an
916 export event of biomass from the sea ice in mid-May, which would fit well with the observed melt
917 onset dates in the DN, as described above. Further analysis is needed to confirm this export
918 event, such as that done by Laney et al. (2014) for prior observations.

919

920 **Figure 18. Ocean properties late May to early June, observed by Woods Hole Ice-tethered**
921 **Profiler #94 at site L2.**

922

923 **Figure 19. Absolute salinity at discrete depths at site M3 from late May to early June.**

924

925 4. DISCUSSION

a. Discussion of DN results and synergies with remote sensing and other observations

Our observational results outlined in Section 3 describe the overall drift of the buoys and illustrate the ability of the MOSAiC DN to resolve spatially variant coupled-system processes, from small scale to mesoscale, and fill temporal gaps during the drift by autonomously observing even in the absence of manual observations. Here, we address these results considering existing literature and show synergies with remote sensing and other observations.

From the different ice observations and electromagnetic induction surveys we know that the region of the DN was initially covered primarily by first-year ice, with approximately 10% being multi-year ice that survived from the previous growth year (Krumpen et al., 2021, their Figure 5a). The observations stem from the marginal ice zone, that was found far north in the central Arctic, and follow a long-term shift in ice types across the Arctic. Warming and reduced sea ice cover have been reported during 1990–2018 in the Bering and Chukchi seas (Danielson et al., 2020), and the eastern Arctic is also approaching a state of seasonal ice cover (Haine and Martin, 2017; Perovich et al., 2020). Therefore, the observed prevailing pattern of first-year ice during the DN drift appears to be a "normal feature" on the pan-Arctic scale.

During our 30 mid-winter days, atmospheric near-surface variability was strongest at time scales of less than one day, and temporal variability was much larger than spatial variability most of the time; the latter was also true for wind-driven ice motion. Although the monthly-mean (winter) atmospheric variables observed immediately above the surface were small, relative to the temporal variability, there were differences in the air temperature and the net atmospheric energy flux between sites. These differences influenced the ice temperature across the DN, also considering the conductive heat flux through the variable snow cover. The conductive heat flux through the snow varied between sites in the mean over the 30 days as well as showing temporal variability. The latter can be explained by changes in air temperature to more than 50%, in contrast to the late spring/early summer situation (Figure 11d), where we find these changes to be only about half that. This difference can be explained by the complex thermodynamic characteristics of the snow and sea ice surfaces during the melting period, such as significant temporal changes in snow moisture content (Sturm et al., 2002; Nicolaus et al., 2003). Ice growth appears to have been dominated by absolute ice and snow thickness at each buoy, with the highest heat flux coinciding with the smallest ice and snow thickness. This result indicates that as Arctic sea ice thins, heat released from the sea ice-ocean system towards the near-surface atmosphere in

32

960 winter can be expected to increase, assuming the snow depth does not increase. It also means
961 that ice growth rates would increase accordingly (Stefan, 1891; Maykut and Untersteiner, 1971).
962 Our preliminary analysis does not suggest a strong influence of storms on sea ice formation, such
963 as found by Graham et al. (2019) for N-ICE2015 (see Section 2e), though the observed sudden
964 changes in wind direction (Figure 8) likely led to events in the ice dynamics (e.g., Figure 10g) and
965 some lead formation (Section 3c) that may have released heat and moisture from the ocean
966 directly to the atmosphere.

967

968 The effect of atmosphere-ice-ocean momentum transfer was subject to internal dynamical
969 processes in both the sea ice and the ocean. The DN position observations, which resolve ice
970 motion on a large range of time scales, show that the sea ice motion is strongly correlated with
971 the near-surface wind, as is the upper portion of the ocean mixed layer, where significant spatial
972 and temporal variability was observed. However, deformation in the sea ice is only sometimes
973 linked with wind transitions, whereas at times the ice-internal stresses dampened the momentum
974 transfer from the atmosphere. Consolidated ice cover generally damps momentum transfer
975 between the atmosphere and the ocean heterogeneously (Cole et al., 2017), although that
976 dampening is generally more pronounced in the marginal ice zone (Manucharyan and Thompson,
977 2017) than in the even more consolidated ice cover we observed. Ocean mixed layer horizontal
978 density gradients and deeper ocean eddies also impacted the mixed layer currents. Hence, the
979 dynamics of all three media played a role in the dynamics of the ice and the ocean surveyed,
980 while neither the ice nor the ocean seems to have impacted the observed winds significantly
981 during our 3-day mid-winter period.

982

983 The ocean observations in the DN show a complex interplay between spatial and temporal
984 variability. Even though the mesoscale and sub-mesoscales were not resolved instantaneously,
985 we could observe quasi-synoptic features, such as eddies, often at more than one site over time
986 periods of one to several days; some of these features were in direct contact with the surface,
987 while others were isolated by local stratification close to the surface. Studying those processes in
988 detail is beyond the scope of this work, as that generally involves direct and indirect feedbacks
989 between ocean, ice and atmosphere. The reader is referred to ocean-focused studies, such as
990 Hoppmann et al. (2022), Kawaguchi et al. (2022), Kuznetsov et al. (2023), and Fang et al. (n.d.).

991

992 Apart from the small influence of snow and ice conditions on the mean atmospheric variables
993 near the surface, the DN captured several transient atmospheric features with substantially

994 shorter time scales than the 30 mid-winter days, such as clouds, fronts and pressure gradients of
995 the passing synoptic systems. This atmospheric variability forced the observed divergence of sea
996 ice and brief departures from the overall thermodynamic homogeneity. Here, we illustrate the
997 combined use of the DN observations and a scanning Ka-band radar (provided by the Department
998 of Energy Atmospheric Measurements Program), mounted on top of the bridge of RV *Polarstern*.
999 The radar observations (Figure S4) reveal details of how a shallow, spatially limited cloud field
1000 produced the variability in LW_d (see also Figure 9) across the DN. Near 23:00 UTC December 26,
1001 the skies were mostly clear across the domain, with low values of LW_d. Shortly before 00:00 UTC
1002 December 27, a region of clouds crossed the domain from the southwest (L1) and sequentially
1003 raised the LW_d by 40–50 W m^{-2} across the different sites, with related increases in F_{atm} and T_a
1004 and subsequent decreases in LW_d, T_a, and F_{atm}. The changes in F_{atm} represent the changes in
1005 the atmosphere's net thermodynamic forcing of the sea ice surface. Similarly, the ship-mounted
1006 C-band radar onboard RV *Polarstern*, using a similar digitizing system approach as the N-
1007 ICE2015 campaign (Oikkonen et al., 2017), captured the very episodic (hours to days) and
1008 localized sea ice deformation events. These radar observations agree with our findings on sea
1009 ice deformation in Section 3a and c and highlight the benefit of covering different scales with the
1010 DN and this radar.

1011

1012 Due to the invisibility from space and the reduced accessibility for in situ sampling, observations
1013 of under-ice phytoplankton blooms in the Arctic are sparse (Ardyna et al., 2020), hence the
1014 MOSAiC DN observations from late spring/early summer cover a gap in knowledge. The
1015 previously available data from the 1950s (Apollonio, 1959; English, 1961) indicate that blooms
1016 under multi-year ice started later (i.e., at the end of June) but developed higher biomass than
1017 observed by the DN. During SHEBA (Section 2e) two phytoplankton blooms were observed
1018 around the Chukchi Plateau and the southeastern Makarov Basin from late May 1998 to early
1019 September 1998, covering a similar vertical range as the DN observations, though with an order
1020 of magnitude higher concentration of chlorophyll *a* (Sherr et al., 2003). More recent observations
1021 below central Arctic first-year ice (Boles et al., 2020) indicate similar timing and magnitude of
1022 under-ice blooms as observed in the DN.

1023

1024 Overall, the DN captured variability at the scales set out to be studied in MOSAiC, even though
1025 the upper ocean mesoscale and sub-mesoscales could not be resolved in the way planned.
1026 However, the varying ice drift during several selected time periods still allows a detailed, quasi-
1027 synoptic analysis of both the sub-mesoscale and mesoscale ocean variability. As the ocean was

34

1028 observed at a larger scale than planned, we can obtain a better impression of the conditions and
1029 dynamics on scales up to 40 km.

1030

1031 Further remote sensing observations during MOSAiC captured different temporal and spatial
1032 scales than the DN, including information on the deformation and morphological changes in the
1033 ice surface by satellite, airborne, and surface-based remote sensing; for example, SAR-based
1034 ice-motion tracking (Nicolaus et al., 2022; Guo et al., 2023), melt pond distribution and albedo
1035 (Neckel et al., 2023, Sperzel et al., 2023), sea ice topography (Hutter et al., 2023; see also Figure
1036 6), and sea ice thickness (von Albedyll et al., 2022; see map of airborne campaigns parallel to
1037 MOSAiC in Figure S5). Analyzing these data sets in conjunction with DN observations has been
1038 the subject of studies targeting specific variables and aspects of the MOSAiC coupled system.

1039

1040 *b. DN model applications and synergies*
1041 The MOSAiC observations, in particular those by the DN, provide a unique opportunity to facilitate
1042 model and forecast improvements. The WMO Year of Polar Prediction (YOPP) initiative, aimed
1043 to advance polar prediction capabilities (Jung et al., 2016), coordinated its international efforts
1044 between 2013 and 2022 with MOSAiC. In particular, several operational Numerical Weather
1045 Prediction centers saved additional model parameters at high temporal and spatial resolutions
1046 along the MOSAiC track to enable in-depth analyses, evaluation, and forecast improvements of
1047 the coupled Arctic atmosphere-ice-ocean system (e.g., Bauer et al., 2020; Solomon et al., 2023).
1048 Promising studies exemplifying the value of MOSAiC data in general for model evaluation have
1049 already been appearing (e.g., Dethloff et al., 2022). In the following we provide only selected
1050 examples of how the information about spatial heterogeneity measured by the DN can provide
1051 added value to evaluating models and forecast systems.

1052

1053 The MOSAiC campaign was provided with real-time sea ice drift forecasts by the Sea Ice Drift
1054 Forecast Experiment (SIDFEx) for the Central Observatory and a number of DN sites to facilitate
1055 satellite image ordering and other logistical tasks (Nicolaus et al., 2022). The representation of
1056 sea ice deformation in models has been studied widely (e.g., Spreen et al., 2017; Rampal et al.,
1057 2019) and a recent study by Korosov et al. (2023) highlights the potential of assimilating satellite-
1058 derived sea ice deformation to improve sea icesea ice deformation forecasts up to 3–4 days. One
1059 could use the SIDFEx forecasts to compare the sea ice deformation forecast skill of a broad range
1060 of forecast systems with lead times up to 10 days. The systems with spatial resolutions of 5–12
1061 km (e.g., Guiavarc'h et al., 2019), though designed to represent average behavior on scales of

35

1062 about 100 km and weeks to months (Blockley et al., 2020), may be able to forecast deformation
1063 events on the scale of the outer ring of the DN, like those described in Section 3c.

1064

1065 **Figure 20. Comparison of wintertime observations and 2-day forecasts during October 15,**
1066 **2019–March 15, 2020.**

1067

1068 The DN observations have also been used to evaluate coupled processes unique to the Arctic in
1069 forecast systems, such as the representation of low-level clouds, the representation of the stable
1070 boundary layer, atmosphere-snow interaction, and ocean-sea ice-atmosphere coupling (see
1071 Solomon et al., 2023). Such evaluations are illustrated in Figure 20, where observations of
1072 wintertime skin temperature, measured with the Atmospheric Surface Flux Stations at the L sites
1073 and from the Central Observatory meteorological installation, and of the surface ice temperature,
1074 measured with several IMB (SIMB3, Table 1), are compared to forecasts from five state-of-the-
1075 art coupled forecast systems at a 2-day lead time. The observed low frequency skin temperature
1076 variability is simulated by all the forecast systems. This close correspondence with observations
1077 is not seen for the surface ice temperature (Figure 20b), where the modeled temperatures differ
1078 by ±10°C from the observations by the different IMB. The DN provides observations that cover a
1079 variety of conditions within a model grid box, thereby substantially enhancing the ability to
1080 evaluate and improve simulations of the coupled Arctic system.

1081

1082 The Next Generation Earth Modelling Systems (nextGEMS) global storm- and eddy-resolving
1083 models with European Centre for Medium-Range Weather Forecasts (ECMWF) Integrated
1084 Forecasting System and the ICOsahedral Nonhydrostatic model represent a new class of
1085 kilometer-scale climate models that are the starting point for climate adaptation "Digital Twins"
1086 (Bauer et al., 2021a; 2021b). With grid box sizes well below 10 km (e.g., 4.4 km), they resolve
1087 linear kinematic features in the sea ice cover and the scale of the DN with tens to hundreds of
1088 points (not shown). Whether these kilometer-scale models start to feature some of the Arctic sub-
1089 grid variability (with respect to more typical 100 km climate model grid boxes) or whether they still
1090 suffer from being too spatially homogeneous can also be answered with the unique DN
1091 observations.

1092

1093 Comparing observations to model simulations generally suffers from differences between the
1094 internal variability of the model and the observations (e.g., Strobach and Bel, 2017; Jain et al.,
1095 2023). One effective way of maximizing the value of field-campaign data for climate model

evaluation is to "nudge" the large-scale circulation in climate models, as demonstrated for MOSAiC data by Pithan et al. (2023). Another example is a high-resolution implementation of an ocean-only model with an irregular grid, sigma vertical coordinates and a level upper (ice) boundary, where the ocean is nudged by the seawater temperature and salinity observed in the ocean by the DN, allowing to resolve sub-mesoscale and mesoscale features (Kuznetsov et al., 2023).

5. CONCLUSIONS

The MOSAiC Distributed Network of autonomous ice-tethered "buoy" platforms operated during the drift from the eastern Eurasian Arctic to Fram Strait in late 2019 through the first half of 2020, and with a reduced setup from late summer to early autumn 2020, after relocation to the central Arctic in late summer. The network was comprised of different instrument systems clustered around individual nodes or sites to observe the coupled atmosphere-ice-ocean climate system in the central Arctic. Instrument systems had varying complexity, ranging from comprehensive flux stations to simple position-tracking drifters. All instrumentation not only recorded autonomously but relayed most of the data via satellite to land or via radio link to the central MOSAiC ship, with the remaining data obtained during maintenance visits or after recovery. Our work presented here has focused on the utility of the MOSAiC DN for observing spatial variability on model grid scales, exploiting the autonomous nature of the instruments.

The DN observations were able to capture simultaneously both vertical processes at a single ice floe and horizontally heterogeneous processes on scales of 10–100 km, as well as on smaller scales quasi-synoptically along the drift. In addition to complex autonomous instruments, the distributed deployment of position-tracking buoys has provided information about the localized and aggregate ice dynamics, allowing relationships to the wind and ocean forcing to be identified. Importantly, the DN sites compared to crewed observations at the Central Observatory are able to provide unique insights into how representative single floe comprehensive measurements are of conditions across scales of 10–100 km, and can give long-duration estimates of the spatial heterogeneity of the coupled atmosphere, ice and ocean systems. The DN successfully observed the transition to ice melt in late spring/early summer and the change between the regions affected by low-salinity polar surface waters and those affected by near-surface waters of Atlantic origin. The corresponding time period, when the Central Observatory was unattended, was a critical time to complete our observations of the full seasonal cycle of the ice within the DN, including optical measurements of biology and chemistry, all subject to changing rapidly with climate change

1130 (Bluhm et al., 2020; Mortenson et al., 2020). Hence, there is a continuous need for more
1131 telemetered, autonomous observations, such as those of the DN. Our results also emphasize the
1132 need to carefully consider the difference of ice thickness and overall ice topography (e.g., ridges)
1133 at various buoy deployment sites, which may cause significant small-scale changes in mass and
1134 energy exchanges between atmosphere, sea ice and ocean.

1135

1136 The comprehensive nature of the instruments, and the parallel operation of an icebreaker and
1137 ice-floe-scale Central Observatory with complementary measurements and manual sampling, are
1138 important aspects of the MOSAiC DN and are unprecedented in their entirety. Together they
1139 facilitate analysis of processes that would not be possible with either clusters of autonomous
1140 instrumentation separated by larger distances than the DN sites or the stand-alone use of
1141 autonomous systems. The scientific value of the DN reaches in multiple directions. The multitude
1142 of temporal and spatial scales covered by the DN make it particularly suited to upscaling and
1143 downscaling of information, including scales that are less than large-scale model grid cells.
1144 Collectively, these observations support improved model parameterizations of ocean, sea ice,
1145 and atmosphere processes along with their key coupling interactions, as well as unique new
1146 possibilities for model validation. Lastly, this successful implementation demonstrates the
1147 feasibility of such networks and provides key guidance for future autonomous observing network
1148 installations, which ought to become more common in a warming world where everyone, including
1149 scientists, have to reduce their emissions.

Author Contribution

Contributed to conception and design

BR, JH, JR, MDS, MH, MN, TS, TK, OP, WS

Contributed to acquisition of data

AJ, BR, DMW, JH, JO, JR, JT, KRC, MDS, MH, MN, MT, TK, TS, TR, OP, RL, RK, STC, WS

Contributed to analysis and interpretation of data

AJ, AS, BR, DMW, EB, HG, JH, JR, MAG, MDS, MH, MN, MT, OP, RL, TK, TS, VL

Drafted and/or revised the article

All authors

Approved the submitted version for publication

All authors

Competing interest

All authors declare that they have no competing interests.

Data accessibility statement

All data have been archived in the MOSAiC Central Storage (MCS) and in the data repositories PANGAEA and the Arctic Data Center. Most of the unprocessed, near-real-time data is available at seaiceportal.de for preview only. References to published data sets are cited in the text.

References

Alfred-Wegener-Institut Helmholtz-Zentrum für Polar- und Meeresforschung. 2017. Polar research and supply vessel POLARSTERN operated by the Alfred-Wegener-Institute. *Journal of Large-Scale Research Facilities* **3**: A119. DOI: http://dx.doi.org/10.17815/jlsrf-3-163.

Andreas, EL, Horst, TW, Grachev, AA, Persson, POG, Fairall, CW, Guest, PS, Jordan, RE. 2010a. Parametrizing turbulent exchange over summer sea ice and the marginal ice zone. *Quarterly Journal of the Royal Meteorological Society* **136**(649): 927–943. DOI: http://dx.doi.org/10.1002/qj.618.

Andreas, EL, Persson, POG, Grachev, AA, Jordan, RE, Horst, TW, Guest, PS, Fairall, CW. 2010b. Parameterizing turbulent exchange over sea ice in winter. *Journal of Hydrometeorology* **11**(1): 87–104. DOI: http://dx.doi.org/10.1175/2009JHM1102.1.

Andreas, EL, Fairall, CW, Guest, PS, Persson, POG. 1999: An overview of the SHEBA atmospheric flux program. In *Fifth Conference on Polar Meteorology and Oceanography*, Dallas, TX, January 10–15,1999, American Meteorological Society, Boston, MA, pp. 550–555 (preprint).

Apollonio, S. 1959. Hydrobiological measurements on IGY drift station Bravo. National Academy of Sciences IGY Bulletins 27. *Eos, Transactions American Geophysical Union* **40**(3): 316–319. DOI: http://dx.doi.org/10.1029/TR040i003p00269.

Ardyna, M, Mundy, CJ, Mayot, N, Matthes, LC, Oziel, L, Horvat, C, Leu, E, Assmy, P, Hill, V, Matrai, PA, Gale, M, Melnikov, IA, Arrigo, KA. 2020. Under-ice phytoplankton blooms: shedding light on the "invisible" part of Arctic primary production. *Frontiers in Marine Science* **7**. DOI: http://dx.doi.org/10.3389/fmars.2020.608032.

Athanase, M, Sennéchael, N, Garric, G, Koenig, Z, Boles, E, Provost, C. 2019. New hydrographic measurements of the upper Arctic western Eurasian Basin in 2017 reveal fresher mixed

1248   layer and shallower warm layer than 2005–2012 climatology. *Journal of Geophysical*
1249   *Research: Oceans* **124**(2): 1091–1114. DOI: http://dx.doi.org/10.1029/2018JC014701.

1250 Bauer, P, Dueben, PD, Hoefler, T, Quintino, T, Schulthess, TC, Wedi, NP. 2021a. The digital
1251   revolution of Earth-system science. *Nature Computational Science* **1**(2): 104–113. DOI:
1252   http://dx.doi.org/10.1038/s43588-021-00023-0.

1253 Bauer, P, Stevens, B, Hazeleger, W. 2021b. A digital twin of Earth for the green transition. *Nature*
1254   *Climate Change* **11**(2): 80–83. DOI: http://dx.doi.org/10.1038/s41558-021-00986-y.

1255 Belter, HJ, Krumpen, T, von Albedyll, L, Alekseeva, TA, Birnbaum, G, Frolov, SV, Hendricks, S,
1256   Herber, A, Polyakov, I, Raphael, I, Ricker, R, Serovetnikov, SS, Webster, M, Haas, C.
1257   2021. Interannual variability in Transpolar Drift summer sea ice thickness and potential
1258   impact of Atlantification. *The Cryosphere* **15**(6): 2575–2591. DOI:
1259   http://dx.doi.org/10.5194/tc-15-2575-2021.

1260 Bliss, A, Hutchings, J, Anderson, P, Anhaus, P, Belter, H J, Berge, J, Bessonov, V, Cheng, B,
1261   Cole, S, Costa, D, Cottier, F, Cox, CJ, De La Torre, PR, Divine, DV, Emzivat, G, Fang,
1262   YC, Fons, S, Gallagher, M, Geoffrey, M, Granskog, MA, Haapala, J, Haas, C, Hoppmann,
1263   M, Høyland, KV, Hwang, B, Itkin, P, Johnsen, G, Juttila, A, Kanzow, T, Katlein, C, Kopec,
1264   T, Krishfield, R, Krumpen, T, Kuznetsov, I, Lange, B, Lei, R, Li, T, Mäkynen, M, Moore, R,
1265   Morgenstern, A, Morris, SM, Nicolaus, M, Olsen, LM, Osborn, J, Perovich, D, Persson, O,
1266   Petrovsky, T, Rabe, B, Raphael, I, Regnery, J, Ricker, R, Riemann-Campe, K, Rohde, J,
1267   Salganik, E, Shaw, B, Sheikin, I, Shupe, MD, Smolyanitsky, V, Sokolov, V, Stanton, T,
1268   Tao, R, Timofeeva, A, Toole, J, Uttal, T, Vogedes, D, Watkins, D, Zhu, J, Zolich, A, Zuo,
1269   G. 2022. Sea ice drift tracks from the Distributed Network of autonomous buoys deployed
1270   during the Multidisciplinary drifting Observatory for the Study of Arctic Climate (MOSAiC)
1271   expedition 2019–2021. *NSF Arctic Data Center*. DOI:
1272   http://dx.doi.org/10.18739/A21N7XP19.

1273 Bliss AC, Hutchings JK, Watkins DM. 2023. Sea ice drift tracks from autonomous buoys in the
1274   MOSAiC Distributed Network. *Scientific Data* **10**(1): 403. DOI:
1275   http://dx.doi.org/10.1038/s41597-023-02311-y.

1276 Bluhm BA, Janout, MA, Danielson, SL, Ellingsen, I, Gavrilo, M, Grebmeier, JM, Hopcroft, RR,
1277   Iken, KB, Ingvaldsen, RB, Jorgensen, LL, Kosobokova, KN, Kwok, R, Polyakov, IV,
1278   Renaud, PE, Carmack, EC. 2020. The pan-Arctic continental slope: sharp gradients of
1279   physical processes affect pelagic and benthic ecosystems. *Frontiers in Marine Science* **7**.
1280   DOI: http://dx.doi.org/10.3389/fmars.2020.544386.

Boles, E, Provost, C, Garçon, V, Bertosio, C, Athanase, M, Koenig, Z, Sennéchael, N. 2020. Under-ice phytoplankton blooms in the central Arctic Ocean: insights from the first biogeochemical IAOOS platform drift in 2017. *Journal of Geophysical Research: Oceans* **125**(3): e2019JC015608. DOI: http://dx.doi.org/10.1029/2019JC015608.

Bourassa, MA, Gille, ST, Bitz, C, Carlson, D, Cerovecki, I, Clayson, CA, Cronin, MF, Drennan, WM, Fairall, CW, Hoffman, RN, Magnusdottir, G, Pinker, RT, Renfrew, IA, Serreze, M, Speer, K, Talley, LD, Wick, GA. 2013. High-latitude ocean and sea ice surface fluxes: challenges for climate research. *Bulletin of the American Meteorological Society* **94**(3): 403–423. DOI: http://dx.doi.org/10.1175/BAMS-D-11-00244.1.

Brenner, S, Thomson, J, Rainville, L, Crews, L, Lee, CM. 2023. Wind-driven motions of the ocean surface mixed layer in the western Arctic. *Journal of Physical Oceanography* **53**(7): 1787–1804. DOI: http://dx.doi.org/10.1175/JPO-D-22-0112.1.

Chan, FMM, King, TG, Stout, KJ. 1996. The influence of sampling strategy on a circular feature in coordinate measurements. *Measurement* **19**(2): 73–81. DOI: http://dx.doi.org/10.1016/S0263-2241(96)00067-X.

Clement Kinney, J, Assmann, KM, Maslowski, W, Björk, G, Jakobsson, M, Jutterström, S, Lee, YJ, Osinski, R, Semiletov, I, Ulfsbo, A, Wåhlström, I, Anderson, LG. 2022. On the circulation, water mass distribution, and nutrient concentrations of the western Chukchi Sea. *Ocean Science* **18**(1): 29–49. DOI: http://dx.doi.org/10.5194/os-18-29-2022.

Cohen, L, Hudson, SR, Walden, VP, Graham, RM, Granskog, MA. 2017. Meteorological conditions in a thinner Arctic sea ice regime from winter to summer during the Norwegian Young Sea Ice expedition (N-ICE2015). *Journal of Geophysical Research: Atmospheres* **122**(14): 7235–7259. DOI: http://dx.doi.org/10.1002/2016JD026034.

Cole, ST, Thwaites, FT, Krishfield, RA, Toole, JM. 2015. Processing of velocity observations from Ice-Tethered Profilers. *OCEANS 2015 - MTS/IEEE Washington*. Washington, DC, USA. DOI: http://dx.doi.org/10.23919/OCEANS.2015.7401887.

Cox, CJ, Gallagher, MR, Shupe, MD, Persson, POG, Solomon, A, Fairall, CW, Ayers, T, Blomquist, B, Brooks, IM, Costa, D, Grachev, A, Gottas, D, Hutchings, JK, Kutchenreiter, M, Leach, J, Morris, SM, Morris, V, Osborn, J, Pezoa, S, Preußer, A, Riihimaki, LD, Uttal, T. 2023a: Continuous observations of the surface energy budget and meteorology over the Arctic sea ice during MOSAiC. *Scientific Data* **10***(519)*. DOI: https://dx.doi.org/10.1038/s41597-023-02415-5.

Cox, C, Gallagher, M, Shupe, M, Persson, O, Blomquist, B, Grachev, A, Riihimaki, L, Kutchenreiter, M, Morris, V, Solomon, A, Brooks, I, Costa, D, Gottas, D, Hutchings, J,

1315   Osborn, J, Morris, S, Preusser, A, Uttal, T. 2023b. Met City meteorological and surface
1316   flux measurements (Level 3 Final), Multidisciplinary Drifting Observatory for the Study of
1317   Arctic Climate (MOSAiC), central Arctic, October 2019–September 2020. *NSF Arctic Data*
1318   *Center*. DOI: http://dx.doi.org/10.18739/A2PV6B83F.

1319 Cox, C, Gallagher, M, Shupe, M, Persson, O, Grachev, A, Solomon, A, Ayers, T, Costa, D,
1320   Hutchings, J, Leach, J, Morris, S, Osborn, J, Pezoa, S, Uttal, T. 2023c. Atmospheric
1321   Surface Flux Station #30 measurements (Level 3 Final), Multidisciplinary Drifting
1322   Observatory for the Study of Arctic Climate (MOSAiC), central Arctic, October 2019–
1323   September 2020. *NSF Arctic Data Center*. DOI: http://dx.doi.org/10.18739/A2FF3M18K.

1324 Cox, C, Gallagher, M, Shupe, M, Persson, O, Grachev, A, Solomon, A, Ayers, T, Costa, D,
1325   Hutchings, J, Leach, J, Morris, S, Osborn, J, Pezoa, S, Uttal, T. 2023d. Atmospheric
1326   Surface Flux Station #40 measurements (Level 3 Final), Multidisciplinary Drifting
1327   Observatory for the Study of Arctic Climate (MOSAiC), central Arctic, October 2019–
1328   September 2020. *NSF Arctic Data Center*. DOI: http://dx.doi.org/10.18739/A25X25F0P.

1329 Cox, C, Gallagher, M, Shupe, M, Persson, O, Grachev, A, Solomon, A, Ayers, T, Costa, D,
1330   Hutchings, J, Leach, J, Morris, S, Osborn, J, Pezoa, S, Uttal, T. 2023e. Atmospheric
1331   Surface Flux Station #50 measurements (Level 3 Final), Multidisciplinary Drifting
1332   Observatory for the Study of Arctic Climate (MOSAiC), central Arctic, October 2019–
1333   September 2020. *NSF Arctic Data Center*. DOI: http://dx.doi.org/10.18739/A2XD0R00S.

1334 d'Ovidio, F, De Monte, S, Alvain, S, Dandonneau, Y, Lévy, M. 2010. Fluid dynamical niches of
1335   phytoplankton types. *Proceedings of the National Academy of Sciences* **107**(43): 18366–
1336   18370. DOI: http://dx.doi.org/10.1073/pnas.1004620107.

1337 Danielson, SL, Ahkinga, O, Ashjian, C, Basyuk, E, Cooper, LW, Eisner, L, Farley, E, Iken, KB,
1338   Grebmeier, JM, Juranek, L, Khen, G, Jayne, SR, Kikuchi, T, Ladd, C, Lu, K, McCabe, RM,
1339   Moore, GWK, Nishino, S, Ozenna, F, Pickart, RS, Weingartner, TJ. 2020. Manifestation
1340   and consequences of warming and altered heat fluxes over the Bering and Chukchi Sea
1341   continental shelves. *Deep Sea Research Part II: Topical Studies in Oceanography* **177**:
1342   104781. DOI: http://dx.doi.org/10.1016/j.dsr2.2020.104781.

1343 Dethloff, K, Maslowski, W, Hendricks, S, Lee, Y J, Goessling, H F, Krumpen, T, Haas, C, Handorf,
1344   D, Ricker, R, Bessonov, V, Cassano, J J, Kinney, J C, Osinski, R, Rex, M, Rinke, A,
1345   Sokolova, J, Sommerfeld, A. 2022. Arctic sea ice anomalies during the MOSAiC winter
1346   2019/20. *The Cryosphere* **16**(3): 981–1005. DOI: http://dx.doi.org/10.5194/tc-16-981-
1347   2022.

English, TS. 1961. Some biological observations in the central North Polar Sea Drift Station Alpha, 1957–1958. *Scientific Reports No.* **15:** 1–80. Calgary, AB: Arctic Institute of North America.

Ermold, W, Rigor, I. 2023. In Situ Observations from the International Arctic Buoy Programme (IABP) 2017–2022, Level 1. *NSF Arctic Data Center.* DOI: http://dx.doi.org/10.18739/A20V89J8K.

Falkner, KK, Steele, M, Woodgate, RA, Swift, JH, Aagaard, K, Morison, J. 2005. Dissolved oxygen extrema in the Arctic Ocean halocline from the North Pole to the Lincoln Sea. *Deep Sea Research Part I: Oceanographic Research Papers* **52**(7): 1138–1154. DOI: http://dx.doi.org/10.1016/j.dsr.2005.01.007.

Fang, YC, Rabe, B, Kuznetsov, I, Hoppmann, M, Tippenhauer, S, Regnery, J, He, H, Li, T. n.d. Upper-ocean variability in the Amundsen Basin of the Arctic Ocean during early winter: insights from the MOSAiC expedition. *Elementa: Science of the Anthropocene* (submitted).

Flores, H, Veyssière, G, Castellani, G, Wilkinson, J, Hoppmann, M, Karcher, M, Valcic, L, Cornils, A, Geoffroy, M, Nicolaus M, Niehoff, B, Priou, P, Schmidt, K, Stroeve, J. 2023. Sea-ice decline could keep zooplankton deeper for longer. *Nature Climate Change* **13**(10): 1122–1130. DOI: http://dx.doi.org/10.1038/s41558-023-01779-1.

Fong, AA, Hoppe, CJM, Aberle, N, Ashjian, CJ, Assmy, P, Bai, Y, Bakker, DCE, Balmonte, JP, Barry, KR, Bertilsson, S, Boulton, W, Bowman, J, Bozzato, D, Bratbak, G, Buck, M, Campbell, RG, Castellani, G, Chamberlain, EJ, Chen, J, Chierici, M, Cornils, A, Creamean, JM, Damm, E, Dethloff, K, Droste, ES, Ebenhöh, O, Eggers, SL, Engel, A, Flores, H, Fransson, A, Frickenhaus, S, Gardner, J, Gelfman, CE, Granskog, MA, Graeve, M, Havermans, C, Heuzé, C, Hildebrandt, N, Hill, TCJ, Hoppema, M, Immerz, A, Jin, H, Koch, B, Kong, X, Kraberg, A, Lan, M, Lange, BA, Larsen, A, Lebreton, B, Leu, E, Loose, B, Maslowski, W, Mavis, C, Metfies, K, Mock, T, Müller, O, Nicolaus, M, Niehoff, B, Nomura, D, Nöthig, EM, Oggier, M, Oldenburg, E, Olsen, LM, Peeken, I, Perovich, DK, Popa, O, Rabe, B, Ren, J, Rex, M, Rinke, A, Rokitta, S, Rost, B, Sakinan, S, Salganik, E, Schaafsma, FL, Schäfer, H, Schmidt, K, Shoemaker, KM, Shupe, MD, Snoeijs-Leijonmalm, P, Stefels, J, Svenson, A, Tao, R, Torres-Valdés, S, Torstensson, A, Toseland, A, Ulfsbo, A, Van Leeuwe, MA, Vortkamp, M, Webb, AL, Gradinger, RR. n.d. Overview of the MOSAiC expedition: Ecosystem. *Elementa: Science of the Anthropocene* (submitted). Preprint at DOI: http://dx.doi.org/10.31223/X5P091.

1381 GEBCO Bathymetric Compilation Group 2020. 2020. The GEBCO_2020 Grid – a continuous
1382   terrain model of the global oceans and land. *British Oceanographic Data Centre*, National
1383   Oceanography Centre, NERC, UK. DOI: http://dx.doi.org/10.5285/A29C5465-B138-234D-
1384   E053-6C86ABC040B9.

1385 George, TM, Manucharyan, GE, Thompson, AF. 2021. Deep learning to infer eddy heat fluxes
1386   from sea surface height patterns of mesoscale turbulence. *Nature Communications* **12**(1):
1387   800. DOI: http://dx.doi.org/10.1038/s41467-020-20779-9.

1388 Gimbert, F, Jourdain, NC, Marsan, D, Weiss, J, Barnier, B. 2012. Recent mechanical weakening
1389   of the Arctic sea ice cover as revealed from larger inertial oscillations. *Journal of
1390   Geophysical Research: Oceans* **117**(C11). DOI:
1391   https://dx.doi.org/10.1029/2011JC007633.

1392 Golden, KM, Ackley, SF, Lytle, VI. 1998. The percolation phase transition in sea ice. *Science*
1393   **282**(5397): 2238–2241. DOI: http://dx.doi.org/10.1126/science.282.5397.2238.

1394 Graham, RM, Itkin, P, Meyer, A, Sundfjord, A, Spreen, G, Smedsrud, LH, Liston, GE, Cheng, B,
1395   Cohen, L, Divine, D, Fer, I, Fransson, A, Gerland, S, Haapala, J, Hudson, SR, Johansson,
1396   A M, King, J, Merkouriadi, I, Peterson, AK, Provost, C, Randelhoff, A, Rinke, A, Rösel, A,
1397   Sennéchael, N, Walden, VP, Duarte, P, Assmy, P, Steen, H, Granskog, MA. 2019. Winter
1398   storms accelerate the demise of sea ice in the Atlantic sector of the Arctic Ocean. *Scientific
1399   Reports* **9**(1): 9222. DOI: http://dx.doi.org/10.1038/s41598-019-45574-5.

1400 Granskog MA, Fer I, Rinke A, Steen H. 2018. Atmosphere-ice-ocean-ecosystem processes in a
1401   thinner Arctic sea ice regime: The Norwegian Young Sea ICE (N-ICE2015) Expedition.
1402   *Journal of Geophysical Research: Oceans* **123**(3): 1586–1594. DOI:
1403   http://dx.doi.org/10.1002/2017JC013328.

1404 Granskog, MA, Høyland, KV, De La Torre, PR, Divine, DV, Katlein, C, Itkin, P, Raphael, I, Olsen,
1405   LM. 2020. Temperature and heating induced temperature difference measurements from
1406   the sea ice mass balance buoy SIMBA 2020T60. 4 datasets. *PANGAEA*. DOI:
1407   http://dx.doi.org/10.1594/PANGAEA.924269

1408 Global Runoff Data Centre (GRDC). 2023. Global Freshwater Fluxes into the World's Oceans.
1409   Online provided by Global Runoff Data Centre. Koblenz: Federal Institute of Hydrology
1410   (BfG).

1411 Guiavarc'h, C, Roberts-Jones, J, Harris, C, Lea, DJ, Ryan, A, Ascione, I. 2019. Assessment of
1412   ocean analysis and forecast from an atmosphere–ocean coupled data assimilation
1413   operational system. *Ocean Sciences* **15**(5): 1307–1326. DOI: http://dx.doi.org/10.5194/os-
1414   15-1307-2019.

1415   Guo, W, Itkin, P, Singha, S, Doulgeris, AP, Johansson, M, Spreen, G. 2023. Sea ice classification
1416   of TerraSAR-X ScanSAR images for the MOSAiC expedition incorporating per-class
1417   incidence angle dependency of image texture. *The Cryosphere* **17**(3): 1279–1297. DOI:
1418   http://dx.doi.org/10.5194/tc-17-1279-2023.

1419   Haarsma, RJ, Roberts, MJ, Vidale, PL, Senior, CA, Bellucci, A, Bao, Q, Chang, P, Corti, S,
1420   Fučkar, NS, Guemas, V, Hardenberg, J von, Hazeleger, W, Kodama, C, Koenigk, T,
1421   Leung, LR, Lu, J, Luo, JJ, Mao, J, Mizielinski, MS, Mizuta, R, Nobre, P, Satoh, M,
1422   Scoccimarro, E, Semmler, T, Small, J, von Storch, JS. 2016. High Resolution Model
1423   Intercomparison Project (HighResMIP v1.0) for CMIP6. *Geoscientific Model Development*
1424   **9**(11): 4185–4208. DOI: http://dx.doi.org/10.5194/gmd-9-4185-2016.

1425   Haas C. 2020. Links to master tracks in different resolutions of POLARSTERN cruise PS122/2,
1426   Arctic Ocean – Arctic Ocean, 2019-12-13 – 2020-02-24 (Version 2). *PANGAEA*. DOI:
1427   http://dx.doi.org/10.1594/PANGAEA.924674.

1428   Haine, TWN, Curry, B, Gerdes, R, Hansen, E, Karcher, M, Lee, C, Rudels, B, Spreen, G, de
1429   Steur, L, Stewart, KD, Woodgate, R. 2015. Arctic freshwater export: status, mechanisms,
1430   and   prospects.   *Global   and   Planetary   Change*   **125**:   13–35.   DOI:
1431   http://dx.doi.org/10.1016/j.gloplacha.2014.11.013.

1432   Haine, TWN, Martin, T. 2017. The Arctic - Subarctic sea ice system is entering a seasonal regime:
1433   implications   for   future   Arctic   amplification.   *Scientific   Reports*   **7**(1):   4618.   DOI:
1434   http://dx.doi.org/10.1038/s41598-017-04573-0.

1435   Hatakeyama, K, Hosono, M, Shimada, K, Kikuchi, T, Nishino, S. 2001. JAMSTEC Compact Arctic
1436   Drifter (J-CAD) : A new Generation drifting buoy to observe the Arctic Ocean, *Journal of*
1437   *the   Japan   Society   for   Marine   Surveys   and   Technology*   **13**(1):   55–68.   DOI:
1438   http://dx.doi.org/10.11306/jsmst.13.1_55.

1439   Herber, A, Becker, S, Belter, HJ, Brauchle, J, Ehrlich, A, Klingebiel, M, Krumpen, T, Lüpkes, C,
1440   Mech, M, Moser, M, Wendisch, M. 2021. MOSAiC expedition: airborne surveys with
1441   research aircraft POLAR 5 and POLAR 6 in 2020. *Reports on Polar and Marine Research*
1442   **754**: 1–99. Alfred-Wegener-Institut Helmholtz-Zentrum für Polar- und Meeresforschung.
1443   DOI: http://dx.doi.org/10.48433/BZPM_0754_2021.

1444   Heuzé, C, Zanowski, H, Karam, S, Muilwijk, M. 2023. The deep Arctic Ocean and Fram Strait in
1445   CMIP6 models. *Journal of Climate* **36**: 2551–2584. DOI: http://dx.doi.org/10.1175/JCLI-D-
1446   22-0194.1.

1447 Hoppmann, M, Kuznetsov, I, Fang, YC, Rabe, B. 2021a. Raw seawater temperature, conductivity
1448 and salinity obtained at different depths by CTD buoy 2019O4 as part of the MOSAiC
1449 Distributed Network. *PANGAEA*. DOI: http://dx.doi.org/10.1594/PANGAEA.933933

1450 Hoppmann, M, Kuznetsov, I, Fang, YC, Rabe, B. 2021b. Raw seawater temperature, conductivity
1451 and salinity obtained at different depths by CTD buoy 2019O6 as part of the MOSAiC
1452 Distributed Network. *PANGAEA*. DOI: http://dx.doi.org/10.1594/PANGAEA.933941

1453 Hoppmann, M, Kuznetsov, I, Fang, YC, Rabe, B. 2021c. Raw seawater temperature, conductivity
1454 and salinity obtained at different depths by CTD buoy 2019O7 as part of the MOSAiC
1455 Distributed Network. *PANGAEA*. DOI: http://dx.doi.org/10.1594/PANGAEA.933939

1456 Hoppmann, M, Kuznetsov, I, Fang, YC, Rabe, B. 2022a. Mesoscale observations of temperature
1457 and salinity in the Arctic Transpolar Drift: a high-resolution dataset from the MOSAiC
1458 Distributed Network. *Earth System Science Data* **14**(11): 4901–4921. DOI:
1459 http://dx.doi.org/10.5194/essd-14-4901-2022.

1460 Hoppmann, M, Kuznetsov, I, Fang, YC, Rabe, B. 2022b. Processed data of CTD buoys 2019O1
1461 to 2019O8 as part of the MOSAiC Distributed Network: 8 datasets. *PANGAEA*. DOI:
1462 http://dx.doi.org/10.1594/PANGAEA.940320

1463 Huang, Y, Taylor, PC, Rose, FG, Rutan, DA, Shupe, MD, Webster, MA, Smith, MM. 2022. Toward
1464 a more realistic representation of surface albedo in NASA CERES-derived surface
1465 radiative fluxes. *Elementa: Science of the Anthropocene* **10**(1): 00013. DOI:
1466 http://dx.doi.org/10.1525/elementa.2022.00013.

1467 Hunkins, K. 1967. Inertial oscillations of Fletcher's Ice Island (T-3). *Journal of Geophysical*
1468 *Research* **72**(4): 1165–1174. DOI: http://dx.doi.org/10.1029/JZ072i004p01165.

1469 Hutchings, JK, Heil, P, Steer, A, Hibler III, WD. 2012. Subsynoptic scale spatial variability of sea
1470 ice deformation in the western Weddell Sea during early summer. *Journal of Geophysical*
1471 *Research: Oceans* **117**(C1): 2011JC006961. DOI:
1472 https://dx.doi.org/10.1029/2011JC006961.

1473 Hutchings, JK, Roberts, A, Geiger, CA, Richter-Menge, J. 2011. Spatial and temporal
1474 characterization of sea-ice deformation. *Annals of Glaciology* **52**(57): 360–368. DOI:
1475 http://dx.doi.org/10.3189/172756411795931769.

1476 Hutter, N, Bouchat, A, Dupont, F, Dukhovskoy, D, Koldunov, N, Lee, YJ, Lemieux, JF, Lique, C,
1477 Losch, M, Maslowski, W, Myers, PG, Ólason, E, Rampal, P, Rasmussen, T, Talandier, C,
1478 Tremblay, B, Wang, Q. 2022a. Sea Ice Rheology Experiment (SIREx): 2. Evaluating
1479 Linear Kinematic Features in High-Resolution Sea Ice Simulations. *Journal of Geophysical*

Research: Oceans **127**(4): e2021JC017666. DOI: http://dx.doi.org/10.1029/2021JC017666.

Hutter, N, Hendricks, S, Jutila, A, Birnbaum, G, von Albedyll, L, Ricker, R, Haas, C. 2023. Gridded segments of sea-ice or snow surface elevation and freeboard from helicopter-borne laser scanner during the MOSAiC expedition, Version 1: 64 datasets. *PANGAEA*. DOI: http://dx.doi.org/10.1594/PANGAEA.950339.

Hutter, N, Hendricks, S, Jutila, A, Ricker, R, von Albedyll, L, Birnbaum, G, Haas, C. 2023. Digital elevation models of the sea-ice surface from airborne laser scanning during MOSAiC. *Scientific Data* **10**(1): 729. DOI: http://dx.doi.org/10.1038/s41597-023-02565-6.

Hutter, N., Hendricks, S., Jutila, A., Ricker, R., von Albedyll, L., Birnbaum, G., and Haas, C. (2023): Digital elevation models of the sea-ice surface from airborne laser scanning during MOSAiC. *Scientific Data* **10**(729). DOI: https://dx.doi.org/10.1038/s41597-023-02565-6.

IABP. 2023: https://iabp.apl.uw.edu/, last accessed 30 January, 2024.

Intergovernmental Panel On Climate Change (IPCC). 2022. The Ocean and Cryosphere in a Changing Climate: Special Report of the Intergovernmental Panel on Climate Change. 1st ed. Cambridge University Press. DOI: http://dx.doi.org/10.1017/9781009157964

Itkin, P, Hendricks, S, Webster, M, von Albedyll, L, Arndt, S, Divine, D, Jaggi, M, Oggier, M, Raphael, I, Ricker, R, Rohde, J, Schneebeli, M, Liston, GE. 2023. Sea ice and snow characteristics from year-long transects at the MOSAiC Central Observatory. *Elementa: Science of the Anthropocene* **11**(1): 00048. DOI: http://dx.doi.org/10.1525/elementa.2022.00048.

Itkin, P, Spreen, G, Cheng, B, Doble, M, Girard-Ardhuin, F, Haapala, J, Hughes, N, Kaleschke, L, Nicolaus, M, Wilkinson, J. 2017. Thin ice and storms: sea ice deformation from buoy arrays deployed during N-ICE2015. *Journal of Geophysical Research: Oceans* **122**(6): 4661–4674. DOI: http://dx.doi.org/10.1002/2016JC012403.

Jackson, K, Wilkinson J, Maksym, T, Meldrum, D, Beckers, J, Haas, C, Mackenzie, D. 2013. A novel and low-cost sea ice mass balance buoy. *Journal of Atmospheric and Oceanic Technology* **30**(11): 2676–2688. DOI: http://dx.doi.org/10.1175/JTECH-D-13-00058.1.

Jain, S, Scaife, AA, Shepherd, TG, Deser, C, Dunstone, N, Schmidt, GA, Trenberth, KE, Turkington, T. 2023. Importance of internal variability for climate model assessment. *NPJ Climate and Atmospheric Science* **6**(1): 68. DOI: http://dx.doi.org/10.1038/s41612-023-00389-0.

Jin, M, Deal, C, Maslowski, W, Matrai, P, Roberts, A, Osinski, R, Lee, YJ, Frants, M, Elliott, S, Jeffery, N, Hunke, E, Wang, S. 2018. Effects of model resolution and ocean mixing on

forced ice-ocean physical and biogeochemical simulations using global and regional system models. *Journal of Geophysical Research: Oceans* **123**(1): 358–377. DOI: http://dx.doi.org/10.1002/2017JC013365.

Jonassen, MO, Chechin, D, Karpechko, A, Lüpkes, C, Spengler, T, Tepstra, A, Vihma, T, Zhang, X. 2020a. *Dynamical Processes in the Arctic Atmosphere*. In: Kokhanovsky, A, Tomasi, C, editors. Physics and Chemistry of the Arctic Atmosphere. Cham: Springer International Publishing. pp1–51. DOI: http://dx.doi.org/10.1007/978-3-030-33566-3_1.

Kalnay, E, Kanamitsu, M, Kistler, R, Collins, W, Deaven, D, Gandin, L, Iredell, M, Saha, S, White, G, Woollen, J, Zhu, Y, Chelliah, M, Ebisuzaki, W, Higgins, W, Janowiak, J, Mo, KC, Ropelewski, C, Wang, J, Leetmaa, A, Reynolds, R, Jenne, R, Joseph, D. 1996. The NCEP/NCAR 40-year reanalysis project. *Bulletin of the American Meteorological Society* **77**(3): 437–471. DOI: http://dx.doi.org/10.1175/1520-0477(1996)077<0437:TNYRP>2.0.CO;2.

Kanzow, T. 2020. Links to master tracks in different resolutions of POLARSTERN cruise PS122/3, Arctic Ocean – Longyearbyen, 2020-02-24 – 2020-06-04 (Version 2). *PANGAEA*. DOI: http://dx.doi.org/10.1594/PANGAEA.924681.

Katlein, C, Mohrholz, V, Sheikin, I, Itkin, P, Divine, DV, Stroeve, J, Jutila, A, Krampe, D, Shimanchuk, E, Raphael, I, Rabe, B, Kuznetsov, I, Mallet, M, Liu, H, Hoppmann, M, Fang, YC, Dumitrascu, A, Arndt, S, Anhaus, P, Nicolaus, M, Matero, I, Oggier, M, Eicken, H, Haas, C. 2020. Platelet ice under Arctic pack ice in winter. *Geophysical Research Letters* **47**(16). DOI: http://dx.doi.org/10.1029/2020GL088898.

Kawaguchi, Y, Koenig, Z, Nomura, D, Hoppmann, M, Inoue, J, Fang, YC, Schulz, K, Gallagher, M, Katlein, C, Nicolaus, M, Rabe, B. 2022. Turbulent mixing during late summer in the ice–ocean boundary layer in the central Arctic Ocean: results from the MOSAiC expedition. *Journal of Geophysical Research: Oceans* **127**(8): e2021JC017975. DOI: http://dx.doi.org/10.1029/2021JC017975.

Kay, JE, L'Ecuyer, T, Chepfer, H, Loeb, N, Morrison, A, Cesana, G. 2016. Recent advances in Arctic cloud and climate research. *Current Climate Change Reports* **2**(4): 159–169. DOI: http://dx.doi.org/10.1007/s40641-016-0051-9.

Kikuchi, T, Inoue, J, Langevin, D. 2007. Argo-type profiling float observations under the Arctic multiyear ice. *Deep Sea Research Part I: Oceanographic Research Papers* **54**(9): 1675–1686. DOI: http://dx.doi.org/10.1016/j.dsr.2007.05.011.

Koenig, Z, Provost, C, Villacieros-Robineau, N, Sennéchael, N, Meyer, A. 2016. Winter ocean-ice interactions under thin sea ice observed by IAOOS platforms during N-ICE2015: Salty

surface mixed layer and active basal melt: *Journal of Geophysical Research: Oceans* **121**(10): 7898–7916. DOI: http://dx.doi.org/10.1002/2016JC012195.

Koenigk, T, Mikolajewicz, U, Haak, H, Jungclaus, J. 2007. Arctic freshwater export in the 20th and 21st centuries. *Journal of Geophysical Research: Biogeosciences* **112**(G4). DOI: http://dx.doi.org/10.1029/2006JG000274.

Koo, Y, Lei, R, Cheng, Y, Cheng, B, Xie, H, Hoppmann, M, Kurtz, NT, Ackley, SF, Mestas-Nuñez, AM. 2021. Estimation of thermodynamic and dynamic contributions to sea ice growth in the Central Arctic using ICESat-2 and MOSAiC SIMBA buoy data. *Remote Sensing of Environment* **267**: 112730. DOI: http://dx.doi.org/10.1016/j.rse.2021.112730.

Korhonen, M, Rudels, B, Marnela, M, Wisotzki, A, Zhao, J. 2013. Time and space variability of freshwater content, heat content and seasonal ice melt in the Arctic Ocean from 1991 to 2011. *Ocean Science* **9**(6): 1015–1055. DOI: http://dx.doi.org/10.5194/os-9-1015-2013.

Krishfield, R, Toole, J, Proshutinsky, A, Timmermans, ML. 2008. Automated Ice-Tethered Profilers for seawater observations under pack ice in all seasons. *Journal of Atmospheric and Oceanic Technology* **25**(11): 2091–2105. DOI: http://dx.doi.org/10.1175/2008JTECHO587.1.

Krueger, F, Rackow, T. 2020. The (drawn) Distributed Network around Polarstern, MOSAiC expedition. *Zenodo*. DOI: http://dx.doi.org/10.5281/ZENODO.3696854.

Krumpen, T, Birrien, F, Kauker, F, Rackow, T, von Albedyll, L, Angelopoulos, M, Belter, HJ, Bessonov, V, Damm, E, Dethloff, K, Haapala, J, Haas, C, Harris, C, Hendricks, S, Hoelemann, J, Hoppmann, M, Kaleschke, L, Karcher, M, Kolabutin, N, Lei, R, Lenz, J, Morgenstern, A, Nicolaus, M, Nixdorf, U, Petrovsky, T, Rabe, B, Rabenstein, L, Rex, M, Ricker, R, Rohde, J, Shimanchuk, E, Singha, S, Smolyanitsky, V, Sokolov, V, Stanton, T, Timofeeva, A, Tsamados, M, Watkins, D. 2020. The MOSAiC ice floe: sediment-laden survivor from the Siberian shelf. *The Cryosphere* **14**(7): 2173–2187. DOI: http://dx.doi.org/10.5194/tc-14-2173-2020.

Krumpen, T, von Albedyll, L, Goessling, HF, Hendricks, S, Juhls, B, Spreen, G, Willmes, S, Belter, HJ, Dethloff, K, Haas, C, Kaleschke, L, Katlein, C, Tian-Kunze, X, Ricker, R, Rostosky, P, Rückert, J, Singha, S, Sokolova, J. 2021. MOSAiC drift expedition from October 2019 to July 2020: sea ice conditions from space and comparison with previous years. *The Cryosphere* **15**(8): 3897–3920. DOI: http://dx.doi.org/10.5194/tc-15-3897-2021.

Kuznetsov, I, Rabe, B, Androsov, A, Fang, YC, Hoppmann, M, Quintanilla-Zurita, A, Harig, S, Tippenhauer, S, Schulz, K, Mohrholz, V, Fer, I, Fofonova, V, Janout, M. n.d. Dynamical reconstruction of the upper-ocean state in the central Arctic during the winter period of the

51

MOSAiC expedition. *EGUsphere preprint.* DOI: http://dx.doi.org/10.5194/egusphere-2023-1353.

Kwok R. 2001. Deformation of the Arctic Ocean sea ice cover between November 1996 and April 1997: A qualitative survey. In: Dempsey JP, Shen HH, editors. *IUTAM Symposium on Scaling Laws in Ice Mechanics and Ice Dynamics*. Dordrecht: Springer Netherlands. pp. 315–322. DOI: http://dx.doi.org/10.1007/978-94-015-9735-7_26.

Laney, SR, Krishfield, RA, Toole, JM, Hammar, TR, Ashjian, CJ, Timmermans, ML. 2014. Assessing algal biomass and bio-optical distributions in perennially ice-covered polar ocean ecosystems. *Polar Science* **8**(2): 73–85. DOI: http://dx.doi.org/10.1016/j.polar.2013.12.003.

Lee, CM, DeGrandpre, M, Guthrie, J, Hill, V, Kwok, R, Morison, J, Cox, C, Singh, H, Stanton, T, Wilkinson, J. 2022. Emerging technologies and approaches for in situ, autonomous observing in the Arctic. *Oceanography* **35**(3–4): 210–221. DOI: http://dx.doi.org/10.5670/oceanog.2022.127.

Lee, CM, Thomson, J, the Marginal Ice Zone Team, the Arctic Sea State Team. 2017. An autonomous approach to observing the seasonal ice zone in the western Arctic. *Oceanography* **30**(2): 56–68. DOI: http://dx.doi.org/10.5670/oceanog.2017.222.

Lei, R, Cheng, B, Hoppmann, M, Haapala, J, Lan, M. 2022b. Temperature and heating induced temperature difference measurements from SIMBA-type sea ice mass balance buoy 2019T56, deployed during MOSAiC 2019/20: 4 datasets. *PANGAEA*. DOI: http://dx.doi.org/10.1594/PANGAEA.940360.

Lei, R, Cheng, B, Hoppmann, M, Zhang, F, Zuo, G, Hutchings, JK, Lin, L, Lan, M, Wang, H, Regnery, J, Krumpen, T, Haapala, J, Rabe, B, Perovich, DK, Nicolaus, M. 2022a. Seasonality and timing of sea ice mass balance and heat fluxes in the Arctic transpolar drift during 2019–2020. *Elementa: Science of the Anthropocene* **10**(1): 000089. DOI: http://dx.doi.org/10.1525/elementa.2021.000089.

Lei, R, Cheng, B, Hoppmann, M, Zuo, G, Lan, M. 2022g. Temperature and heating induced temperature difference measurements from SIMBA-type sea ice mass balance buoy 2019T62, deployed during MOSAiC 2019/20: 4 datasets. *PANGAEA*. DOI: http://dx.doi.org/10.1594/PANGAEA.940231.

Lei, R, Cheng, B, Hoppmann M, Zuo, G. 2021b. Temperature and heating induced temperature difference measurements from SIMBA-type sea ice mass balance buoy 2019T66, deployed during MOSAiC 2019/20: 4 datasets. *PANGAEA*. DOI: http://dx.doi.org/10.1594/PANGAEA.938134.

1616 Lei, R, Cheng, B, Hoppmann, M, Zuo, G. 2021c. Temperature and heating induced temperature
1617   difference measurements from SIMBA-type sea ice mass balance buoy 2019T67,
1618   deployed   during   MOSAiC   2019/20:   4   datasets.   *PANGAEA*.   DOI:
1619   http://dx.doi.org/10.1594/PANGAEA.938128.

1620 Lei, R, Cheng, B, Hoppmann, M, Zuo, G. 2021d. Temperature and heating induced temperature
1621   difference measurements from SIMBA-type sea ice mass balance buoy 2019T69,
1622   deployed   during   MOSAiC   2019/20:   4   datasets.   *PANGAEA*.   DOI:
1623   http://dx.doi.org/10.1594/PANGAEA.938096.

1624 Lei, R, Cheng, B, Hoppmann, M, Zuo, G. 2022c. Temperature and heating induced temperature
1625   difference measurements from SIMBA-type sea ice mass balance buoy 2019T58,
1626   deployed   during   MOSAiC   2019/20:   4   datasets.   *PANGAEA*.   DOI:
1627   http://dx.doi.org/10.1594/PANGAEA.940393.

1628 Lei, R, Cheng, B, Hoppmann, M, Zuo, G. 2022d. Temperature and heating induced temperature
1629   difference measurements from SIMBA-type sea ice mass balance buoy 2019T64,
1630   deployed   during   MOSAiC   2019/20:   4   datasets.   *PANGAEA*.   DOI:
1631   http://dx.doi.org/10.1594/PANGAEA.940617.

1632 Lei, R, Cheng, B, Hoppmann, M, Zuo, G. 2022e. Temperature and heating induced temperature
1633   difference measurements from SIMBA-type sea ice mass balance buoy 2019T68,
1634   deployed   during   MOSAiC   2019/20:   4   datasets.   *PANGAEA*.   DOI:
1635   http://dx.doi.org/10.1594/PANGAEA.940650.

1636 Lei, R, Cheng, B, Hoppmann, M, Zuo, G. 2022f. Temperature and heating induced temperature
1637   difference measurements from SIMBA-type sea ice mass balance buoy 2019T72,
1638   deployed   during   MOSAiC   2019/20:   4   datasets.   *PANGAEA*.   DOI:
1639   http://dx.doi.org/10.1594/PANGAEA.940668.

1640 Lei, R, Cheng, B, Zuo, G, Hoppmann, M, Lan, M. 2022k. Temperature and heating induced
1641   temperature difference measurements from SIMBA-type sea ice mass balance buoy
1642   2019T70, deployed during MOSAiC 2019/20: 4 datasets. *PANGAEA*. DOI:
1643   http://dx.doi.org/10.1594/PANGAEA.940659.

1644 Lei, R, Cheng, B, Zuo, G, Hoppmann, M. 2022h. Temperature and heating induced temperature
1645   difference measurements from SIMBA-type sea ice mass balance buoy 2019T47,
1646   deployed   during   MOSAiC   2019/20:   4   datasets.   *PANGAEA*.   DOI:
1647   http://dx.doi.org/10.1594/PANGAEA.940387.

1648 Lei, R, Cheng, B, Zuo G, Hoppmann, M. 2022i. Temperature and heating induced temperature
1649   difference measurements from SIMBA-type sea ice mass balance buoy 2019T63,

1650   deployed during MOSAiC 2019/20: 4 datasets. *PANGAEA*. DOI:
1651   http://dx.doi.org/10.1594/PANGAEA.940593.

1652   Lei, R, Cheng, B, Zuo, G, Hoppmann, M. 2022j. Temperature and heating induced temperature
1653   difference measurements from SIMBA-type sea ice mass balance buoy 2019T65,
1654   deployed during MOSAiC 2019/20: 4 datasets. PANGAEA. DOI:
1655   http://dx.doi.org/10.1594/PANGAEA.940634.

1656   Lei, R, Hutchings, JK, Cheng, B, Hoppmann, M. 2022l. Temperature and heating induced
1657   temperature difference measurements from SIMBA-type sea ice mass balance buoy
1658   2020T75, deployed during MOSAiC 2019/20: 4 datasets. PANGAEA. DOI:
1659   http://dx.doi.org/10.1594/PANGAEA.940740.

1660   Lei, R, Hutchings, JK, Hoppmann, M, Yuan, Z. 2022m. Temperature and heating induced
1661   temperature difference measurements from SIMBA-type sea ice mass balance buoy
1662   2020T79, deployed during MOSAiC 2019/20: 4 datasets. PANGAEA. DOI:
1663   http://dx.doi.org/10.1594/PANGAEA.940712.

1664   Lei, R, Hutchings, JK, Watkins, D, Hoppmann, M. 2021a. Sea ice drift from autonomous
1665   measurements from buoy 2020P225, deployed during MOSAiC 2019/20. PANGAEA.
1666   DOI: http://dx.doi.org/10.1594/PANGAEA.939043.

1667   Levy, M, Martin, AP. 2013. The influence of mesoscale and submesoscale heterogeneity on
1668   ocean biogeochemical reactions. *Global Biogeochemical Cycles* **27**(4): 1139–1150. DOI:
1669   http://dx.doi.org/10.1002/2012GB004518.

1670   Li, G, Cheng, L, Zhu, J, Trenberth, KE, Mann, ME, Abraham, JP. 2020. Increasing ocean
1671   stratification over the past half-century. *Nature Climate Change* **10**(12): 1116–1123. DOI:
1672   http://dx.doi.org/10.1038/s41558-020-00918-2.

1673   Li, T, Zhu, J, Zhai, L. 2021b. Drift Towing Ocean Profiler (DTOP) data on sea ice, meteorological
1674   conditions and drift of sea ice from buoy 2019V1, deployed during MOSAiC 2019/20: 2
1675   datasets. *PANGAEA*. DOI: http://dx.doi.org/10.1594/PANGAEA.937212.

1676   Li, T, Zhu, J, Zhai, L. 2021c. Drift Towing Ocean Profiler (DTOP) data on sea ice, meteorological
1677   conditions and drift of sea ice from buoy 2019V2, deployed during MOSAiC 2019/20: 2
1678   datasets. *PANGAEA*. DOI: http://dx.doi.org/10.1594/PANGAEA.937940.

1679   Li, T, Zhu, J, Zhai, L. 2021d. Drift Towing Ocean Profiler (DTOP) data on sea ice, meteorological
1680   conditions and drift of sea ice from buoy 2019V4, deployed during MOSAiC 2019/20: 2
1681   datasets. *PANGAEA*. DOI: http://dx.doi.org/10.1594/PANGAEA.937949.

1682 Li, T, Zhu, J, Zhai, L. 2021a. Ocean data of the Drift Towing Ocean Profiler (DTOP) data on sea
1683   ice, meteorological conditions and drift of sea ice from buoy 2019V5. *PANGAEA*. DOI:
1684   http://dx.doi.org/10.1594/PANGAEA.937955.

1685 Light, B, Smith, MM, Perovich, DK, Webster, MA, Holland, MM, Linhardt, F, Raphael, IA,
1686   Clemens-Sewall, D, Macfarlane, AR, Anhaus, P, Bailey, DA. 2022. Arctic sea ice albedo:
1687   Spectral composition, spatial heterogeneity, and temporal evolution observed during the
1688   MOSAiC drift. *Elementa: Science of the Anthropocene* **10**(1): 000103. DOI:
1689   http://dx.doi.org/10.1525/elementa.2021.000103.

1690 Lindsay, R, Schweiger, A. 2015. Arctic sea ice thickness loss determined using subsurface,
1691   aircraft, and satellite observations. *The Cryosphere* **9**(1): 269–283. DOI:
1692   http://dx.doi.org/10.5194/tc-9-269-2015.

1693 Mahadevan, A. 2016. The impact of submesoscale physics on primary productivity of plankton.
1694   *Annual Review of Marine Science* **8**(1): 161–184. DOI: http://dx.doi.org/10.1146/annurev-
1695   marine-010814-015912.

1696 Manucharyan, GE, Thompson, AF. 2017. Submesoscale sea ice-ocean interactions in marginal
1697   ice zones. *Journal of Geophysical Research: Oceans* **122**(12): 9455–9475. DOI:
1698   http://dx.doi.org/10.1002/2017JC012895.

1699 Marsan, D, Stern, H, Lindsay, R, Weiss, J. 2004. Scale dependence and localization of the
1700   deformation of Arctic sea ice. *Physical Review Letters* **93**(17). DOI:
1701   http://dx.doi.org/10.1103/PhysRevLett.93.178501.

1702 Maslowski, W, Clement Kinney, J, Higgins, M, Roberts, A. 2012. The future of Arctic sea ice.
1703   *Annual Review of Earth and Planetary Sciences* **40**(1): 625–654. DOI:
1704   http://dx.doi.org/10.1146/annurev-earth-042711-105345.

1705 Maykut, GA, Untersteiner, N. 1971. Some results from a time-dependent thermodynamic model
1706   of sea ice. *Journal of Geophysical Research* **76**(6): 1550–1575. DOI:
1707   http://dx.doi.org/10.1029/JC076i006p01550.

1708 Maykut, GA. 1978. Energy exchange over young sea ice in the central Arctic. *Journal of
1709   Geophysical Research* **83**(C7): 3646–3658. DOI:
1710   http://dx.doi.org/10.1029/JC083iC07p03646.

1711 McDougall, TJ, Barker, PM. 2011. Getting started with TEOS-10 and the Gibbs Seawater (GSW)
1712   Oceanographic Toolbox. SCOR/IAPSO WG127.

1713 McDougall, TJ, Feistel, R, Millero, F, Jackett, DR, Wright, D, King, B, Marion, G, Chen, CTA,
1714   Spitzer, P. 2010. The international thermodynamic equation of seawater – 2010:

1715   calculation and use of thermodynamic properties. Paris: 196 S. *IOC Manuals and guides*
1716   *56*. http://unesdoc.unesco.org/images/0018/001881/188170e.pdf.

1717 McPhee, MG. 1978. A simulation of inertial oscillation in drifting pack ice. *Dynamics of*
1718   *Atmospheres and Oceans* **2**(2): 107–122. DOI: http://dx.doi.org/10.1016/0377-
1719   0265(78)90005-2.

1720 Mortenson, E, Steiner, N, Monahan, AH, Hayashida, H, Sou, T, Shao, A. 2020. Modeled impacts
1721   of sea ice exchange processes on Arctic Ocean carbon uptake and acidification (1980–
1722   2015). *Journal of Geophysical Research: Oceans* **125**(7). DOI:
1723   http://dx.doi.org/10.1029/2019JC015782.

1724 MOSAiC Consortium. 2016. MOSAiC Science Plan. Eprint ID 56333,
1725   https://epic.awi.de/id/eprint/56616/, last accessed June 30, 2023.

1726 MOSAiC Consortium. 2018. MOSAiC Implementation Plan. Eprint ID 56333,
1727   https://epic.awi.de/id/eprint/56333/ , last accessed June 30, 2023.

1728 NASA. 2023. NASA Goddard Space Flight Center, Ocean Ecology Laboratory, Ocean Biology
1729   Processing Group. Moderate-resolution Imaging Spectroradiometer (MODIS) Aqua Data;
1730   NASA OB.DAAC, Greenbelt, MD, USA. Accessed on January 01, 2018; see also
1731   https://oceancolor.gsfc.nasa.gov/.

1732 Neckel, N, Fuchs, N, Birnbaum, G, Hutter, N, Jutila, A, Buth, L, von Albedyll, L, Ricker, R, Haas,
1733   C. 2023. Helicopter-borne RGB orthomosaics and photogrammetric digital elevation
1734   models from the MOSAiC Expedition. *Scientific Data* **10**(1): 426. DOI:
1735   http://dx.doi.org/10.1038/s41597-023-02318-5.

1736 Nicolaus, M, Hoppmann, M, Arndt, S, Hendricks, S, Katlein, C, Nicolaus, A, Rossmann, L, Schiller,
1737   M, Schwegmann, S. 2021a. Snow depth and air temperature seasonality on sea ice
1738   derived from Snow Buoy measurements. *Frontiers in Marine Science* **8**: 655446. DOI:
1739   http://dx.doi.org/10.3389/fmars.2021.655446.

1740 Nicolaus, M, Hoppmann, M, Lei, R, Belter, HJ, Fang, YC, Rohde, J. 2020a. Snow height on sea
1741   ice, meteorological conditions and drift of sea ice from autonomous measurements from
1742   buoy 2019S81, deployed during MOSAiC 2019/20. *PANGAEA*. DOI:
1743   http://dx.doi.org/10.1594/PANGAEA.925312.

1744 Nicolaus, M, Hoppmann, M, Lei, R, Belter, HJ, Fang, YC, Rohde, J. 2020b. Snow height on sea
1745   ice, meteorological conditions and drift of sea ice from autonomous measurements from
1746   buoy 2019S94, deployed during MOSAiC 2019/20. *PANGAEA*. DOI:
1747   http://dx.doi.org/10.1594/PANGAEA.925325.

1748 Nicolaus, M, Perovich, DK, Spreen, G, Granskog, MA, von Albedyll, L, Angelopoulos, M, Anhaus,
1749   P, Arndt, S, Belter, HJ, Bessonov, V, Birnbaum, G, Brauchle, J, Calmer, R, Cardellach, E,
1750   Cheng, B, Clemens-Sewall, D, Dadic, R, Damm, E, de Boer, G, Demir, O, Dethloff, K,
1751   Divine, DV, Fong, AA, Fons, S, Frey, MM, Fuchs, N, Gabarró, C, Gerland, S, Goessling,
1752   HF, Gradinger, R, Haapala, J, Haas, C, Hamilton, J, Hannula, HR, Hendricks, S, Herber,
1753   A, Heuzé, C, Hoppmann, M, Høyland, KV, Huntemann, M, Hutchings, JK, Hwang, B, Itkin,
1754   P, Jacobi, HW, Jaggi, M, Jutila, A, Kaleschke, L, Katlein, C, Kolabutin, N, Krampe, D,
1755   Kristensen, SS, Krumpen, T, Kurtz, N, Lampert, A, Lange, BA, Lei, R, Light, B, Linhardt,
1756   F, Liston, GE, Loose, B, Macfarlane, AR, Mahmud, M, Matero, IO, Maus, S, Morgenstern,
1757   A, Naderpour, R, Nandan, V, Niubom, A, Oggier, M, Oppelt, N, Pätzold, F, Perron, C,
1758   Petrovsky, T, Pirazzini, R, Polashenski, C, Rabe, B, Raphael, IA, Regnery, J, Rex, M,
1759   Ricker, R, Riemann-Campe, K, Rinke, A, Rohde, J, Salganik, E, Scharien, RK, Schiller,
1760   M, Schneebeli, M, Semmling, M, Shimanchuk, E, Shupe, MD, Smith, MM, Smolyanitsky,
1761   V, Sokolov, V, Stanton, T, Stroeve, J, Thielke, L, Timofeeva, A, Tonboe, RT, Tavri, A,
1762   Tsamados, M, Wagner, DN, Watkins, D, Webster, M, Wendisch, M. 2022. Overview of the
1763   MOSAiC expedition: snow and sea ice. *Elementa: Science of the Anthropocene* **10**(1):
1764   000046. DOI: http://dx.doi.org/10.1525/elementa.2021.000046.
1765 Nicolaus, M, Riemann-Campe, K, Bliss, A, Hutchings, JK, Granskog, MA, Haas, C, Hoppmann,
1766   M, Kanzow, T, Krishfield, RA, Lei, R, Rex, M, Tao, L, Rabe, B. 2021b. Drift trajectories of
1767   the main sites of the Distributed Network of MOSAiC 2019/2020: 15 datasets. *PANGAEA*.
1768   DOI: http://dx.doi.org/10.1594/PANGAEA.937204.
1769 Nixdorf, U, Dethloff, K, Rex, M, Shupe, M, Sommerfeld, A, Perovich, DK, Nicolaus, M, Heuzé, C,
1770   Rabe, B, Loose, B, Damm, E, Gradinger, R, Fong, A, Maslowski, W, Rinke, A, Kwok, R,
1771   Spreen, G, Wendisch, M, Herber, A, Hirsekorn, M, Mohaupt, V, Frickenhaus, S, Immerz,
1772   A, Weiss-Tuider, K, König, B, Mengedoht, D, Regnery, J, Gerchow, P, Ransby, D,
1773   Krumpen, T, Morgenstern, A, Haas, C, Kanzow, T, Rack, FR, Saitzev, V, Sokolov, V,
1774   Makarov, A, Schwarze, S, Wunderlich, T, Wurr, K, Boetius, A. 2021. MOSAiC Extended
1775   Acknowledgement. *Zenodo*. DOI: http://dx.doi.org/10.5281/ZENODO.5179738.
1776 Notz, D, Wettlaufer, JS, Worster, MG. 2005. A non-destructive method for measuring the salinity
1777   and solid fraction of growing sea ice in situ. *Journal of Glaciology* **51**(172): 159–166. DOI:
1778   http://dx.doi.org/10.3189/172756505781829548.
1779 Nurser, AJG, Bacon, S. 2014. The Rossby radius in the Arctic Ocean. *Ocean Science* **10**(6): 967–
1780   975. DOI: http://dx.doi.org/10.5194/os-10-967-2014.

1781 Oikkonen, A, Haapala, J, Lensu, M, Karvonen, J, Itkin, P. 2017. Small-scale sea ice deformation
1782   during N-ICE2015: From compact pack ice to marginal ice zone. *Journal of Geophysical*
1783   *Research: Oceans* **122**(6): 5105–5120. DOI: http://dx.doi.org/10.1002/2016JC012387.

1784 Ocean University of China. 2024: Drift-Towing Ocean Profiler.
1785   http://coas.ouc.edu.cn/pogoc/2021/0713/c9714a342585/page.htm, last accessed on
1786   January 30, 2024.

1787 Perovich, DK, Meier, W, Tschudi, M, Hendricks, S, Petty, AA, Divine, D, Farrell, S, Gerland, S,
1788   Haas, C, Kaleschke, L, Pavlova, O, Ricker, R, Tian-Kunze, X, Webster, M, Wood, K. 2020.
1789   Arctic Report Card 2020: Sea Ice. *Series: Arctic Report Card.* DOI:
1790   http://dx.doi.org/10.25923/N170-9H57.

1791 Perovich, DK, Raphael, I, Moore, R, Clemens-Sewall, D, Lei, R, Sledd, A, Polashenski, C. 2023.
1792   Sea ice heat and mass balance measurements from four autonomous buoys during the
1793   MOSAiC drift campaign. *Elementa: Science of the Anthropocene* **11**(1): 00017. DOI:
1794   http://dx.doi.org/10.1525/elementa.2023.00017.

1795 Perovich, DK, Richter-Menge, J, Polashenski, C, Elder, B, Arbetter, T, Brennick, O. 2014. Sea ice
1796   mass balance observations from the North Pole Environmental Observatory. *Geophysical*
1797   *Research Letters* **41**(6): 2019–2025. DOI: http://dx.doi.org/10.1002/2014GL059356.

1798 Perovich, DK, Andreas, EL, Curry, JA, Eiken, H, Fairall, CW, Grenfell, TC, Guest, PS, Intrieri, J,
1799   Kadko, D, Lindsay, RW, McPhee, MG, Morison, J, Moritz, RE, Paulson, CA, Pegau, WS,
1800   Persson, POG, Pinkel, R, Richter-Menge, JA, Stanton, T, Stern, H, Sturm, M, Tucker, W
1801   B III, Uttal, T. 1999. Year on ice gives climate insights. *Eos Transactions* **80**(41): 481. DOI:
1802   http://dx.doi.org/10.1029/EO080i041p00481-01.

1803 Perovich, DK, Elder, B. 2002. Estimates of ocean heat flux at SHEBA. *Geophysical Research*
1804   *Letters* **29**(9): 58-1-58–4. DOI: http://dx.doi.org/10.1029/2001GL014171.

1805 Persson, POG, Fairall, CW, Andreas, EL, Guest, PS, Perovich, DK. 2002. Measurements near
1806   the Atmospheric Surface Flux Group tower at SHEBA: Near-surface conditions and
1807   surface energy budget. *Journal of Geophysical Research: Oceans* **107**(C10). DOI:
1808   http://dx.doi.org/10.1029/2000JC000705.

1809 Persson, POG, Shupe, MD, Perovich, D, Solomon, A. 2017. Linking atmospheric synoptic
1810   transport, cloud phase, surface energy fluxes, and sea-ice growth: observations of
1811   midwinter SHEBA conditions. *Climate Dynamics* **49**(4): 1341–1364. DOI:
1812   http://dx.doi.org/10.1007/s00382-016-3383-1.

1813 Persson, POG. 2012. Onset and end of the summer melt season over sea ice: thermal structure
1814   and surface energy perspective from SHEBA. *Climate Dynamics* **39**(6): 1349–1371. DOI:
1815   http://dx.doi.org/10.1007/s00382-011-1196-9.

1816 Pithan, F, Athanase, M, Dahlke, S, Sánchez-Benítez, A, Shupe, MD, Sledd, A, Streffing, J,
1817   Svensson, G, Jung, T. 2023. Nudging allows direct evaluation of coupled climate models
1818   with in situ observations: a case study from the MOSAiC expedition. *Geoscientific Model*
1819   *Development* **16**(7): 1857–1873. DOI: http://dx.doi.org/10.5194/gmd-16-1857-2023.

1820 Planck, CJ, Whitlock, J, Polashenski, C, Perovich, DK. 2019. The evolution of the seasonal ice
1821   mass balance buoy. *Cold Regions Science and Technology* **165**: 102792. DOI:
1822   http://dx.doi.org/10.1016/j.coldregions.2019.102792.

1823 Polyakov, GV, Pnyushkov, AV, Alkire, M B, Ashik, IM, Baumann, TM, Carmack, EC, Goszczko,
1824   I, Guthrie, J, Ivanov, VV, Kanzow, T, Krishfield, R, Kwok, R, Sundfjord, A, Morison, J,
1825   Rember, R, Yulin, A. 2017. Greater role for Atlantic inflows on sea-ice loss in the Eurasian
1826   Basin of the Arctic Ocean. *Science* **356**(6335): 285–291. DOI:
1827   http://dx.doi.org/10.1126/science.aai8204.

1828 Rabe, B, Heuzé, C, Regnery, J, Aksenov, Y, Allerholt, J, Athanase, M, Bai, Y, Basque, C, Bauch,
1829   D, Baumann, TM, Chen, D, Cole, ST, Craw, L, Davies, A, Damm, E, Dethloff, K, Divine,
1830   DV, Doglioni, F, Ebert, F, Fang, YC, Fer, I, Fong, AA, Gradinger, R, Granskog, MA,
1831   Graupner, R, Haas, C, He, H, He, Y, Hoppmann, M, Janout, M, Kadko, D, Kanzow, T,
1832   Karam, S, Kawaguchi, Y, Koenig, Z, Kong, B, Krishfield, RA, Krumpen, T, Kuhlmey, D,
1833   Kuznetsov, I, Lan, M, Laukert, G, Lei, R, Li, T, Torres-Valdés, S, Lin, L, Lin, L, Liu, H, Liu,
1834   N, Loose, B, Ma, X, McKay, R, Mallet, M, Mallett, RDC, Maslowski, W, Mertens, C,
1835   Mohrholz, V, Muilwijk, M, Nicolaus, M, O'Brien, JK, Perovich, DK, Ren, J, Rex, M, Ribeiro,
1836   N, Rinke, A, Schaffer, J, Schuffenhauer, I, Schulz, K, Shupe, MD, Shaw, W, Sokolov, V,
1837   Sommerfeld, A, Spreen, G, Stanton, T, Stephens, M, Su, J, Sukhikh, N, Sundfjord, A,
1838   Thomisch, K, Tippenhauer, S, Toole, JM, Vredenborg, M, Walter, M, Wang, H, Wang, L,
1839   Wang, Y, Wendisch, M, Zhao, J, Zhou, M, Zhu, J. 2022. Overview of the MOSAiC
1840   expedition: Physical oceanography. *Elementa: Science of the Anthropocene* **10**(1): 00062.
1841   DOI: http://dx.doi.org/10.1525/elementa.2021.00062.

1842 Rabe, B, Karcher, M, Schauer, U, Toole, J, Krishfield, R, Pisarev, S, Kauker, F, Gerdes, R,
1843   Kikuchi, T. 2011. An assessment of Arctic Ocean freshwater content changes from the
1844   1990s to 2006–2008. *Deep-Sea Research Part I: Oceanographic Research Papers* **58**(2):
1845   173–185. DOI: http://dx.doi.org/10.1016/j.dsr.2010.12.002.

1846   Rackow, T, Sein, DV, Semmler, T, Danilov, S, Koldunov, NV, Sidorenko, D, Wang, Q, Jung, T.
1847   2019. Sensitivity of deep ocean biases to horizontal resolution in prototype CMIP6
1848   simulations with AWI-CM1.0. *Geoscientific Model Development* **12**(7): 2635–2656. DOI:
1849   http://dx.doi.org/10.5194/gmd-12-2635-2019.

1850   Rantanen, M, Karpechko, AY, Lipponen, A, Nordling, K, Hyvärinen, O, Ruosteenoja, K, Vihma,
1851   T, Laaksonen, A. 2022. The Arctic has warmed nearly four times faster than the globe
1852   since 1979. *Communications Earth and Environment* **3**(1): 168. DOI:
1853   http://dx.doi.org/10.1038/s43247-022-00498-3.

1854   Rennermalm, AK, Wood, EF, Weaver, AJ, Eby, M, Déry, SJ. 2007. Relative sensitivity of the
1855   Atlantic meridional overturning circulation to river discharge into Hudson Bay and the
1856   Arctic Ocean. *Journal of Geophysical Research: Biogeosciences* **112**(G4). DOI:
1857   http://dx.doi.org/10.1029/2006JG000330.

1858   Rex, M. 2020. Links to master tracks in different resolutions of POLARSTERN cruise PS122/1,
1859   Tromsø – Arctic Ocean, 2019-09-20 – 2019-12-13 (Version 2). *PANGAEA*. DOI:
1860   http://dx.doi.org/10.1594/PANGAEA.924668

1861   Rex, M. 2021a. Master tracks in different resolutions of POLARSTERN cruise PS122/4,
1862   Longyearbyen – Arctic Ocean, 2020-06-04 – 2020-08-12. *PANGAEA*. DOI:
1863   http://dx.doi.org/10.1594/PANGAEA.926829

1864   Rex, M. 2021b. Master tracks in different resolutions of POLARSTERN cruise PS122/5, Arctic
1865   Ocean – Bremerhaven, 2020-08-12 – 2020-10-12. *PANGAEA*. DOI:
1866   http://dx.doi.org/10.1594/PANGAEA.926910

1867   Richter-Menge, JA, Perovich, DK, Elder, BC, Claffey, K, Rigor, I, Ortmeyer, M. 2006. Ice mass-
1868   balance buoys: a tool for measuring and attributing changes in the thickness of the Arctic
1869   sea-ice cover. *Annals of Glaciology* **44**: 205–210. DOI:
1870   http://dx.doi.org/10.3189/172756406781811727.

1871   Rigor, I, Ortmeyer, M. 2001. International Arctic Buoy Program 2001 Data Report, APL-UW TM
1872   6-02, Applied Physics Laboratory, University of Washington, 2002.
1873   https://iabp.apl.uw.edu/Data_Products/Reports/tm_6_02.pdf, last accessed on February
1874   2, 2024

1875   Rippeth, T, Fine, E. 2022. Turbulent mixing in a changing Arctic Ocean. *Oceanography* **35**(3–4):
1876   66–75. DOI: http://dx.doi.org/10.5670/oceanog.2022.103.

1877   Roberts, AF, Hunke, EC, Kamal, SM, Lipscomb, WH, Horvat, C, Maslowski, W. 2019. A variational
1878   method for sea ice ridging in Earth system models. *Journal of Advances in Modeling Earth*
1879   *Systems* **11**(3): 771–805. DOI: http://dx.doi.org/10.1029/2018MS001395.

1880 Rudels, B. 2009. Arctic Ocean Circulation. In: Steele, E-CJH, Turekian, KK, Thorpe, SA, editors.
1881 *Encyclopedia of Ocean Sciences (Second Edition).* Oxford: Academic Press. P. 211–225.
1882 DOI: http://dx.doi.org/10.1016/B978-012374473-9.00601-9.

1883 Salganik, E, Katlein, C, Lange, BA, Matero, I, Lei, R, Fong, AA, Fons, SW, Divine, D, Oggier, M,
1884 Castellani, G, Bozzato, D, Chamberlain, EJ, Hoppe, CJM, Müller, O, Gardner, J, Rinke,
1885 A, Simões Pereira, PS, Ulfsbo, A, Marsay, C, Webster, MA, Maus, S, Høyland, K,
1886 Granskog, MA. 2023. Temporal evolution of under-ice meltwater layers and false bottoms
1887 and their impact on summer Arctic sea ice mass balance. *Elementa: Science of the*
1888 *Anthropocene* **11**(1): 00035. DOI: http://dx.doi.org/10.1525/elementa.2022.00035.

1889 Schartmüller, B, Anderson, P, McKee, D, Connan-McGinty, S, Kopec, TP, Daase, M, Johnsen,
1890 G, Berge J. 2023. Development and calibration of a high dynamic range and autonomous
1891 ocean-light instrument to measure sub-surface profiles in ice-covered waters. *Applied*
1892 *Optics* **62**: 8308. DOI: http://dx.doi.org/10.1364/ao.502437.

1893 Schulz, K, Koenig, Z, Muilwijk, M, Bauch, D, Hoppe, CJM, Droste, E, Hoppmann, M, Chamberlain,
1894 EJ, Laukert, G, Stanton, T, Quintanilla Zurita, A, Fer, I, Heuzé, C, Karam, S, Mieruch-
1895 Schnuelle, S, Baumann, T, Vredenborg, M, Tippenhauer, S, Granskog, MA. n.d. The
1896 Eurasian Arctic Ocean along the MOSAiC drift (2019–2020): An interdisciplinary
1897 perspective on properties and processes. *Elementa: Science of the Anthropocene*
1898 (submitted). Preprint at DOI: http://dx.doi.org/10.31223/X5TT2W.

1899 Schulz, K, Mohrholz, V, Fer, I, Janout, M, Hoppmann, M, Schaffer, J, Koenig, Z. 2022. A full year
1900 of turbulence measurements from a drift campaign in the Arctic Ocean 2019–2020.
1901 *Scientific Data* **9**(1): 472. DOI: http://dx.doi.org/10.1038/s41597-022-01574-1.

1902 Sein, DV, Koldunov, NV, Danilov, S, Wang, Q, Sidorenko, D, Fast, I, Rackow, T, Cabos, W, Jung,
1903 T. 2017. Ocean modeling on a mesh with resolution following the local Rossby radius.
1904 *Journal of Advances in Modeling Earth Systems* **9**(7): 2601–2614. DOI:
1905 http://dx.doi.org/10.1002/2017MS001099.

1906 Shaw, WJ, Stanton, TP, McPhee, MG, Kikuchi, T. 2008. Estimates of surface roughness length
1907 in heterogeneous under-ice boundary layers. *Journal of Geophysical Research: Oceans*
1908 **113**(C8): C08030. DOI: http://dx.doi.org/10.1029/2007JC004550.

1909 Shaw, WJ, Stanton, TP, McPhee, MG, Morison, JH, Martinson, DG. 2009. Role of the upper
1910 ocean in the energy budget of Arctic sea ice during SHEBA. *Journal of Geophysical*
1911 *Research: Oceans* **114**(C6): C06012. DOI: http://dx.doi.org/10.1029/2008JC004991.

1912 Sherr, EB, Sherr, BF, Wheeler, PA, Thompson, K. 2003. Temporal and spatial variation in stocks
1913 of autotrophic and heterotrophic microbes in the upper water column of the central Arctic

Ocean. *Deep Sea Research Part I: Oceanographic Research Papers* **50**(5): 557–571. DOI: http://dx.doi.org/10.1016/S0967-0637(03)00031-1.

Shibley, NC, Timmermans, ML, Carpenter, JR, Toole, JM. 2017. Spatial variability of the Arctic Ocean's double-diffusive staircase. *Journal of Geophysical Research: Oceans* **122**(2): 980–994. DOI: http://dx.doi.org/10.1002/2016JC012419.

Shupe, MD, Rex, M, Blomquist, B, Persson, POG, Schmale, J, Uttal, T, Althausen, D, Angot, H, Archer, S, Bariteau, L, Beck, I, Bilberry, J, Bucci, S, Buck, C, Boyer, M, Brasseur, Z, Brooks, IM, Calmer, R, Cassano, J, Castro, V, Chu, D, Costa, D, Cox, CJ, Creamean, J, Crewell, S, Dahlke, S, Damm, E, de Boer, G, Deckelmann, H, Dethloff, K, Dütsch, M, Ebell, K, Ehrlich, A, Ellis, J, Engelmann, R, Fong, AA, Frey, MM, Gallagher, MR, Ganzeveld, L, Gradinger, R, Graeser, J, Greenamyer, V, Griesche, H, Griffiths, S, Hamilton, J, Heinemann, G, Helmig, D, Herber, A, Heuzé, C, Hofer, J, Houchens, T, Howard, D, Inoue, J, Jacobi, HW, Jaiser, R, Jokinen, T, Jourdan, O, Jozef, G, King, W, Kirchgaessner, A, Klingebiel, M, Krassovski, M, Krumpen, T, Lampert, A, Landing, W, Laurila, T, Lawrence, D, Lonardi, M, Loose, B, Lüpkes, C, Maahn, M, Macke, A, Maslowski, W, Marsay, C, Maturilli, M, Mech, M, Morris, S, Moser, M, Nicolaus, M, Ortega, P, Osborn, J, Pätzold, F, Perovich, DK, Petäjä, T, Pilz, C, Pirazzini, R, Posman, K, Powers, H, Pratt, KA, Preußer, A, Quéléver, L, Radenz, M, Rabe, B, Rinke, A, Sachs, T, Schulz, A, Siebert, H, Silva, T, Solomon, A, Sommerfeld, A, Spreen, G, Stephens, M, Stohl, A, Svensson, G, Uin, J, Viegas, J, Voigt, C, von der Gathen, P, Wehner, B, Welker, JM, Wendisch, M, Werner, M, Xie, ZQ, Yue, F. 2022. Overview of the MOSAiC expedition: Atmosphere. *Elementa: Science of the Anthropocene* **10**(1): 00060. DOI: http://dx.doi.org/10.1525/elementa.2021.00060.

Shupe, MD, Rex, M, Dethloff, K, Damm, E, Fong, AA, Gradinger, R, Heuzé, C, Loose, B, Makarov, A, Maslowski, W, Nicolaus, M, Perovich, D, Rabe, B, Rinke, A, Sokolov, V, Sommerfeld, A, 2020. The MOSAiC Expedition: A Year Drifting with the Arctic Sea Ice. *Series: Arctic Report Card*. DOI: http://dx.doi.org/10.25923/9G3V-XH92.

Sirevaag, A, De La Rosa, S, Fer, I, Nicolaus, M, Tjernström, M, McPhee, MG. 2011. Mixing, heat fluxes and heat content evolution of the Arctic Ocean mixed layer. *Ocean Science* **7**(3): 335–349. DOI: http://dx.doi.org/10.5194/os-7-335-2011.

Solomon, A, Shupe, MD, Svensson, G, Barton, NP, Batrak, Y, Bazile, E, Day, JJ, Doyle, JD, Frank, HP, Keeley, S, Remes, T, Tolstykh, M. 2023. The winter central Arctic surface energy budget: A model evaluation using observations from the MOSAiC campaign.

Elementa: Science of the Anthropocene **11**(1): 00104. DOI: http://dx.doi.org/10.1525/elementa.2022.00104.

Sperzel, TR, Jäkel, E, Pätzold, F, Lampert, A, Niehaus, H, Spreen, G, Rosenburg, S, Birnbaum, G, Neckel, N, Wendisch, M. 2023. Surface albedo measurements and surface type classification from helicopter-based observations during MOSAiC. *Scientific Data* **10**(1): 584. DOI: http://dx.doi.org/10.1038/s41597-023-02492-6.

Spreen, G, Kwok, R, Menemenlis, D, Nguyen, AT. 2017. Sea-ice deformation in a coupled ocean–sea-ice model and in satellite remote sensing data. *The Cryosphere* **11**(4): 1553–1573. DOI: http://dx.doi.org/10.5194/tc-11-1553-2017.

Stanton, TP, Shaw, WJ, Hutchings, JK. 2012. Observational study of relationships between incoming radiation, open water fraction, and ocean-to-ice heat flux in the Transpolar Drift: 2002–2010. *Journal of Geophysical Research: Oceans* **117**(C7). DOI: http://dx.doi.org/10.1029/2011JC007871.

Stanton, TP, Shaw, WJ. 2023a. Observations from Autonomous Ocean Flux Buoy 43 deployed at site L1 during the MOSAiC transpolar drift, Arctic Basin, 2019–2020. *NSF Arctic Data Center*. DOI: http://dx.doi.org/10.18739/A2610VT5W

Stanton, TP, Shaw, WJ. 2023b. Observations from Autonomous Ocean Flux Buoy 44 deployed at site L2 during the MOSAiC transpolar drift, Arctic Basin, 2019–2020. *NSF Arctic Data Center*. DOI: http://dx.doi.org/10.18739/A2P26Q527

Stanton, TP, Shaw, WJ. 2023c. Observations from Autonomous Ocean Flux Buoy 45 deployed at site L3 during the MOSAiC transpolar drift, Arctic Basin, 2019–2020. *NSF Arctic Data Center*. DOI: http://dx.doi.org/10.18739/A2XG9FC60

Stanton, TP, Shaw, WJ. 2023d. Observations from Autonomous Ocean Flux Buoy 46 deployed at site CO during the MOSAiC transpolar drift, Arctic Basin, 2019–2020. *NSF Arctic Data Center*. DOI: http://dx.doi.org/10.18739/A2SQ8QK2V

Steele, M, Morley, R, Ermold, W. 2001. PHC: A global ocean hydrography with a high-quality Arctic Ocean. *Journal of Climate* **14**(9): 2079–2087. DOI: http://dx.doi.org/10.1175/1520-0442(2001)014<2079:PAGOHW>2.0.CO;2.

Stefan, J. 1891. Ueber die Theorie der Eisbildung, insbesondere über die Eisbildung im Polarmeere. *Annalen der Physik* **278**: 269–286.

Stramler, K, Del Genio, AD, Rossow, WB. 2011. Synoptically driven Arctic winter states. *Journal of Climate* **24**(6): 1747–1762. DOI: http://dx.doi.org/10.1175/2010JCLI3817.1 .

1979   Strobach, E, Bel, G. 2017. The contribution of internal and model variabilities to the uncertainty in
1980   CMIP5 decadal climate predictions. *Climate Dynamics* **49**(9–10): 3221–3235. DOI:
1981   http://dx.doi.org/10.1007/s00382-016-3507-7.

1982   SWITCHYARD. 2023: http://psc.apl.washington.edu/switchyard/, last accessed June 30, 2023.

1983   Tao, R, Nicolaus, M, Katlein, C Anhaus, P Hoppmann, M Spreen, G Niehaus, H, Jäkel, E,
1984   Wendisch, M, Haas, C. n.D. Seasonality of spectral radiative fluxes and optical properties
1985   of Arctic sea ice. *Elementa: Science of the Anthropocene* (submitted).

1986   Timmermans, ML, Cole, S, Toole, J. 2012. Horizontal density structure and restratification of the
1987   Arctic Ocean surface layer. *Journal of Physical Oceanography* **42**(4): 659–668. DOI:
1988   http://dx.doi.org/10.1175/JPO-D-11-0125.1.

1989   Tjernström, M, Leck, C, Birch, CE, Bottenheim, JW, Brooks, BJ, Brooks, IM, Bäcklin, L, Chang,
1990   RYW, de Leeuw, G, Di Liberto, L, de la Rosa, S, Granath, E, Graus, M, Hansel, A,
1991   Heintzenberg, J, Held, A, Hind, A, Johnston, P, Knulst, J, Martin, M, Matrai, PA, Mauritsen,
1992   T, Müller, M, Norris, SJ, Orellana, MV, Orsini, DA, Paatero, J, Persson, POG, Gao, Q,
1993   Rauschenberg, C, Ristovski, Z, Sedlar, J, Shupe, MD, Sierau, B, Sirevaag, A, Sjogren, S,
1994   Stetzer, O, Swietlicki, E, Szczodrak, M, Vaattovaara, P, Wahlberg, N, Westberg, M,
1995   Wheeler, CR. 2014. The Arctic Summer Cloud Ocean Study (ASCOS): overview and
1996   experimental design. *Atmospheric Chemistry and Physics* **14**(6): 2823–2869. DOI:
1997   http://dx.doi.org/10.5194/acp-14-2823-2014.

1998   Toole, JM, Krishfield, R, Timmermans, ML, Proshutinsky, A. 2011. The Ice-Tethered Profiler: Argo
1999   of the Arctic. *Oceanography* **24**(3): 126–135. DOI:
2000   http://dx.doi.org/10.5670/oceanog.2011.64.

2001   Toole, JM, Krishfield, RA, O'Brien, JK, Houk, AE, Cole, ST, Woods Hole Oceanographic Institution
2002   Ice-Tethered Profiler Program. 2016. Ice-Tethered Profiler observations: Vertical profiles
2003   of temperature, salinity, oxygen, and ocean velocity from an Ice-Tethered Profiler buoy
2004   system. Dataset. *NOAA National Centers for Environmental Information*. Last accessed
2005   January 30, 2024. DOI: http://dx.doi.org/10.7289/V5MW2F7X.

2006   Toole, JM, Timmermans, ML, Perovich, DK, Krishfield, RA, Proshutinsky, A, Richter-Menge, JA.
2007   2010. Influences of the ocean surface mixed layer and thermohaline stratification on Arctic
2008   sea ice in the central Canada Basin. *Journal of Geophysical Research: Oceans* **115**(C10):
2009   2009JC005660. DOI: http://dx.doi.org/10.1029/2009JC005660.

2010   University of Washington. 2024: Measuring the Upper layer Temperature of the Polar Oceans.
2011   http://psc.apl.washington.edu/UpTempO/UpTempO.php, last accessed on February 7,
2012   2024.

2013 Untersteiner, N, Thorndike, AS, Rothrock, DA, Hunkins, KL. 2009. AIDJEX revisited: A look back
2014   at the U.S.-Canadian Arctic Ice Dynamics Joint Experiment 1970–78. *Arctic* **60**(3): 327–
2015   336. DOI: http://dx.doi.org/10.14430/arctic233.

2016 von Albedyll, L, Hendricks, S, Grodofzig, R, Krumpen, T, Arndt, S, Belter, HJ, Birnbaum, G,
2017   Cheng, B, Hoppmann, M, Hutchings, JK, Itkin, P, Lei, R, Nicolaus, M, Ricker, R, Rohde,
2018   J, Suhrhoff, M, Timofeeva, A, Watkins, D, Webster, M, Haas, C. 2022. Thermodynamic
2019   and dynamic contributions to seasonal Arctic sea ice thickness distributions from airborne
2020   observations. *Elementa: Science of the Anthropocene* **10**(1): 00074. DOI:
2021   http://dx.doi.org/10.1525/elementa.2021.00074.

2022 von Appen, WJ, Baumann, T, Janout, M, Koldunov, N, Lenn, YD, Pickart, R, Scott, R, Wang, Q.
2023   2022. Eddies and the distribution of eddy kinetic energy in the Arctic Ocean.
2024   *Oceanography* **35**(3–4): 42–51. DOI: http://dx.doi.org/10.5670/oceanog.2022.122.

2025 Wang, Q, Koldunov, NV, Danilov, S, Sidorenko, D, Wekerle, C, Scholz, P, Bashmachnikov, IL,
2026   Jung, T. 2020. Eddy kinetic energy in the Arctic Ocean from a global simulation with a 1-
2027   km Arctic. *Geophysical Research Letters* **47**(14). DOI:
2028   http://dx.doi.org/10.1029/2020GL088550.

2029 Watkins, DM. 2023b. Relative motion of the buoys in the MOSAiC Distributed Network from 2019-
2030   12-20 to 2020-01-19. *Zenodo*. DOI: http://dx.doi.org/10.5281/ZENODO.10278327.

2031 Watkins, DN, Persson, OPG, Hutchings, JK, Stanton, TP, Solomons, A. 2023c. Sea Ice and
2032   Ocean Response to a Strong Mid-Winter Cyclone in the Arctic Ocean. Abstract C41C-
2033   1534 presented at *AGU23*, San Francisco, CA, December 11–15, 2023.
2034   DOI: http://dx.doi.org/10.22541/essoar.170365235.53452562/v1.

2035 Watkins, DM, Bliss, AC, Hutchings, JK, Wilhelmus, MM. 2023a. Evidence of abrupt transitions
2036   between sea ice dynamical regimes in the East Greenland marginal ice zone. *Geophysical*
2037   *Research Letters* **50**: 2023GL103558. DOI: http://dx.doi.org/10.1029/2023GL103558.

2038 Webster, MA, Holland, M, Wright, NC, Hendricks, S, Hutter, N, Itkin, P, Light, B, Linhardt, F,
2039   Perovich, DK, Raphael, IA, Smith, MM, von Albedyll, L, Zhang, J. 2022. Spatiotemporal
2040   evolution of melt ponds on Arctic sea ice. *Elementa: Science of the Anthropocene* **10**(1):
2041   000072. DOI: http://dx.doi.org/10.1525/elementa.2021.000072.

2042 Wedi, NP, Polichtchouk, I, Dueben, P, Anantharaj, VG, Bauer, P, Boussetta, S, Browne, P,
2043   Deconinck, W, Gaudin, W, Hadade, I, Hatfield, S, Iffrig, O, Lopez, P, Maciel, P, Mueller,
2044   A, Saarinen, S, Sandu, I, Quintino, T, Vitart, F. 2020. A baseline for global weather and
2045   climate simulations at 1 km resolution. *Journal of Advances in Modeling Earth Systems*
2046   **12**(11). DOI: http://dx.doi.org/10.1029/2020MS002192.

2047 Weingartner, T, Ashjian, C, Brigham, L, Haine, T, Mack, L, Perovich, D, Rabe, B. 2022.
2048   Introduction to the Special Issue on the New Arctic Ocean. *Oceanography* **35**(3–4): 6–9.
2049   DOI: http://dx.doi.org/10.5670/oceanog.2022.132
2050 Wu, B, Handorf, D, Dethloff, K, Rinke, A, Hu, A. 2013. Winter weather patterns over Northern
2051   Eurasia and Arctic sea ice loss. *Monthly Weather Review* **141**(11): 3786–3800. DOI:
2052   http://dx.doi.org/10.1175/MWR-D-13-00046.1.

2053

2054

2055

Figures and full captions
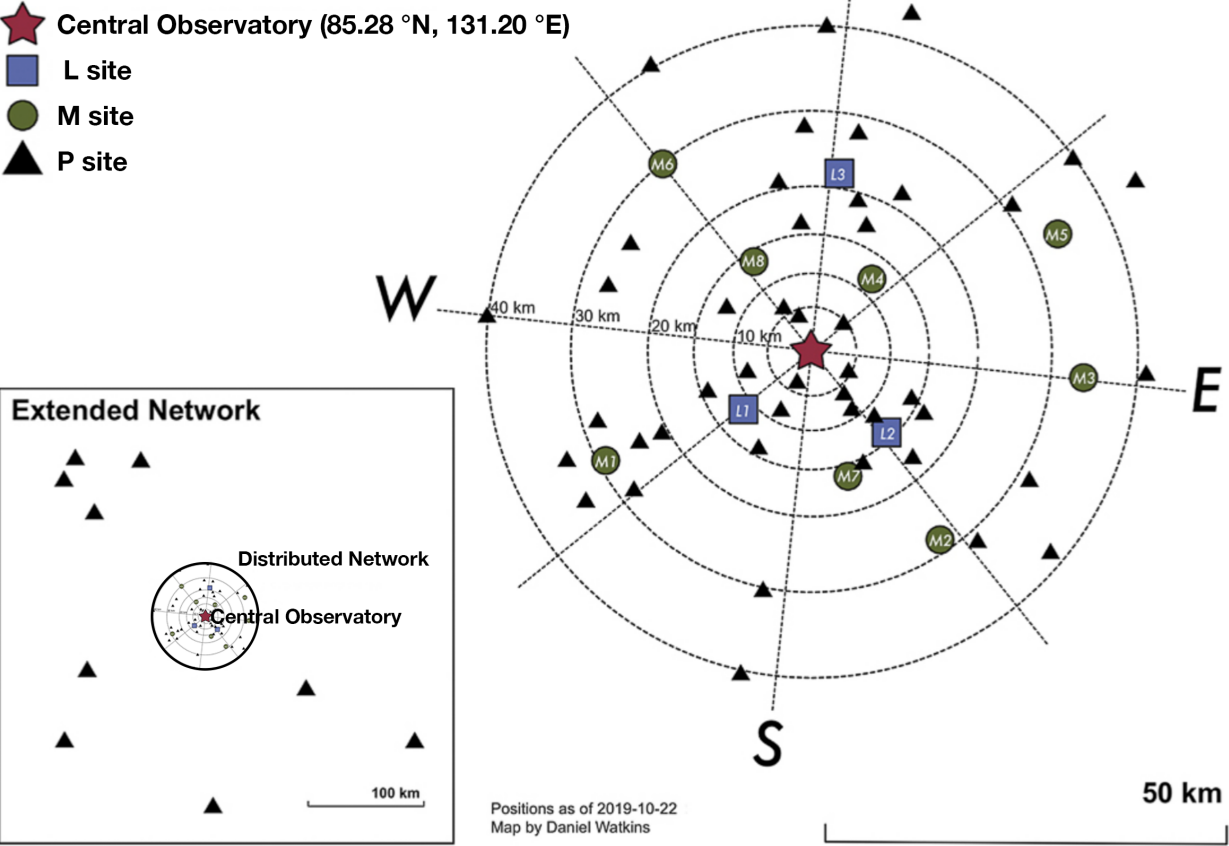
2059 **Figure 1. Actual layout of the Distributed Network after completing all initial deployments**
2060 **on October 22, 2019.**
2061 The different site types are distinguished by color as shown in the legend: L sites (blue squares),
2062 M sites (green circles) and P sites (black triangles). The Central Observatory with RV *Polarstern*
2063 is located in the center of the map (red star). Note that the LM site (not shown) was part of the
2064 wider Central Observatory, located 1–2 km away from RV *Polarstern*. The figure is modified from
2065 Krumpen and Sokolov (2020, their Figure 1.2).
2066

2067

Figure 2. Photographs of selected autonomous platforms (buoys) deployed in the two implementations of the Distributed Network.

a) Atmospheric Surface Flux Station (ASFS #50 at L3 (photo by Ola Persson); b) radiation station 2020R21 and thermistor string buoy 2020T81 deployed on a frozen melt pond (RITBOB; photo by Mario Hoppmann); c) Snow Buoy 2020S109 (Snow Buoy; photo by Mario Hoppmann); d) Unmanned (uncrewed) Ice Station (UMIS; photo by unknown); e) Seasonal Ice Mass Balance buoy (SIMB3; photo by unknown); f) Snow Ice Mass Balance Apparatus (SIMBA; photo by Mario

2075 Hoppmann); g) Acoustic Zooplankton and Fish Profiler (AZFP) buoy and bio-optical buoy
2076 2020M23 (IMBflex), with ablation stakes in the background (photo by Mario Hoppmann); h) First
2077 Institute of Oceanography Fixed-Level Ocean buoy (FIO FLB; photo by Bing Kong); i) Drift-Towing
2078 Ocean Profiler (D-TOP; photo by Mario Hoppmann); j) Woods-Hole Ice-Tethered Profiler (WHOI
2079 ITP; photo by unknown); k) position-tracking buoy 2020P162 (ice tracker; photo by Marcel
2080 Nicolaus); l) Salinity Ice Tether buoy (SIT; photo by Mario Hoppmann); m) Autonomous Ocean
2081 Flux Buoy (AOFB; photo by Michael Gallagher); n) light strings (OptiCAL, formerly Envipope;
2082 photo by Dmitry Divine); o) ice-Surface Velocity Profiler 2020P237 (iSVP; photo by Mario
2083 Hoppmann). Details of the different platform types are summarized in Tables 1 and S1.

2084

Figure 3. Photographs of conditions during recovery of the Distributed Network platforms in 2020.

a) Atmospheric Surface Flux Station #50 turned upside down after ridging event at site L3 on February 4, requiring maintenance and reinstallation at the Central Observatory (photo by Michael Gallagher); b) surface unit and floatation of Woods Hole Ice-tethered Profiler #102 (2019W3) at site L3 during recovery in August: the tether had been severed so that the corresponding profiler could not be recovered as the tether had been severed (photo by Julia Regnery); c) Snow Buoy during recovery by "mummy chair" from the ship (photo by Julia Regnery).

2093

2094
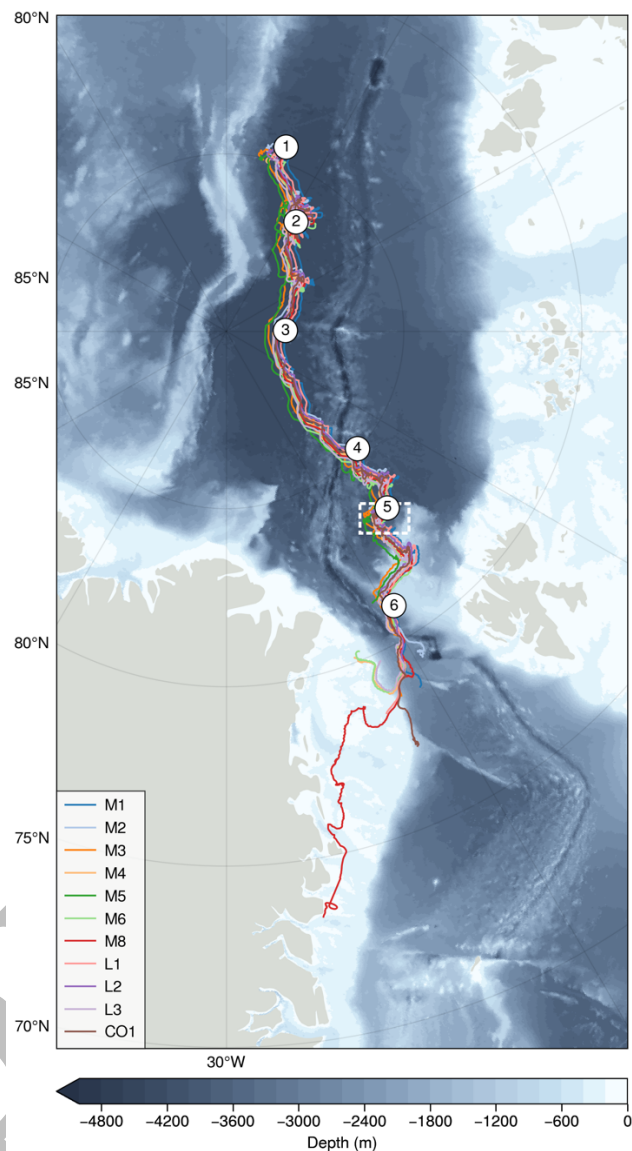
Figure 4. Drift tracks of the main sites of the Distributed Network.

Tracks of the 3 L sites and 8 M sites and the Central Observatory (CO1). Table S3 lists all data sources and their properties used to create the drift tracks, with further explanation given in Text S3. Drift track data are available from Nicolaus et al. (2021b). Note that the LM site (not shown) was part of the wider Central Observatory and very close to RV *Polarstern*, within 1–2 km when the ship was present. The numbers 1 to 6 on the track refer to the location of the maps in Figure 5, with Figure 1 located close to number 1. That part of the drift track where RV *Polarstern* was absent from the Central Observatory is marked by the white, dashed box, between about 82.4°N and 83.4°N. The seafloor topography and coastlines are based on the General Bathymetric Chart of the Oceans (GEBCO, 2020).
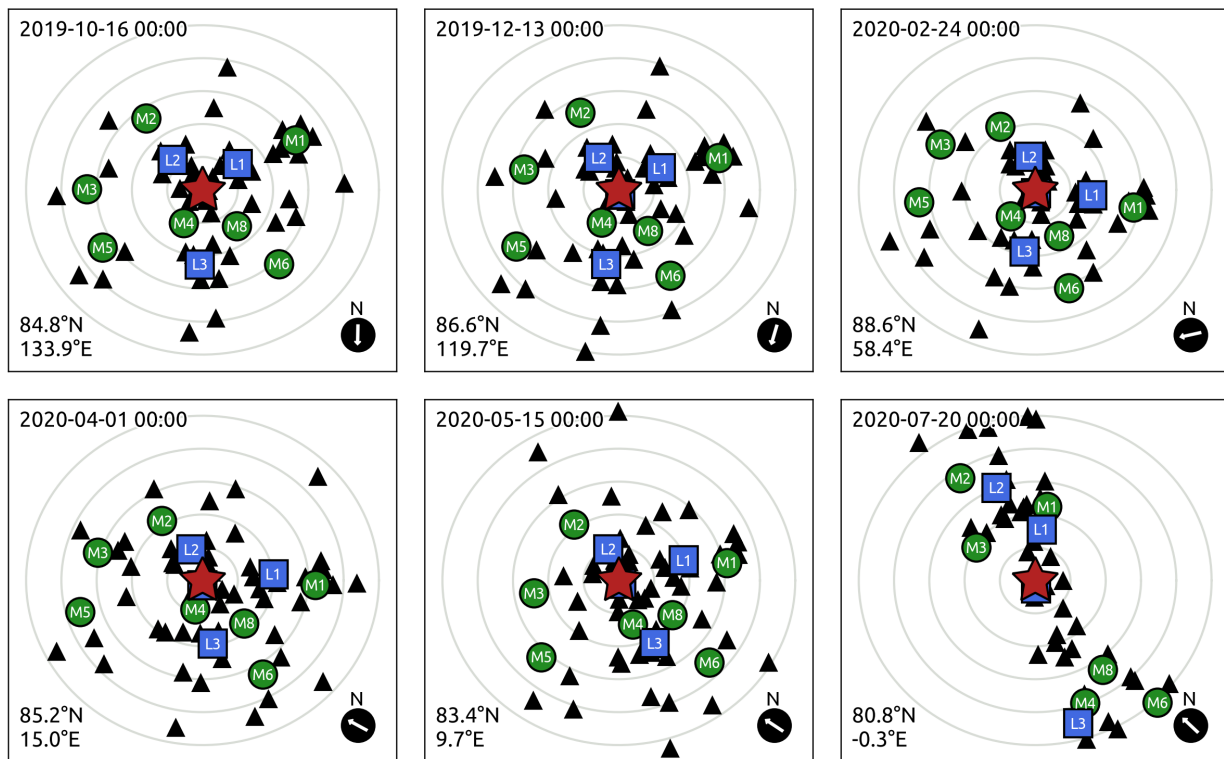
Figure 5. Evolution of the Distributed Network from mid-October 2019 to late July 2020.
Position of the Distributed Network sites at six times during the drift in the transpolar drift, as marked in Figure 4. This set of maps documents the array after deployment, in late spring and towards the end of the drift as the array approached Fram Strait. Positions are shown in north polar stereographic projection; arrows in the lower right corners of each panel point north, and the position of the Central Observatory is shown in latitude/longitude in the lower left corner. Gray circles are plotted at 10 km intervals from the Central Observatory. The symbols refer to the Central Observatory, including the site LM (red star), the M sites (blue squares), the L sites (green circles) and the P sites (black triangles; see also Figure 1).

72

2117
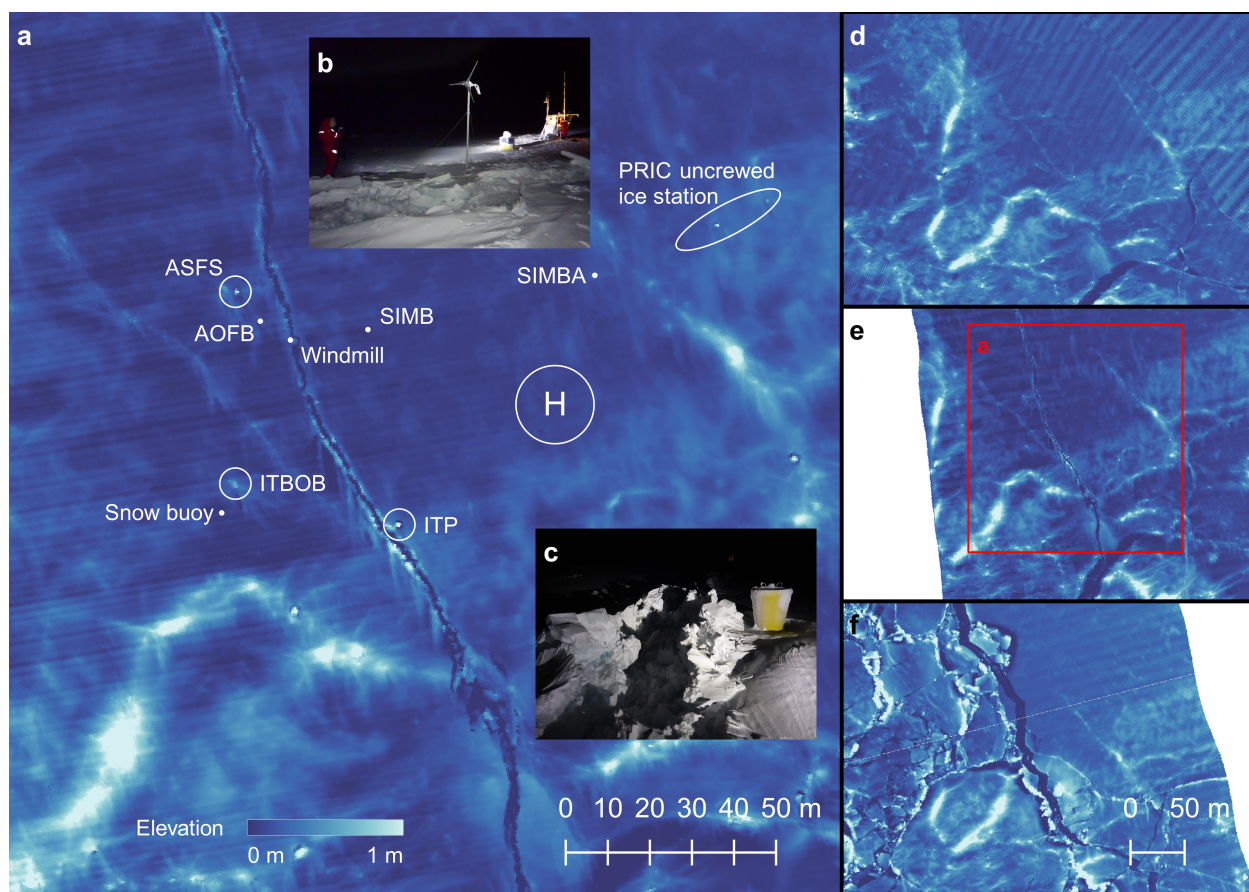
Figure 6. Surface elevation maps of site L3 in mid-winter from airborne laser scanner observations.

Shades of blue denote the approximate surface elevation according to the color bar, where the lightest blue indicates heights of 1 m and above. The large map in panel a shows the situation on January 25, 2020, where buoy locations are labeled. The combined radiation station and ice mass balance buoy (IMB) is labelled "ITBOB". "H" marks the usual landing site for the helicopter. Photos b and c taken on January 20 show selected buoys and the developing crack in the ice (photos by Eric Brossier). The evolution throughout about one month is shown in panels d–f without annotations: d) January 8, e) January 25 and f) February 9. The red square in panel e shows the extent of panel a. The large crack from bottom right to top left is visible as a ragged dark-blue line after January 25. The Autonomous Ocean Flux Buoy (AOFB), Atmospheric Surface Flux Station (ASFS) and Woods Hole Ice-tethered Profiler (ITP) were subsequently damaged or disappeared as the crack developed into a pressure ridge (see also Figure 3a). Note the different horizontal scales in panel a and in panels d–f. The maps are based on data in Hutter et al. (2023a) and processed according to Hutter et al. (2023b).
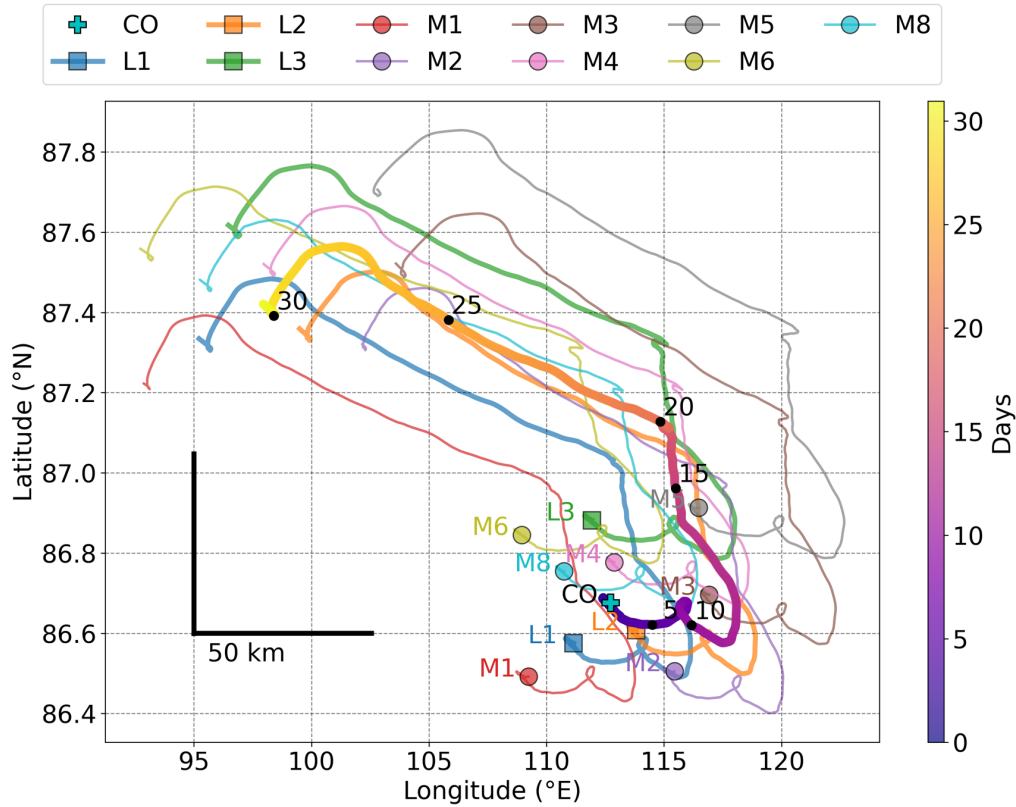
73

2133

Figure 7. Geographic position of sites within the Distributed Network from late December to late January.

The black lines show the scale of horizontal distance in kilometers. The legend denotes the different sites with symbols corresponding to the position on December 20, 2019, and color to the lines of each site. Note that the P site tracks are omitted for clarity. CO is the position of the Central Observatory with RV *Polarstern*, with the 30-day time period shown in days from 20 December, 2019 (both in color and labelled every 5 days). The data for the M sites are from Salinity Ice Tether buoys (Hoppmann et al., 2022b).

2142
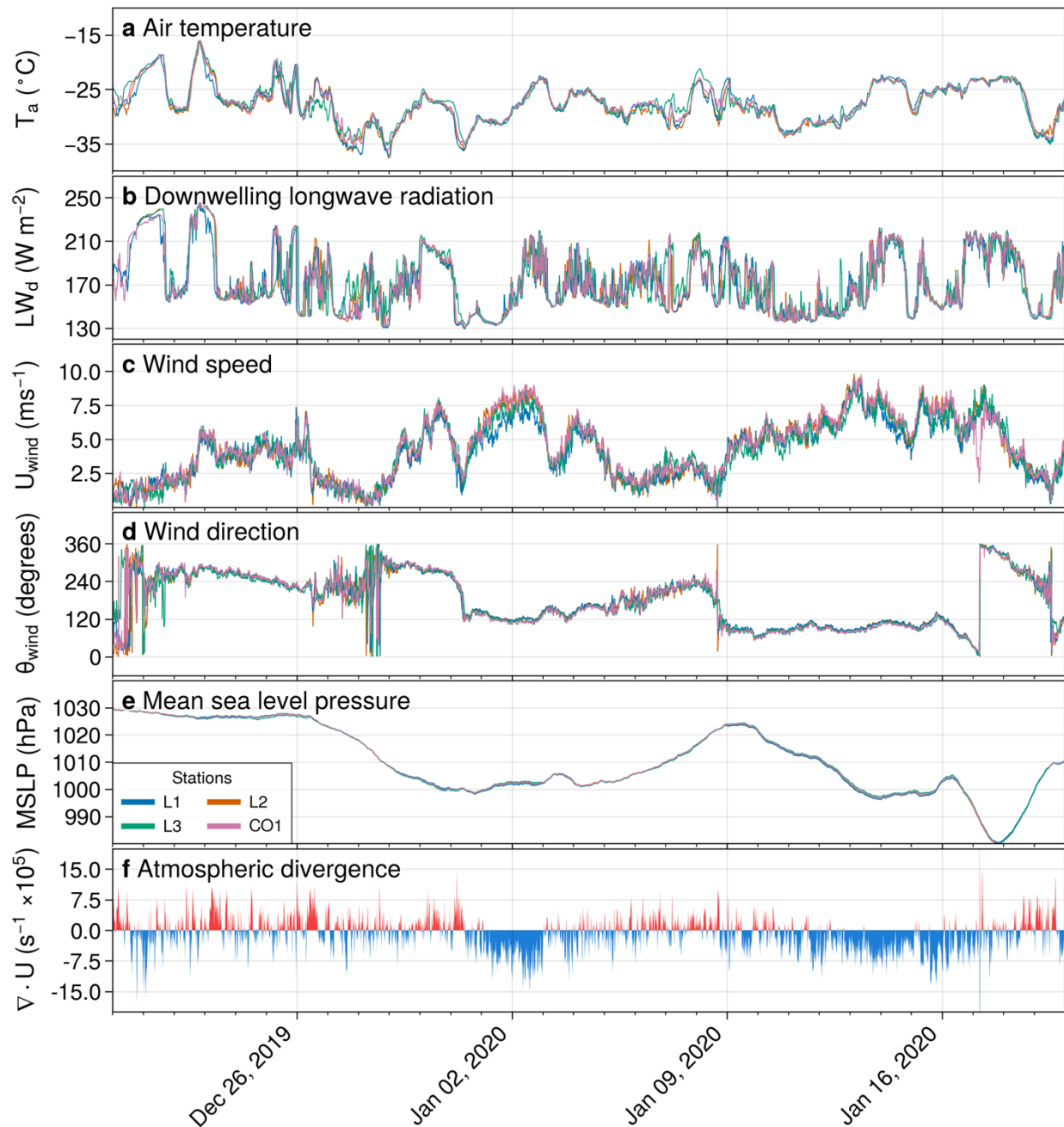
Figure 8. Time series of 10-minute means for meteorological measurements from late December to late January.

Observations from the meteorological installation at the Central Observatory (CO1 in the figure) and the three Atmospheric Surface Flux Stations at the L sites (L1–L3) during December 20, 2019–January 19, 2020: a) near-surface air temperature (T_a), b) downwelling longwave radiation (LW_d), c) wind speed (U_{wind}), d) wind direction (θ_{wind}; meteorological definition, opposite to the direction of motion), e) mean sea-level pressure (MSLP), and f) wind divergence across the L1–

75

2151   L3 triangle ($\nabla \cdot U$; anomaly to the mean of the full time series). Note that the wind measurements

2152   at L1–L3 (Atmospheric Surface Flux Stations) were obtained at 3.8 m above the ice surface, and

2153 T_a at 2 m. Those at CO1 were obtained at approximately 6 m. The observational data can be

2154   found in Cox et al. (2023b 2023c; 2023d; 2023e).
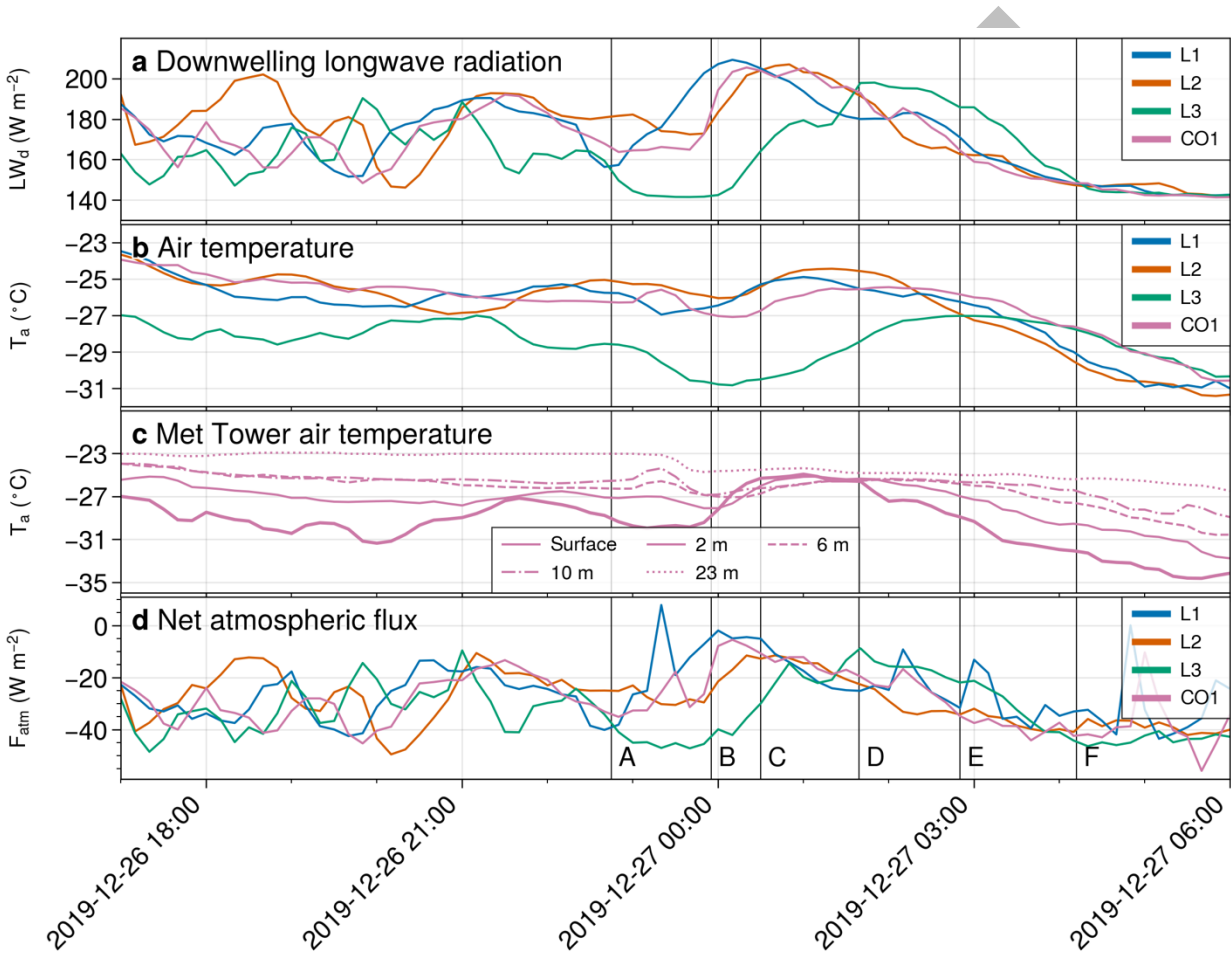
2155

2156
2157 **Figure 9. Time series of atmospheric variables between 17:00 December 26 and 06:00**

2158 **December 27 in 2019.**

2159   a) Downwelling longwave radiation at the three L sites (L1–L3) and the meteorological installation

2160   at the Central Observatory (CO1), b) near-surface air temperature at the L sites (2 m height) and

2161   at CO1 (6 m height), c) air temperature at the different heights at CO1, and d) the net atmospheric

2162   energy flux (F_{atm}) at the three L sites and CO1. The six vertical lines labeled a–f show the times

2163   of the KaSACR reflectivity panels in Figure S4. The observational data are a subset of those
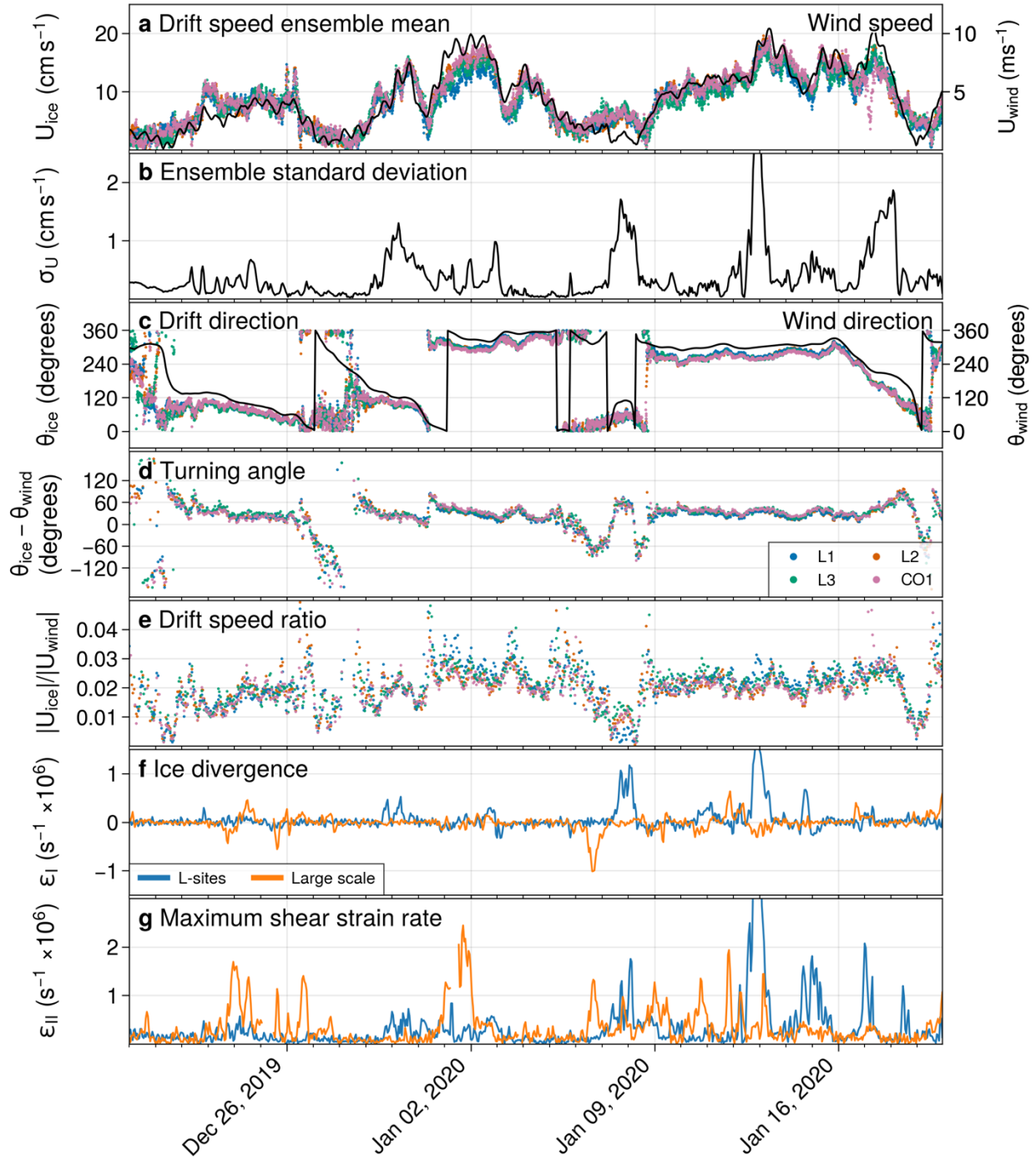
2164   shown in Figure 8.

2165

Figure 10. Time series of ice drift and deformation from late December to late January.
Observations from the period December 19, 2019–January 19, 2020, for: a) wind speed at the L sites (L1–L3) and the Central Observatory (CO1; colored dots) and ensemble mean (black line) of ice drift speed of position-tracking buoys within the Distributed Network (DN; black line); b) standard deviation of the ensemble ice drift speed; c) ensemble mean drift direction and wind direction (positive in the direction of motion) of the time series in a; d) the difference between the

77

2173   ice drift direction and the wind direction at the L sites and CO1 (turning angle); e) the ratio between

2174   the ice drift speed and the local wind speed at the L sites and CO1; f) the deformation calculated

2175   (following Hutchings et al., 2012; 2018) from buoys on the perimeter of the DN, where orange

2176   represents the large scale and blue shows the deformation of the L site triangle, which is a smaller

2177   scale; and (g) maximum shear strain rate for the same set of buoys as in panel f. Data from the

2178   L1–L3 sites and CO1 are shown in panels a–e as denoted by color in the legend. For panels a

2179   and c, only points where the wind speed was >1 m s^{-1} and drift speed >0.01 m s^{-1} are used. The

2180   data can be found under Bliss et al. (2022).
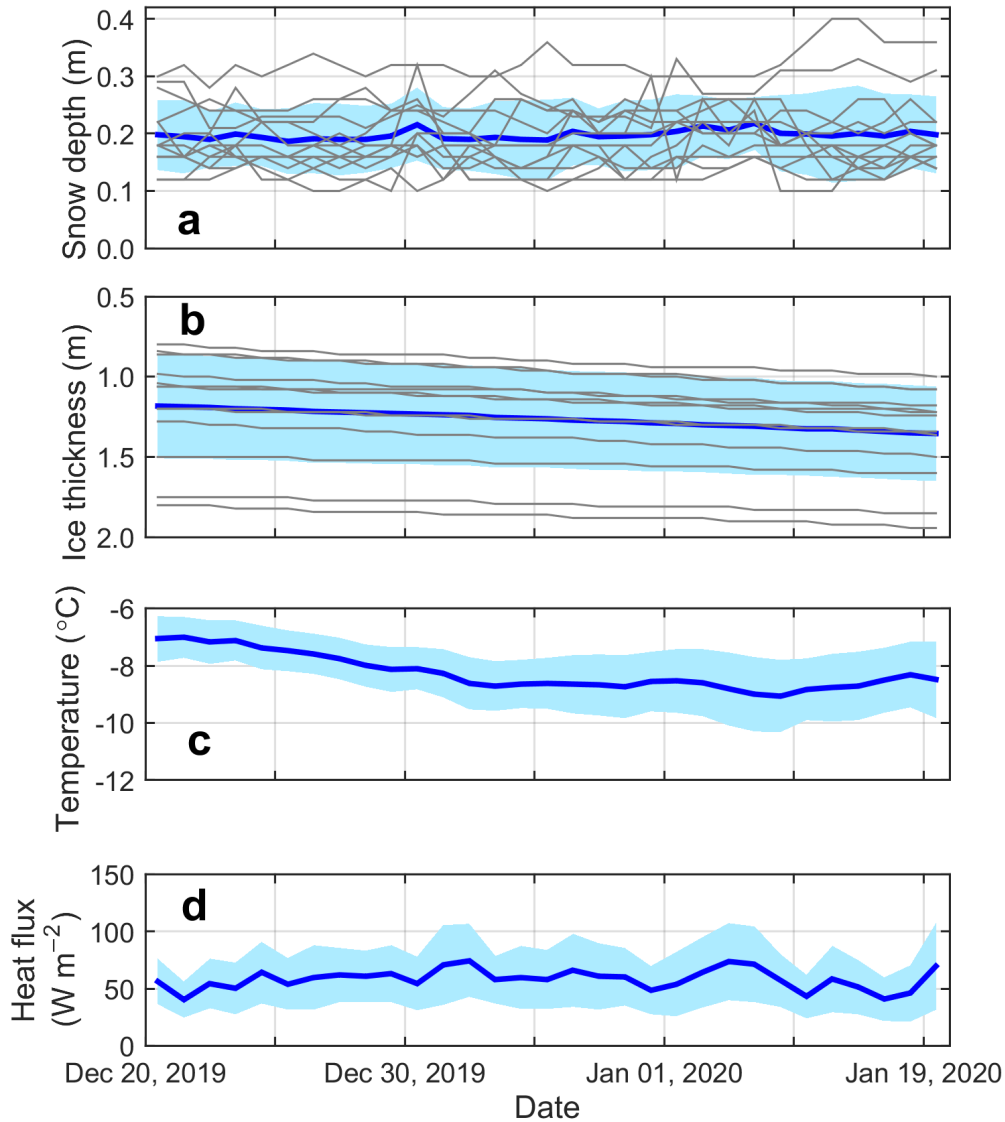
2181

Figure 11. Snow and sea ice mass balance data from late December to late January.
Observations of a) snow depth, b) ice thickness, c) bulk-average temperature through the ice
layer, and d) conductive heat flux through the top ice layer during December 20, 2019–January
19, 2020, obtained from the measurements by 13 ice mass balance buoys (SIMBA; Table 1)
deployed over the MOSAiC Distributed Network. The thick blue line and cyan shade are the
average and standard deviation obtained from 13 measurement sites; the thin grey lines shown
in panels a and b are the data obtained from each buoy. The data can be found under Lei et al.
(2021b; 2021c; 2021d; 2022b; 2022c; 2022d; 2022e; 2022f; 2022g; 2022h; 2022I; 2022j;
2022k).
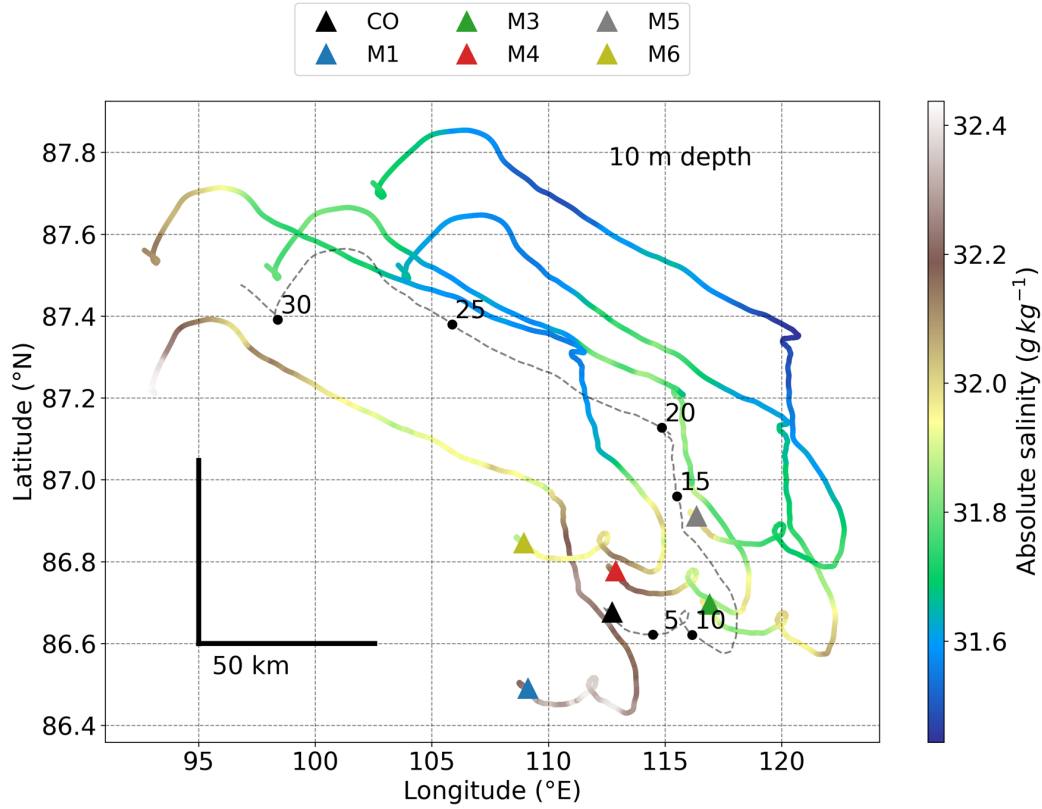
Figure 12. Horizontal distribution of absolute salinity at 10 m depth from late December to late January.
The initial positions of the buoys (denoted by site name in the legend) are denoted by colored triangles, and the track of the Central Observatory (CO) is denoted by the black dashed line. The numbers on the Central Observatory (CO) track are days from December 20, 2019. Absolute salinity is given in g kg^{-1} as defined by TEOS10 (see McDougall et al., 2010; McDougall and Barker, 2011). The data are from Salinity Ice Tether buoys (Hoppmann et al., 2022b).
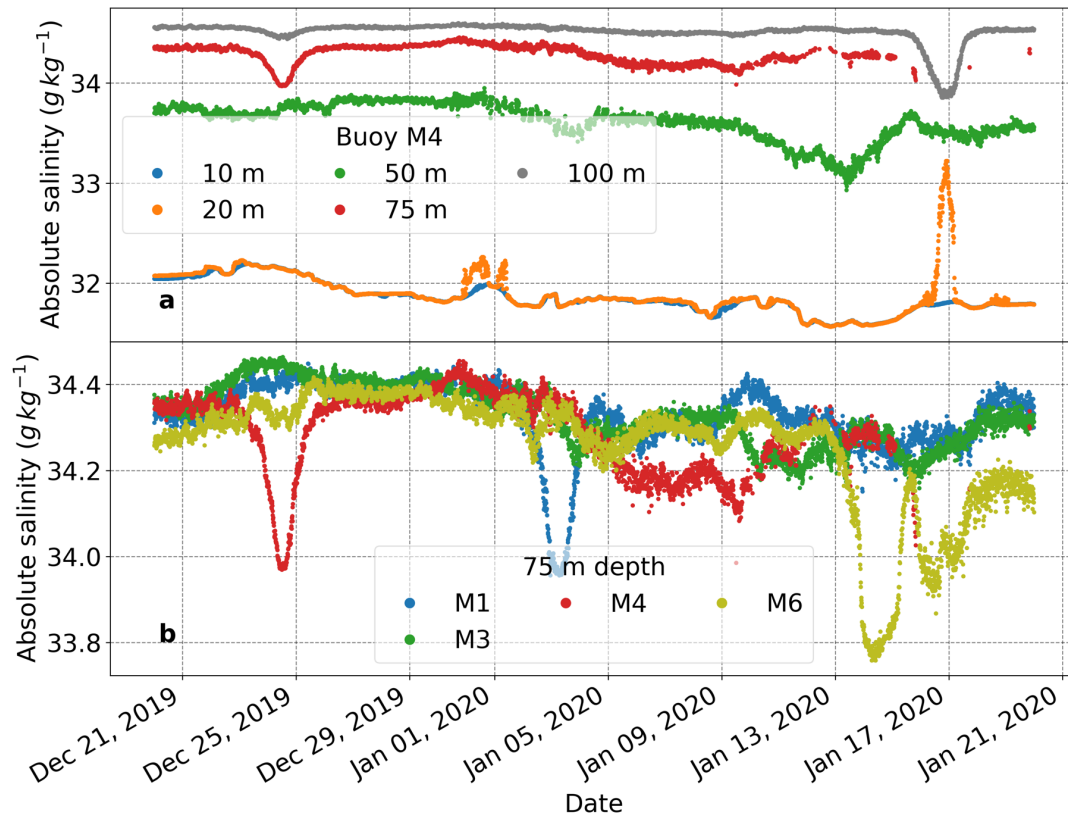
2203

Figure 13. Absolute salinity at discrete depths across the Distributed Network from late December to late January.

The observations by different buoys with instruments at the depths shown are based on 10-minute measurement intervals. The depths (upper panel) and the sites (lower panel) are denoted by color, as shown in the legend. The data are from Salinity Ice Tether buoys (Hoppmann et al., 2022b).

2210
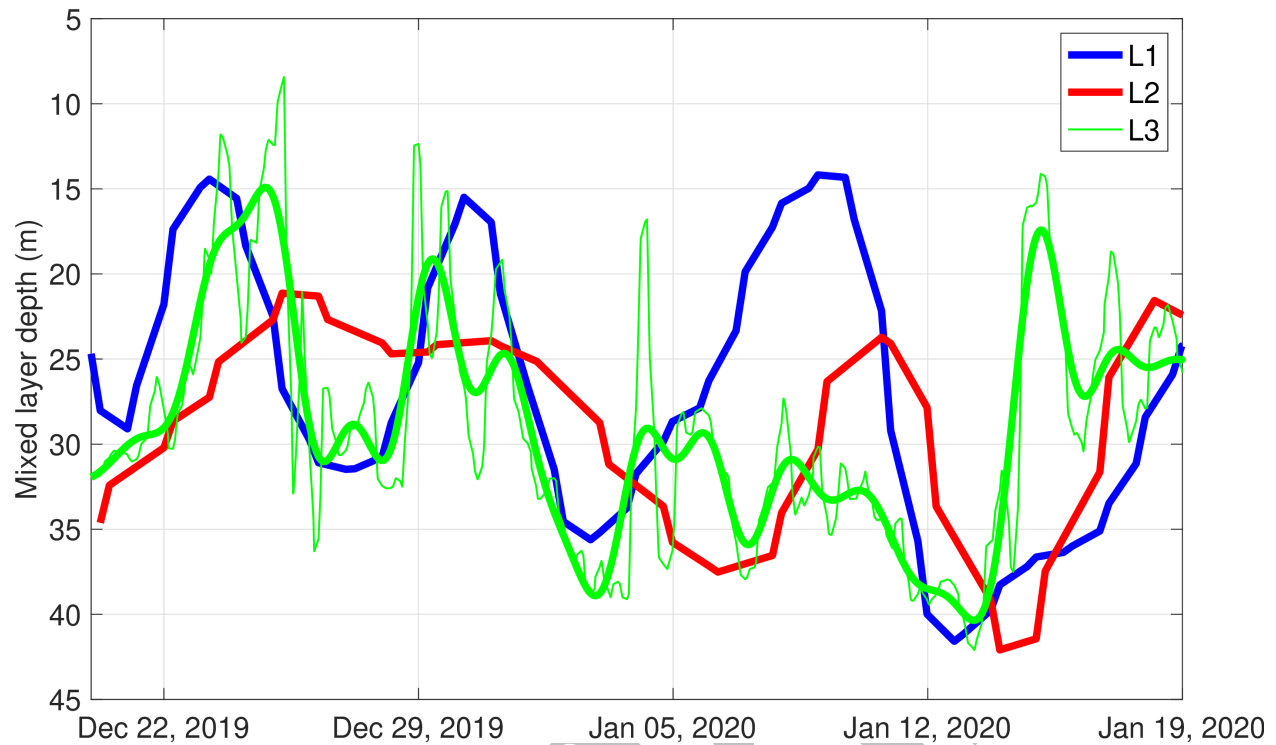
Figure 14. Time series of mixed layer depth at sites L1–3 from late December to early January.

The values are derived from conservative temperature and absolute salinity profiles (after TEOS10; see Figure 12) measured by the Woods Hole Ice-tethered Profiler at each L site, as denoted in the inset legend. The criterion for mixed layer depth assumes a density-step of 0.05 kg m^{-3} in accordance with Rabe et al. (2022), based on Toole et al. (2010). Note that the Woods Hole Ice-tethered Profiler at L1 and L2 only measured two profiles a day, whereas the one at L3 obtained profiles 8 times per day. Note that both the original values at L3 (thin line) and the 12-hour low-pass filtered values (5th order Butterworth filter; thick line) are shown. The Woods Hole Ice-tethered Profiler profile data can be found under Toole et al. (2016).
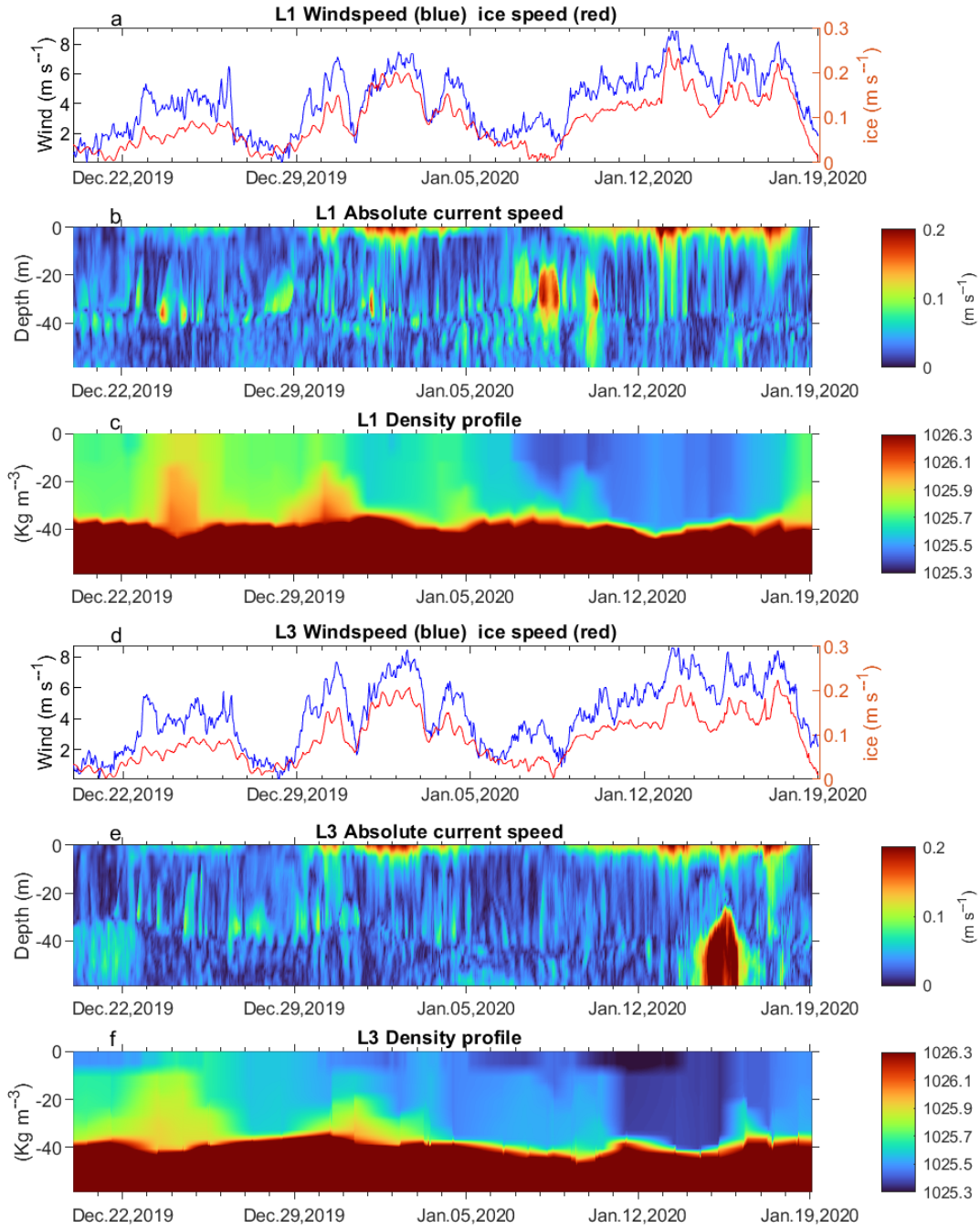
Figure 15. Wind, ice and ocean speed, and ocean density, from late December to late January .

83

2226 Comparative observations at site L1 (a–c) and site L3 (d–f) of 1.8-m height wind forcing and ice

2227 speed (a, d), absolute current profiles with 15-minute averaging (b, e), and potential density,

2228 relative to 0 dbar (c, f). At each site the wind speed was measured by the adjacent Atmospheric

2229 Surface Flux Station, currents were derived from the acoustic doppler current profilers in the

2230 Autonomous Ocean Flux Buoys (AOFBs), and ice speed from the AOFB geographic position,

2231 while ocean density is based on observations by the co-located Woods Hole Ice-tethered

2232 Profiler (WHOI-ITP) CTD. The WHOI-ITP data can be found under Toole et al. (2016); the

2233 Atmospheric Surface Flux Station data are from Cox et al. (2023d; 2023e); the AOFB data are

2234 from Stanton and Shaw (2023a; 2023b; 2023c; 2023d).
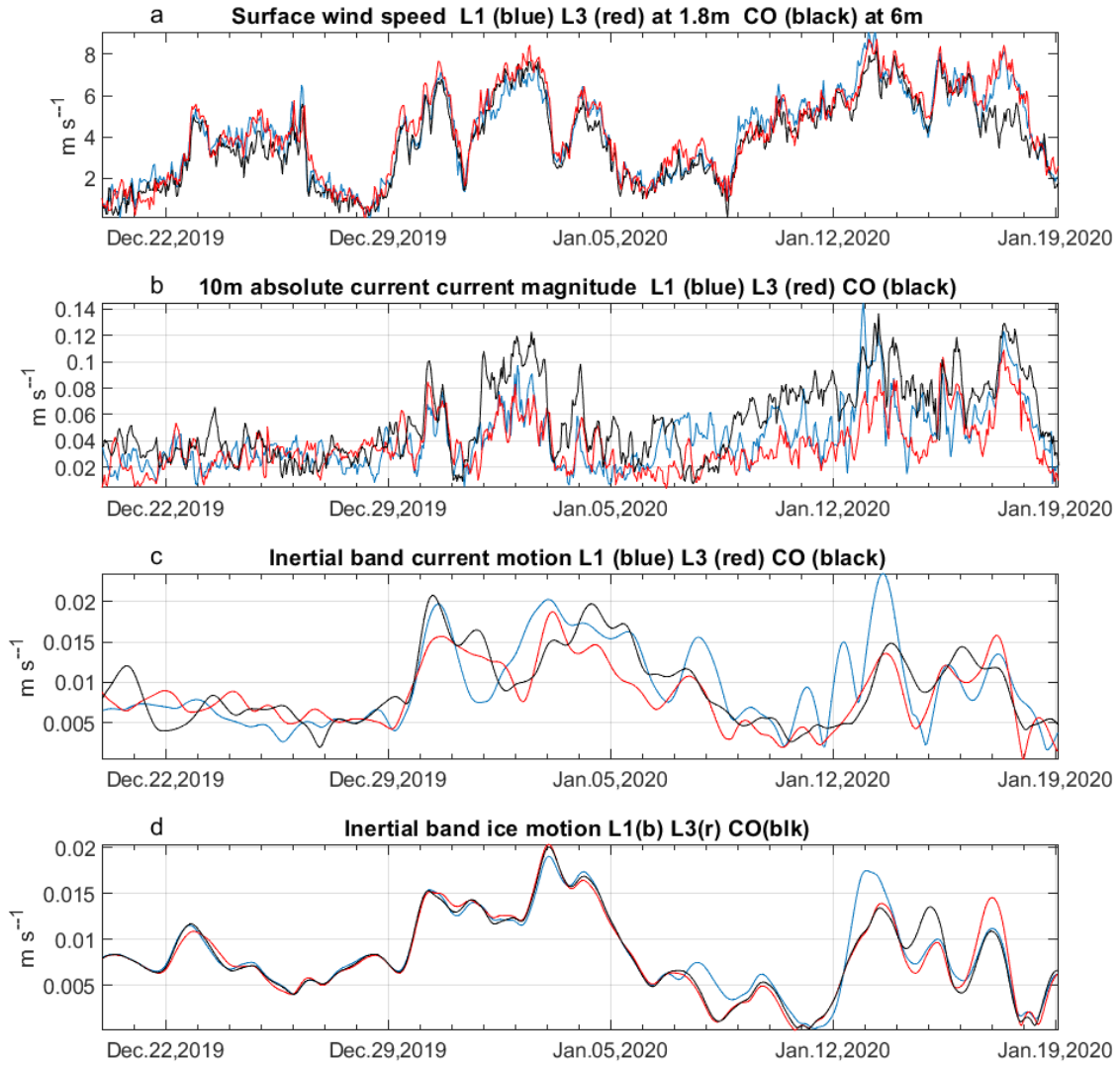
2235

a Surface wind speed L1 (blue) L3 (red) at 1.8m CO (black) at 6m

b 10m absolute current current magnitude L1 (blue) L3 (red) CO (black)

c Inertial band current motion L1 (blue) L3 (red) CO (black)

d Inertial band ice motion L1(b) L3(r) CO(blk)

2236
2237 **Figure 16. Wind speed, upper ocean currents and ice inertial band motion, late December**
2238 **to late January.**

2239 a) Observations of surface wind speed at sites L1, L3 and the Central Observatory (CO); b)
2240 corresponding 10 m depth absolute ocean current magnitudes; c) 0.3 f 6th order bandpass filtered
2241 10 m depth inertial currents; and d) ice inertial band motion from Autonomous Ocean Flux Buoy
2242 (AOFB) position with the same filter used in panel c. The Coriolis parameter is $f = 2\omega \sin(\phi)$,
2243 where ϕ is the latitude and $\omega = 7.2921\ 10^{-5}\ \frac{rad}{s}$. The data in panel a are from Cox et al. (2023b;
2244 2023d; 2023e); in panels b, c and d the AOFB data are from Stanton and Shaw (2023a; 2023b;
2245 2023c; 2023d).

85

2248 **Figure 17. Late-spring snow and sea ice mass balance and conductive heat flux at the ice**

2249 **surface.**

2250 Changes in snow depth, ice thickness, and temperature at a) site L1, b) site L2, and c) site L3

2251 May 16–June 18, 2020, with thick black line denoting snow or ice (after snow melted over) surface,

2252 grey dashed line denoting initial snow-ice interface, and thick black line denoting ice bottom. d)

2253 Average (thick blue line) and standard deviation (shade) of daily conductive heat flux at the
2254 surface of the ice layer calculated from continuous measurements by 8 buoys at 5 sites (L1, L3,
2255 M3, M6, 1 buoy each; Central Observatory, 4 buoys). Also shown is the daily near-surface (2 m
2256 height) air temperature measured by the Unmanned (uncrewed) Ice Station at the site L3. These
2257 measurements agree approximately with measurements at 2 m height by Atmospheric Surface
2258 Flux Station #30 at the Central Observatory and can be expected to be representative of the
2259 region around the L sites, as spatial variability within the three Distributed Network sites with
2260 Atmospheric Surface Flux Stations installed was low for time scales greater than approximately
2261 1 day (not shown). Data for panel a can be found under Lei et al. (2022c); for panel b, under Lei
2262 et al. (2022i); for panel c, under Lei et al. (2022k); and for panel d, under Lei et al. (2021b; 2022b;
2263 2022c; 2022d; 2022g; 2022k; 2022l; 2022m).
2264
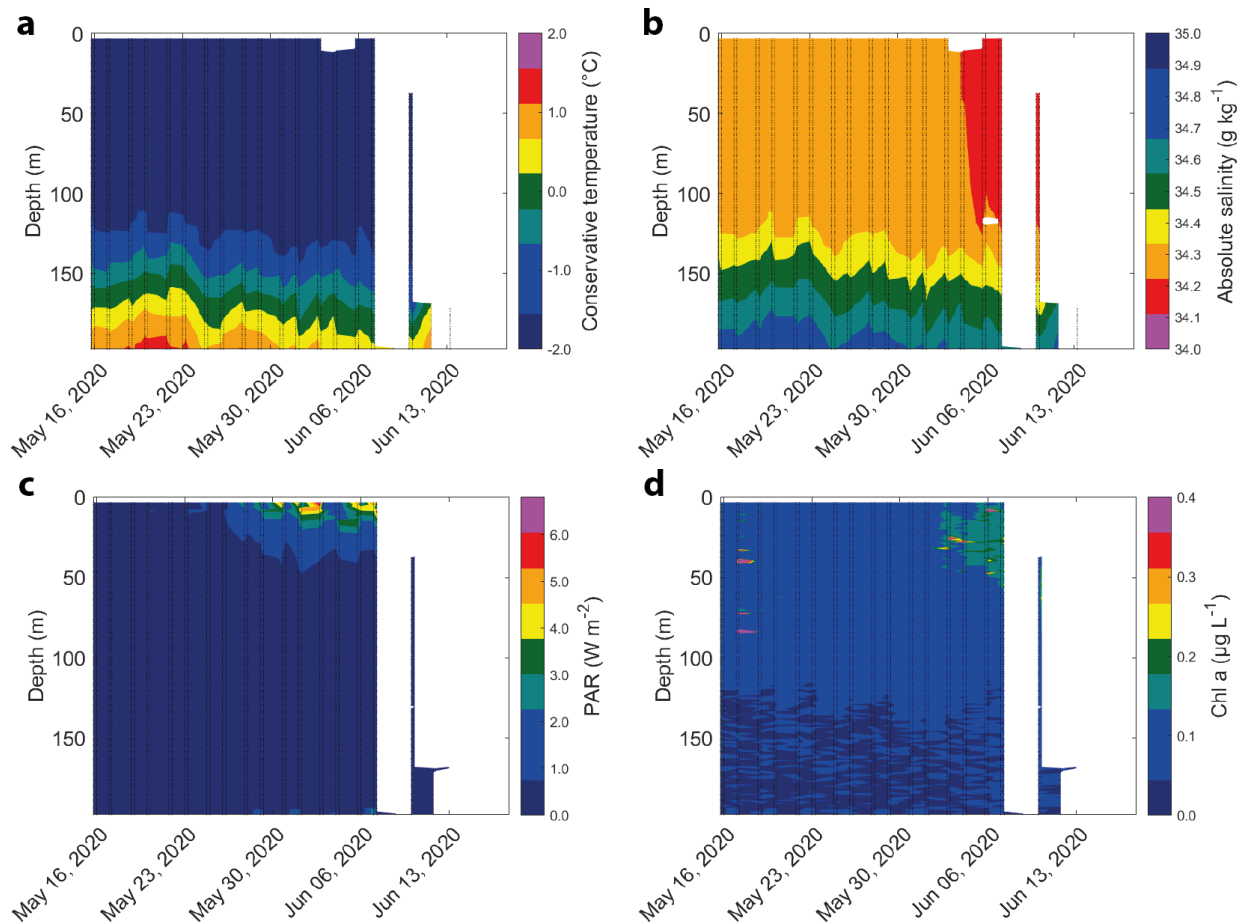
Figure 18. Ocean properties late May to early June, observed by Woods Hole Ice-tethered Profiler #94 at site L2.

Vertical sections are shown during the absence of manual observations for a) conservative temperature, b) absolute salinity, c) photosynthetically active radiation (PAR) and d) chlorophyll *a* (Chl *a*) based on fluorescence measurements and manufacturer's calibration (d); see Figure 12 for citations for TEOS10 conservative temperature and absolute salinity. Observed data locations are denoted by small black dots, and the contours are based on linear interpolation in the horizontal. Large gaps in observations are left blank; in early to mid-June the shallow topography likely led to the cable of the Woods Hole Ice-tethered Profiler at site L2 dragging across the seafloor and slanting from vertical, impeding the system from capturing full profiles. The interpolated, contoured section for Chl *a* in panel d reflects the actual point values (not shown). The data can be found under Toole et al. (2016).
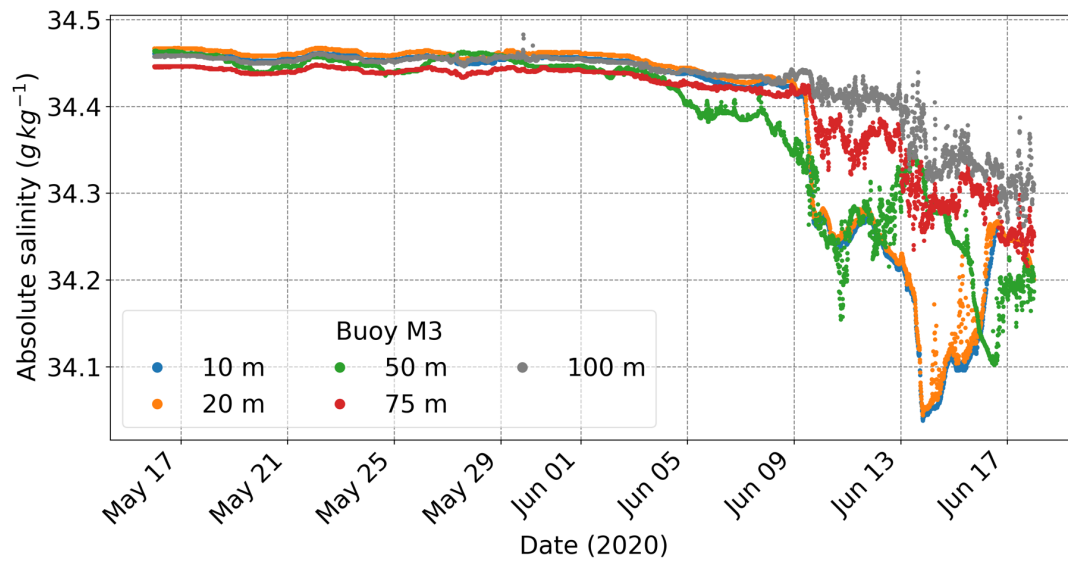
Figure 19. Absolute salinity at discrete depths at site M3 from late May to early June.
The observations are by the same type of instrument as in Figure 13 but shown for May 16–June
18, 2020, with depths denoted by color, as shown in the legend. The data are from Salinity Ice
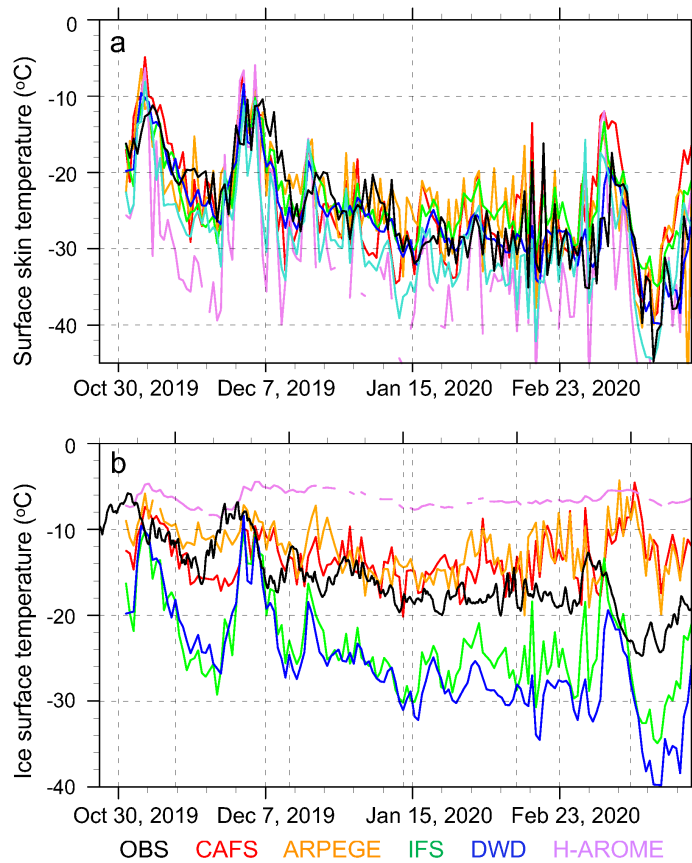Tether buoys (Hoppmann et al., 2022b).

Figure 20. Comparison of wintertime observations and 2-day forecasts during October 15, 2019–March 15, 2020.

Observations (OBS, black lines) of a) skin temperature and b) surface ice temperature, averaged across the L sites and the Central Observatory meteorological installation, and compared to 2-day forecasts at the location of RV *Polarstern*. Forecasts systems (color-coded) shown: NOAA-PSL Coupled Arctic Forecast System (CAFS; red), Météo-France ARPEGE-GELATO forecast system (ARPEGE; orange), ECMWF Integrated Forecast System (IFS, green), German Weather Service forecast system (DWD; blue) and HARMONIE--AROME (H-AROME; purple). Details of these systems can be found in Solomon et al. (2023) and references therein.

2298　Tables and full captions

2299

2300

Table 1. Types of autonomous buoy systems used during MOSAiC.

Buoy type (abbreviation)[a]	Reference	Buoy label[b]
Light strings (OptiCAL; formerly Envipope/LITO)	Schartmüller et al. (2023)	E buoy
Autonomous Ocean Flux Buoy (AOFB)	Stanton et al. (2012)	F buoy
Seasonal Ice Mass Balance buoy (SIMB3)	Planck et al. (2019)	I buoy
Bruncin-type Ice Mass Balance buoy with additional sensors (IMB-flex)	—[c]	M buoy
Salinity Ice Tether (SIT) with CTD	Hoppmann et al. (2022a)	O buoy
Position-tracking buoys (surface velocity profilers/ice trackers) of various types (SVP-B, IceTracker, iSVP, SVP-BT, Calib)	Bliss et al. (2023)	P, C buoy
Spectral radiation station and bio-optical buoys (Spectral Radiation Station, RITBOB); sometimes with additional instrumentation	Tao et al. (n.d.)	R buoy
Snow buoy (Snow Buoy)	Nicolaus et al. (2021a)	S buoy
Snow Ice Mass Balance Apparatus (SIMBA)	Jackson et al. (2013)	T buoy
UpTempO (UpTempO)	University of Washington (2024)	U buoy
Drift-Towing Oceanic Profiler (DTOP)	Li et al. (2021a)	V buoy
Woods Hole Ice-Tethered Profiler (WHOI ITP, WHOI BIO-ITP, WHOI ITP-V)	Toole et al. (2011); Krishfield et al. (2008); Cole et al. (2015)	W buoy
Atmospheric Surface Flux Station (ASFS)	Cox et al. (2023a)	—[d]
Dynamic Ocean Topography (DOT) Buoy	Lee et al. (2022)	—[d]
Unmanned (uncrewed) Ice Station (UMIS_PRIC_Ice, UMIS_PRIC_Ocean)	Lei et al. (2022)	—[d]
Acoustic Zooplankton Fish Profiler (AZFP) buoy	Flores et al. (2023)	—[d]
Light harp (light harp)	—[c]	—[d]
Salt harp (salt harp)	Notz et al. (2005)	—[d]
First Institute of Oceanography fixed-level buoy (FIO FLB)	—[c]	—[d]
Second Institute of Oceanography sediment trap (SIO sediment trap)	—[c]	—[d]

2302
2303
2304
2305
2306

---

[a] Technical name by users/manufacturer; see Table S1 for detailed descriptions of the variables measured by each type, and Table S2 for a full list of buoys and their labels, where appropriate
[b] Nomenclature on meereisportal.de, distinguished by single letters in the label
[c] Citations for these buoys are not yet available, as they include novel technology
[d] Buoys without a label have not been available in near-real time through the seaiceportal.de, although some have been provided at other portals.

2307 **Table 2. Mean values of downwelling longwave radiation (LW$_d$), near-surface air**

2308 **temperature (T$_a$), and net surface energy flux (F$_{atm}$) measured[a] at 4 sites in the Distributed**

2309 **Network December 20, 2019–January 19, 2020.**

Site	LW$_d$ (W m^{-2})	T$_a$ (°C)	F$_{atm}$ (W m^{-2})[b]	Ice thickness (m)[c]	Snow depth (m)[c]	Initial distance to Central Observatory (km)[d]
"Met City" at Central Observatory (6 m height Ta):	172.1	−27.5 [e]	−29.0	—[f]	—[f]	<1
L1 (2 m height T$_a$):	171.4	−27.7	−27.9	1.10	0.072	15
L2 (2 m height T$_a$):	172.8	−27.8	−26.8	1.27/1.54[g]	0.038/0.035[g]	12
L3 (2 m height T$_a$):	173.2	−27.5	−29.2	1.27	0.040	22

2310

[a] LW$_d$ and T$_a$ are from the time series in Figure 8a and b; F$_{atm}$ is from the same instrument system (not shown in the figure).
[b] Heights of measurements contributing to F$_{atm}$ are considered unimportant, as all were within the atmospheric surface boundary layer.
[c] Mean values based on the time series shown in Figure 11 for sites L1–L3
[d] On December 20, 2019
[e] Value may not be comparable to values at the L sites, as it was measured at a different height.
[f] No autonomous observations of ice thickness and snow depth available close to the "Met City" installations
[g] Values are from two buoys at site L2.

2311 *Supplementary material for*

2312 **The MOSAiC Distributed Network: observing the coupled**
2313 **Arctic system with multidisciplinary, coordinated**
2314 **platforms**

2315
2316 **Text S1. Further details on the planning process of the Distributed Network**

2317 The originally planned layout had considered the radially distributed network of sites around RV
2318 *Polarstern* ("PS" in Figure S1), with a corridor for logistics access by supply vessels (gray shading
2319 in Figure S1) with only few buoy sites and none of the heavily instrumented L sites. The position-
2320 tracking buoys (labels starting with "P" in Figure S1) had been clustered around RV *Polarstern*
2321 and each of the M and L sites. One M site ("MF") at 40 km distance to RV *Polarstern* had been
2322 planned, in addition, to capture conditions far away from the Central Observatory and the core of
2323 the distributed sites. This arrangement had been projected prior to the expedition onto satellite
2324 images of the larger region, including situations where marginal-ice-zone condition dominated,
2325 around the planned deployment of the MOSAiC Central Observatory (Figure S2). Further details
2326 of how floes were identified directly before buoy deployment in the field, using advanced products
2327 from satellite observations, can be found in Krumpen and Sokolov (2020).
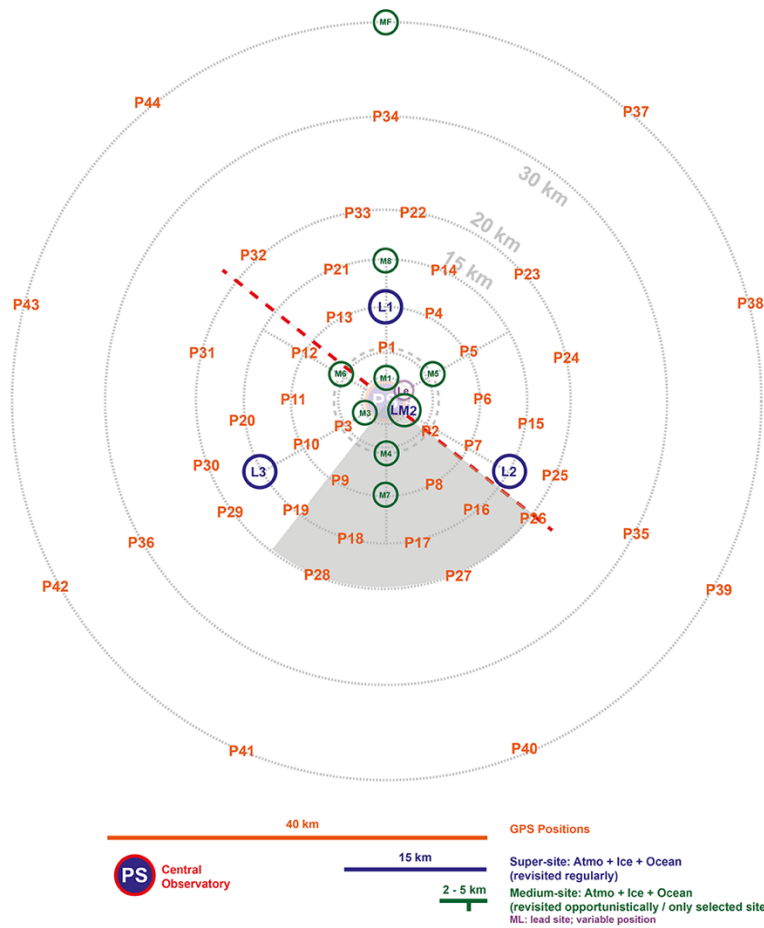
Figure S1. Planned layout of the DN prior to deployment in October 2019.
The different site types are distinguished by color as shown in the legend: L sites (blue), M sites (green) and P sites (orange). The Central Observatory with RV *Polarstern* is located in the centre, where the ship's assumed orientation is along the red dashed line. The gray shaded area denotes the logistics corridor planned for approach of supply ships.
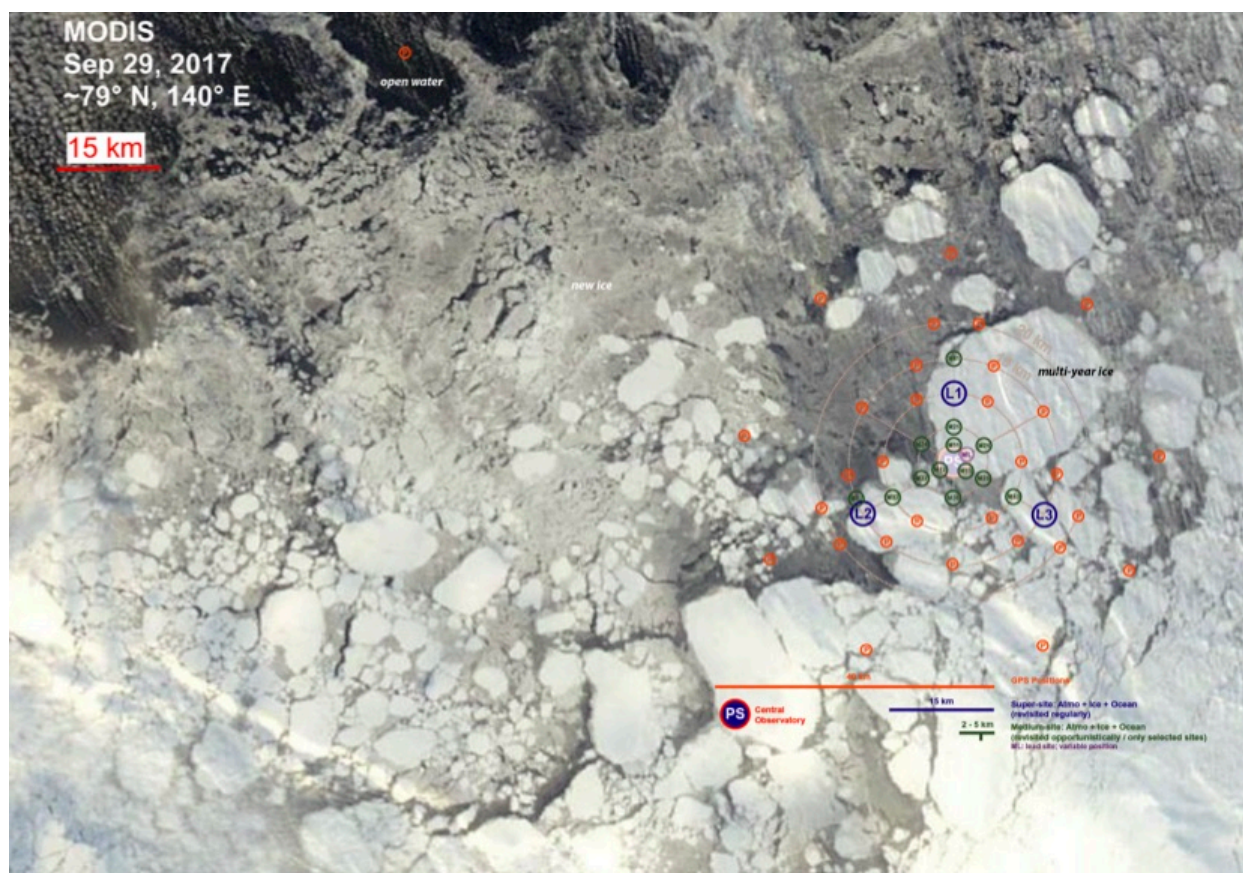
2334
2335 **Figure S2. A modified version of the layout from Figure S1 projected onto a satellite image.**

2336 The sites were adjusted to fit the ice conditions in the marginal ice zone captured in this satellite

2337 image from MODIS, taken on September 29, 2017 around 79 N and 140 E. (NASA, 2017).

2338

2339

Table S1. Extended description of autonomous (buoy) system types as used during

MOSAiC.

Buoy Type (abbreviation)[a]	Variable / measurement	Reference[b]	Buoy Label[c]
Light strings (OptiCAL; formerly Envipope/LITO)	Global Positioning System (GPS) position; light measurements at three wavelengths, chlorophyll a fluorescence	Schartmüller et al. (2023)	E buoy
Autonomous Ocean Flux Buoy (AOFB)	GPS position; eddy correlation fluxes of heat salt and momentum at 3 m depth, temperature, conductivity and salinity at 3 m depth, water velocity components every 2 m to 80 m depth, GPS position, 50 m depth thermal diffusivity	Stanton et al. (2012)	F buoy
Seasonal Ice Mass Balance buoy (SIMB3)	GPS position; sea ice thickness & snow depth (calculated from ultrasonic pingers), air, snow, ice and ocean temperatures at 0.02 m vertical spacing (thermistor chain)	Planck et al. (2019)	I buoy
Bruncin-type Ice Mass Balance buoy with additional sensors (IMB-flex)	GPS position; barometric pressure; hull temperature and humidity; Optional: C*hlorophyll a* & CDOM fluorescence, optical backscatter at 700 nm; ocean temperature, salinity, and pressure (SBE37 MicroCat); dissolved oxygen; air, snow, ice & ocean temperatures at 0.02 m vertical spacing (thermistor chain); camera images	—	M buoy
Salinity Ice Tether (SIT) with CTD	GPS position; T/S/P (SBE37 Microcat), surface temperature	Hoppmann et al. (2022a)	O buoy
Positioin-tracking buoys (surface velocity profilers / ice trackers) of various types (SVP-B, IceTracker, iSVP, SVP-BT, Calib)	GPS position. Optional: barometric pressure, surface temperature	Bliss et al. (2023)	P, C buoy
Spectral radiation station and bio-optical buoys (Spectral Radiation Station, RITBOB); sometimes with additional instrumentation	GPS position; barometric pressure; hull temperature & humidity; shortwave spectral radiation (incident, reflected, and transmitted). Optional: *Chlorophyll a* & CDOM fluorescence, optical backscatter at 700nm; ocean temperature, salinity, and pressure (SBE37 MicroCat); dissolved oxygen; air, snow, ice & ocean temperatures at 0.02 m vertical spacing (thermistor chain); WRGB light transmission at 0.05 m vertical spacing (light chain); camera images. Some units without telemetry	Tao et al. (n.d.)	R buoy

[a] Technical name by users/manufacturer; see Table S1 for detailed descriptions of the variables measured by each type, and Table S2 for a full list of buoys and their labels, where appropriate

[b] Citations for some of these buoys are not, yet, available, as they include novel technology

[c] Nomenclature on meereisportal.de, distinguished by single letters in the label. Buoys without a label have not been available in near-real time through the seaiceportal.de, although some have been provided at other portals

Table S1 continued.

Buoy (Type)	Variable / measurement	Reference	Buoy Label
Snow buoy (Snow Buoy)	GPS position; snow depth (4x), air temperature (1.5m), barometric pressure	Nicolaus et al. (2021a)	S buoy
Snow Ice Mass Balance Apparatus (SIMBA)	GPS position; air, snow, ice & ocean temperatures at 0.02 m vertical spacing (thermistor chain)	Jackson et al. (2013)	T buoy
UpTempO (UpTempO)	GPS position; ocean state (T/P) at different depths	University of Washington (2024)	U buoy
Drift-Towing Oceanic Profiler (DTOP)	GPS position; ocean state (T/S), surface meteorology (P/T/q), optional chlorophyll a, dissolved oxygen, ice T profile.	Li et al. (2021a)	V buoy
Woods Hole Ice-Tethered Profiler (WHOI ITP, WHOI BIO-ITP, WHOI ITP-V)	GPS position; ocean state (T/S/P), dissolved oxygen; optional: *Chlorophyll a* and CDOM fluorescence, optical backscatter at 700nm; ocean current velocity	Toole et al., (2011); Krishfield et al. (2008); Cole et al. (2015)	W buoy
Atmospheric Surface Flux Station (ASFS)	GPS position; surface meteorology (P, T, RH, winds), broadband radiative fluxes, surface turbulent heat fluxes, surface net heat flux, surface height change, surface skin temperature	Cox et al. (2023a)	—
Dynamic Ocean Topography (DOT) Buoy	GPS position; barometric pressure, temperature, sea surface height, pressure at 1m depth.	Lee et al. (2022)	—
Unmanned (uncrewed) Ice Station (UMIS_PRIC_Ice, UMIS_PRIC_Ocean)	GPS position; snow depth, ice thickness, snow-ice temperature profile, spectral radiation at 6 layer from upper surface to the water under the ice; ocean: conductivity and temperature of upper ocean at 5 fixed layer to 40 m under the ice, and dissolved oxygen/chlorophyll a at 5 and 20 m under the ice	Lei et al. (2022)	—
Acoustic Zooplankton Fish Profiler (AZFP) buoy	GPS position; barometric pressure, internal temperature and humidity; incoming broadband radiation, AZFP acoustic backscatter at 4 frequencies, chlorophyll a fluorescence, optical backscatter, webcam images	Flores et al. (2023)	—
Light harp (light harp)	Temperature, light (incoming and outgoing) in ice	—	—
Salt harp (salt harp)	Salinity in ice	Notz et al. (2005)	—
First Institute of Oceanography fixed-level buoy (FIO FLB)	GPS position; ocean state (T/S/P) at different depths		—
Second Institute of Oceanography sediment trap (SIO sediment trap)	collection of sediment samples, position	—	—

Text S2. Implementation of the mDN

In autumn 2020 the mDN was installed along the transit of RV *Polarstern* as it moved back northward into the central Arctic as well as in and around a new Central Observatory. This mDN was much less instrumented than the original DN and focused on detailed studies of surface re-freezing and new ice formation to characterize the transition from the summer melt season into freeze-up. This included snow thickness changes after initial freeze-up. Most buoys were installed within the Central Observatory and recovered towards the end of the drift with RV *Polarstern* by September 20, 2020. As the DN, the remaining buoys of the mDN continued reporting, drifting into the North Atlantic as late as summer 2022, the last one transmitting until September 2023 (2020P220).

The larger-scale mDN consisted of two Snow Buoys and eight position-tracking buoys with barometric pressure. These units were deployed on remote ice floes during the transits to (August 16 to 23, 2020) and from (September 21 to 30, 2020) the last implementation of the Central Observatory (Fgure S3a). A small-scale mDN was established around the main ice camp of this Central Observatory (Figure S3b, c and d) where 22 ice drifters were deployed, 10 of the drifters within 1 km of the ship, and the other 12 in equal amounts at about 4.5 km, 9 km, and 28 km distance to the ship. Within the Central Observatory, the devices were installed across different surface types, e.g., ridges, melt ponds, leads, or bare ice, to enable comparative studies of level and deformed ice and different types of freezing water surfaces. These installations consisted of five IMBs, four Snow Buoys, two radiation stations equipped with spectral radiometers, one Salinity Ice Tether buoy (Conductivity Temperature Depth), a twin-buoy setup equipped with an Acoustic Zooplankton Fish Profiler and a suite of complementary biooptical sensors. A recovered Autonomous Ocean Flux Buoy was partially re-deployed at the Central Observatory. Atmospheric Surface Flux Station #50 and Atmospheric Surface Flux Station #30 were deployed near a lead and within a melt pond, respectively, obtaining energy budgets during freeze-up over surfaces different from the main Central Observatory meteorological installation during this important transition period. Three position-tracking buoys were deployed in a triangle around an eddy covariance system installed close to a ridge. These mDN deployments provide a distributed network of observations that has a scale smaller than the original DN, and are also given in Table S2.

Figure S3. Positions of the main sites of the Distributed Network during the final leg.
Position of the buoys in the second ("mini") implementation of the Distributed Network (mDN) on September 19, 2020. (a) shows the buoys deployed enroute to the site (red triangles) and the northernmost buoys remaining from the initial Distributed Netowork (gold circles). The blue star marks the location of the RV *Polarste*rn. (b)–(d) show progressively smaller scales, with the boundaries of each panel marked by the blue dashed line in each prior panel.

Text S3. Drift trajectories for each site

For some sites, data sets from different buoys / sources were merged. While, by design, the drift and position of each P site are provided by the one buoy at each site (Bliss et al., 2022, 2023), the drift trajectory and position of all L and M sites are defined by merging the time series of selected buoys at each site (as in Nicolaus et al. 2021b). Data source names are consistent with the short names of sensor.awi.de and meereisportal.de, as well as with the tables in the MOSAiC cruise reports. In addition, the unique International Mobile Equipment Identity (IMEI) number is given. The original measurement frequency also depends on the platform technical properties and varies between 1 s and 1 h. The resulting data set is interpolated to hourly position data. The end dates given in Table S3 refer to the last position reported by the buoy. While all buoys were deployed on sea ice, most buoys melted out of the ice during their drift and continued in the open ocean. Hence, positions are not necessarily sea ice drift / positions. The selection of the formal position of each site was based on the following criteria:

- Length of the time series: The aim is to cover the entire time series until the last unit stopped reporting positions
- Frequency of measurements: Higher frequency is preferred, as the final data product was chosen to have a temporal resolution of 1 hour, which was the reporting interval of most units

Table S2. Autonomous (buoy) system deployments during MOSAiC, explained in Text S4.

The table is provided as an Excel file.

Text S4. Explanatory text related to Table S2.

For some sites, data sets from All buoy deployments are listed by the buoy label (meereisportal.de), buoy type, and date and site of deployment. The sites are given as "CO" (Central Observatory), "L1–L3", "M", "LM" for the DN; and "mDN" for the Central Observatory mDN deployments. Note that several platforms were recovered and then redeployed, denoted as a new deployment. The Buoy Type is defined in Tables 1 and S1. Where available, other buoy labels, such as labels given by the respective PI, are given under "Original Buoy Label". Several buoys labelled starting with "P" and "U" were not deployed at one of the main sites but stand-alone on separate ice floes; here, no site labels are given, and the reader is referred to Bliss et al. (2023). Several buoys did not have telemetry and are listed as "local storage" under "IMEI", though several did have radio links to transmit a subset of the data to the ship, such as the Atmospheric Surface Flux Station. Note that IMEI usually end on "0"; those listed with "1" or "2" at the end are internal numbers denoting the first and second redeployment of each buoy instrument package, respectively. A few buoys were not displayed in the meereisportal.de and, hence, do not have a corresponding buoy label. DN sites labelled starting with "Ak" were part of the DN extended network (Figure 1) and are not detailed further here.

2425 **Table S3. Data sources of the drift trajectories for each site[a].**

Site[b]	Operational time range	IMEI[c] number	Data source	f[d]	Reference
CO1	October 4 2019 – April 23, 2020	—[e]	RV *Polarstern*	1 s	Rex (2020), Haas (2020), Kanzow (2020)
CO1	April 23, 2020 – November 11, 2020	300234068210310	2020P225	1 h	Lei et al. (2021a)
CO2	June 19, 2020 – June 26, 2020	—[e]	RV *Polarstern*	1 s	Rex (2021a), Rex (2021b)
CO2	June 26, 2020 – August 19, 2020	300025010649550	2020M26	1 h	Granskog et al. (2020)
CO3	August 21, 2020 – August 28, 2020	—[e]	RV *Polarstern*	1 s	Rex (2021b)
CO3	August 28, 2020 – August 9, 2021	300234068066320	2020O10	10 min	Hoppmann et al. (2021d)
L1	October 5 2019 – August 6, 2020	300234068704730	2019T67	30 min	Lei et al. (2021b)

---

[a] The full drift data set can be found under Nicolaus et al. (2021b).
[b] "CO1", "CO2" and "CO3" are used in the drift data set to denote different implementations of the Central Observatory, so that CO1 and CO2 were part of the first Distributed Network (DN), whereas CO3 was part of the second ("mini") implementation of the Distributed Network (mDN)
[c] International Mobile Equipment Identity
[d] Original measurement frequency
[e] The ship is not an autonomous buoy and does not have an IMEI

L2	October 7 2019 – August 18, 2020	300025010524990	2019W2	1 h	Toole et al. (2016)
L3	October 11 2019 – August 7, 2020	300234066081170	2019S94	1 h	Nicolaus et al. (2020b)
LM	October 29 2019 – August 14, 2020	300234068706330	2019T66	30 min	Lei et al. (2021c)
M1	October 5 2019 – May 9, 2020	300234067068380	2019V1	1 h	Li et al. (2021b)
M2	October 7 2019 – August 9, 2020	300234067064490	2019V2	1 h	Li et al. (2021c)
M3	October 7 2019 – August 3, 2020	300234066444880	2019S81	1 h	Nicolaus et al. (2020a)
M4	October 8 2019 – August 14, 2020	300234068166760	2019O4	10 min	Hoppmann et al. (2021a)
M5	October 9 2019 – August 17, 2020	300234067066520	2019V4	1 h	Li et al. (2021d)
M6	October 10 2019 – August 13, 2020	300234068514740	2019O6	10 min	Hoppmann et al. (2021b)
M7	October 11 2019 – October 25 2019	300234068519770	2019O7	10 min	Hoppmann et al. (2021c)
M8	October 11 2019 – September 29, 2020	300234068700320	2019T69	1 h	Lei et al. (2021d)

2426

2427

2428
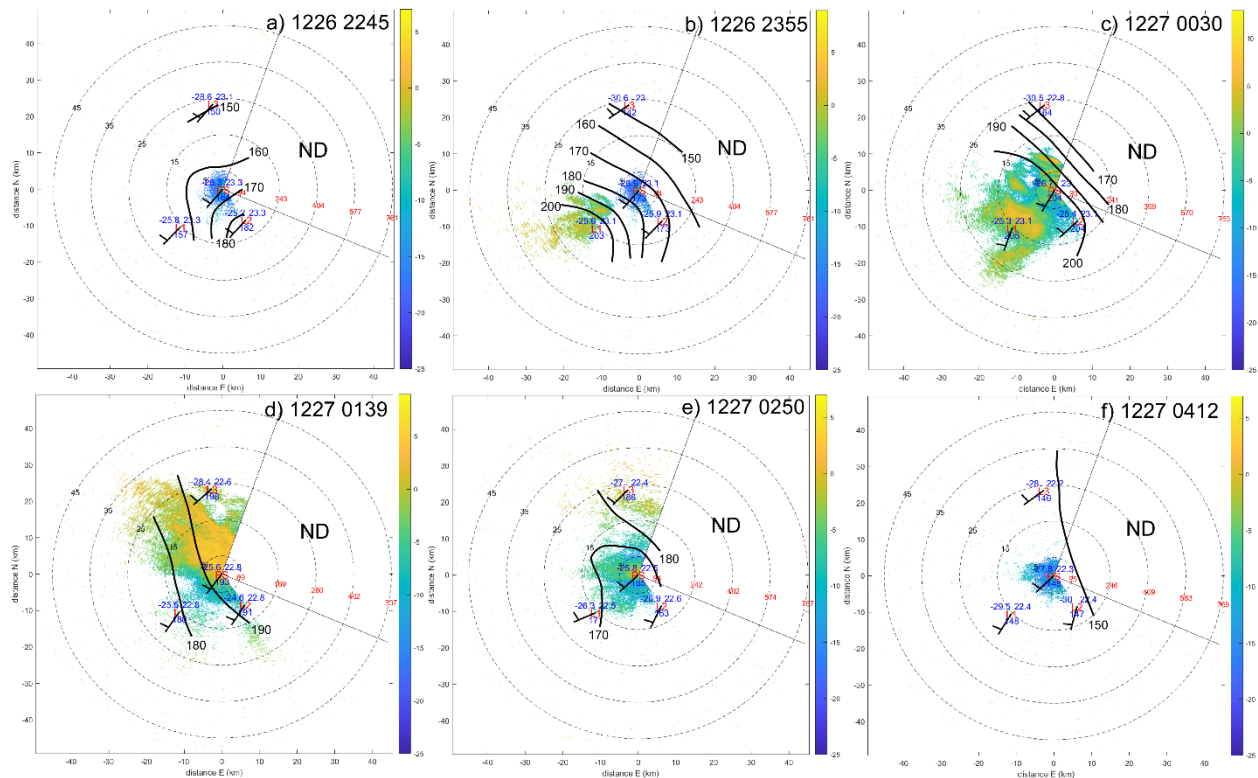
Figure S4. Radar reflectivity intensity (dBz) from the scanning Ka-band Doppler radar.
The maps are at the six times shown in Figure 9 (Date & time shown in upper right). The L sites are indicated, while RV *Polarstern* (PS) is located at the center of each figure (note that the meteorological installations in the Central Observatory, "Met City", are <500 m from PS). The near-surface observations of air temperature, surface pressure, LW_d, and wind speed / direction are given at each of these surface sites. The isopleths show the analysis of the LW_d field (isopleth interval 10 W m^{-2}) based on these observations. The range from the radar (black numbers; km) is shown by the dashed concentric circles, which are also labeled by the height above the local surface (red; meters). Radar data was not obtained in the delineated sector to the northeast labeled "ND". A signal-to-noise threshold of –10 dB is used for the reflectivity. The scanning Ka-band radar was operated by the United States Department of Energy Atmospheric Radiation Measurement program and was able to obtain meaningful radar reflectivity measurements of even fairly shallow clouds to a range of approximately 35 km using elevation angles <1°. These radar volumes were obtained every approximately 12 minutes and approximately covered the domain of the Distributed Network (DN) at a resolution of about 100 m. The spatial scales shown by the scanning radar data aids in upscaling atmospheric forcing parameters from variables measured at the DN sites.

105
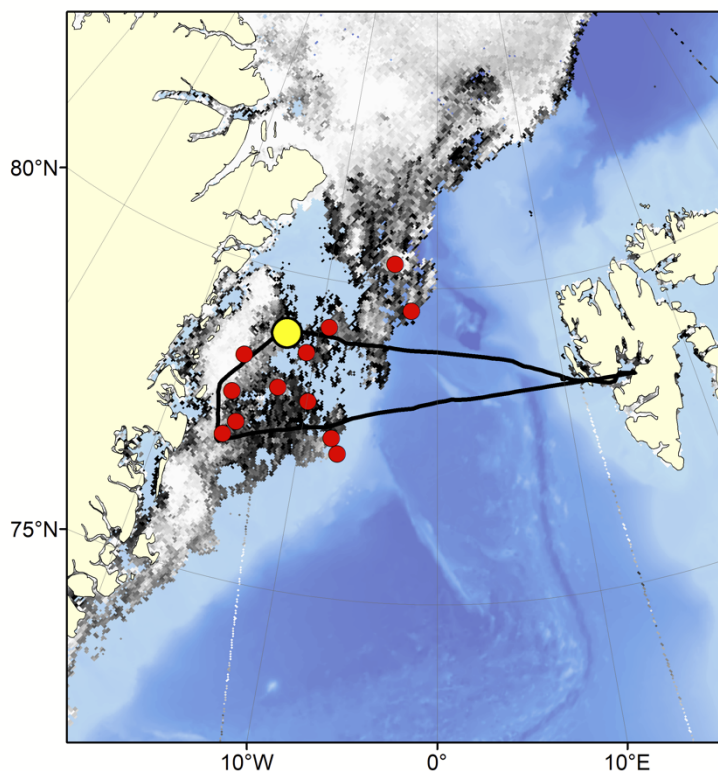
Figure S5. Map with the flight path of Polar 6 on September 2, 2020.

The red dots indicate the position of active buoys from the MOSAiC DN. The yellow dot indicates the position of the icebreaker *Kronprins Haakon* (NPI) that was carrying out sea ice and oceanographic surveys in Fram Strait. The flights were part of the MOSAiC IceBird Campaign (Belter et al. 2021, Herber et al. 2021).
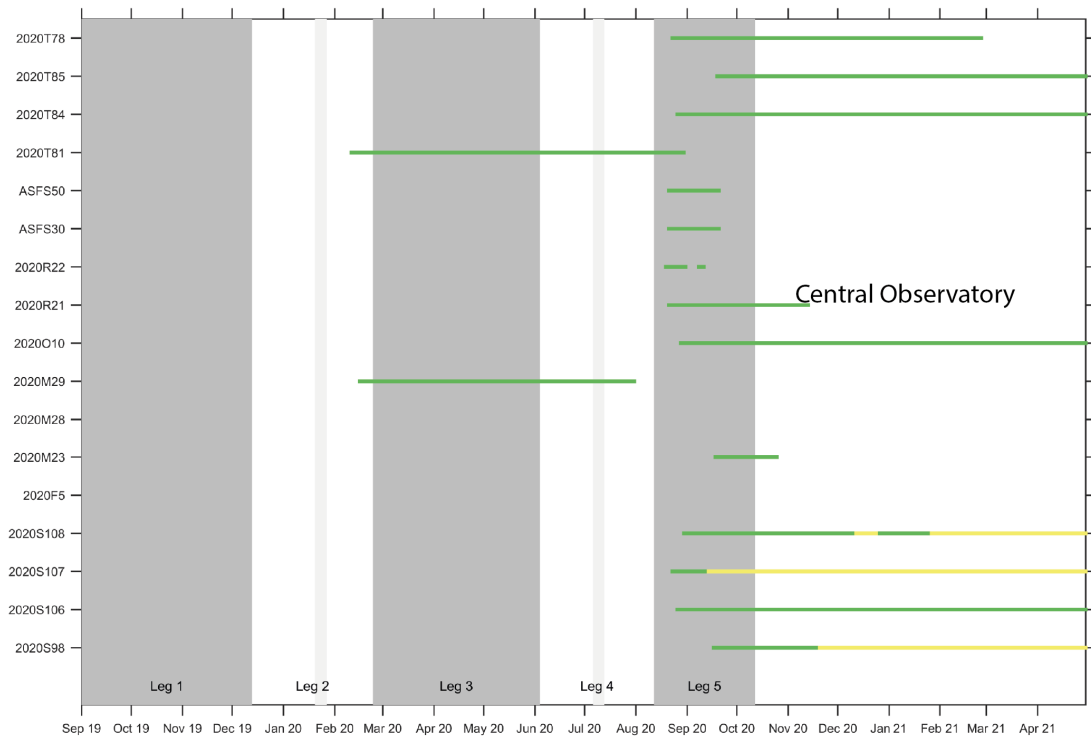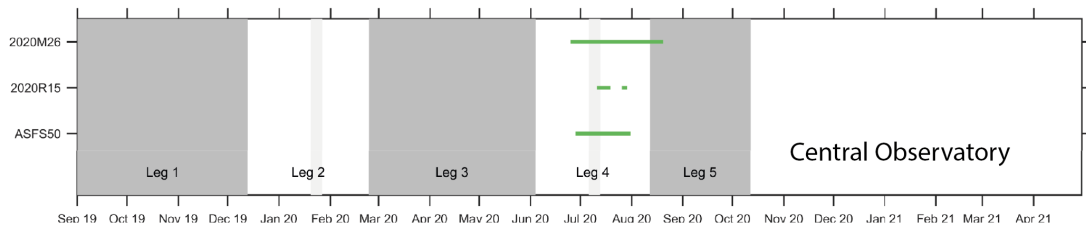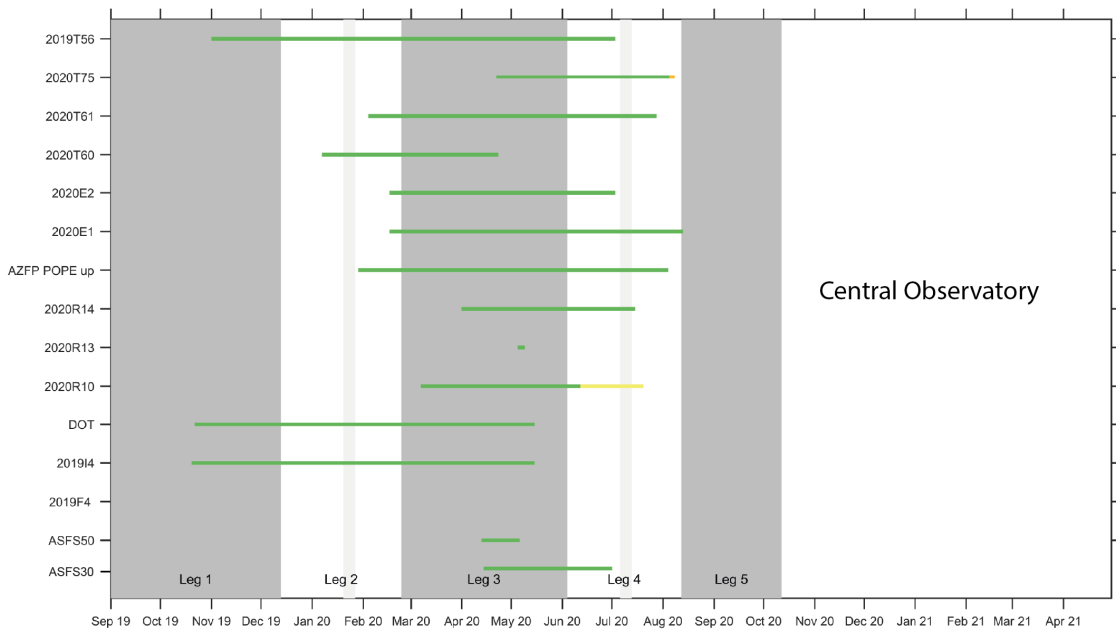
2453

2454 **Figure S6: Status of observational buoys in the implementations of the Distributed**
2455 **Network against time.**
2456 The charts are arranged by site (L1–L3, LM and Central Observatory) and category. The status
2457 of each system is shown in color: all functioning optimally (green), partly functional (yellow) and
2458 position-only (orange). Note that the three panels for "Central Observatory" refer to the time
2459 before RV *Polarstern* left for resupply (CO1 in Table S3), after return of RV *Polarstern* until most
2460 of the DN was dismantled in Fram Strait (CO2) and the time after relocation of the Central
2461 Observatory to the central Arctic in late summer (CO3). The buoy label is given on the y-axis,
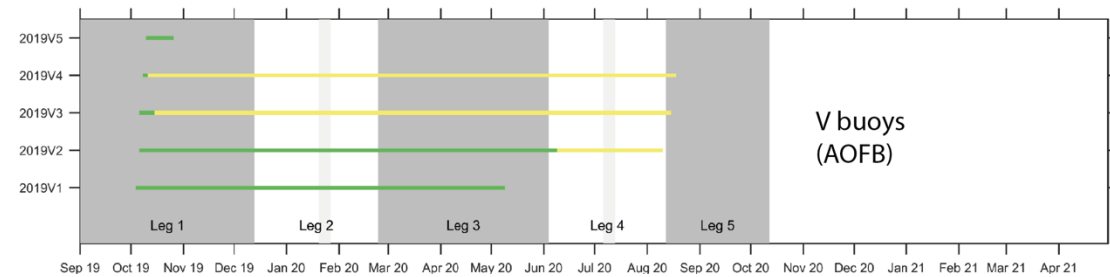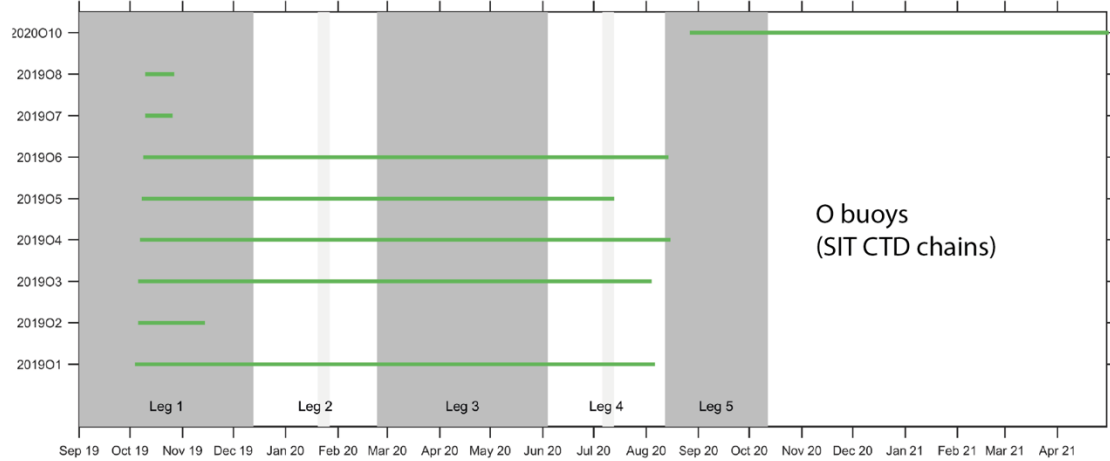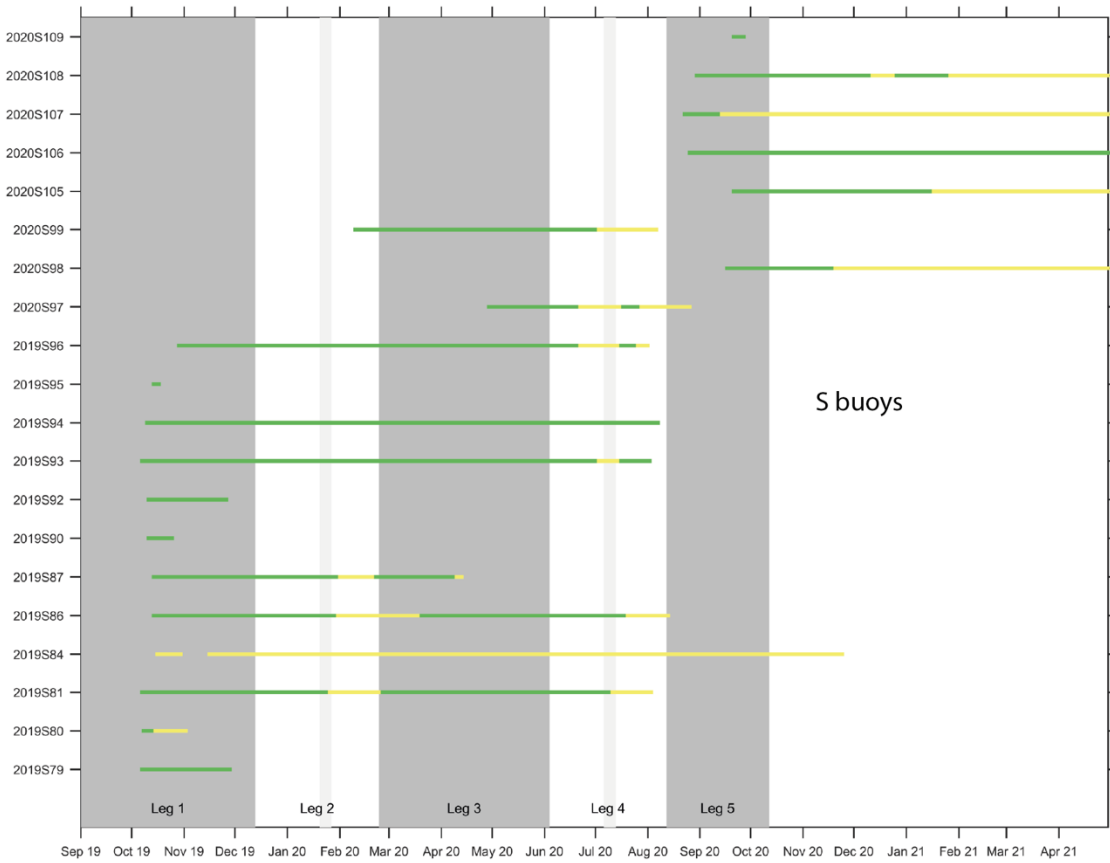2462 the month and year in abbreviated form on the x-axis.

2463

Figure S5 continued.

110
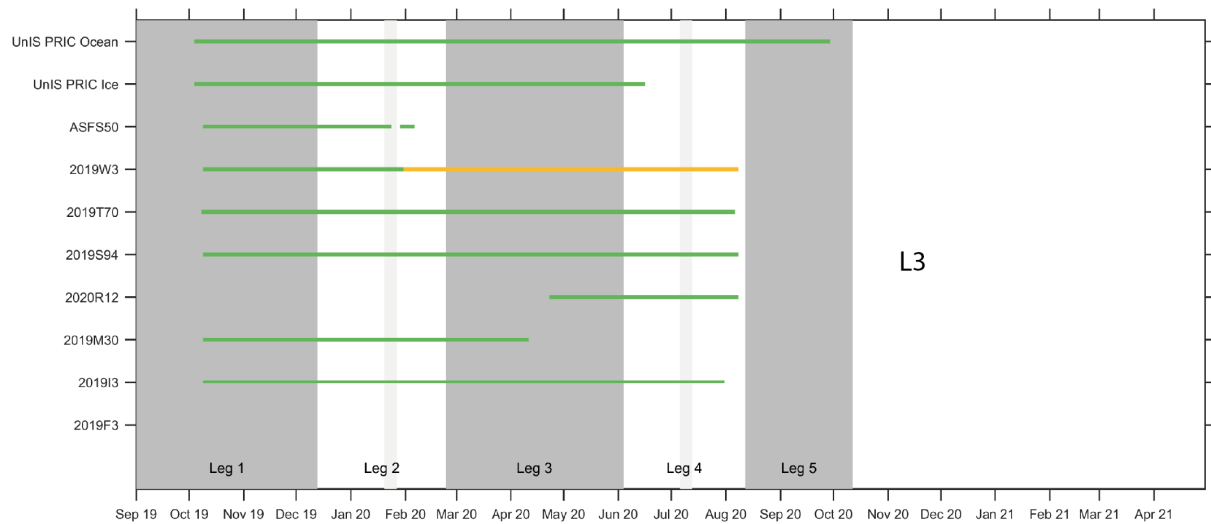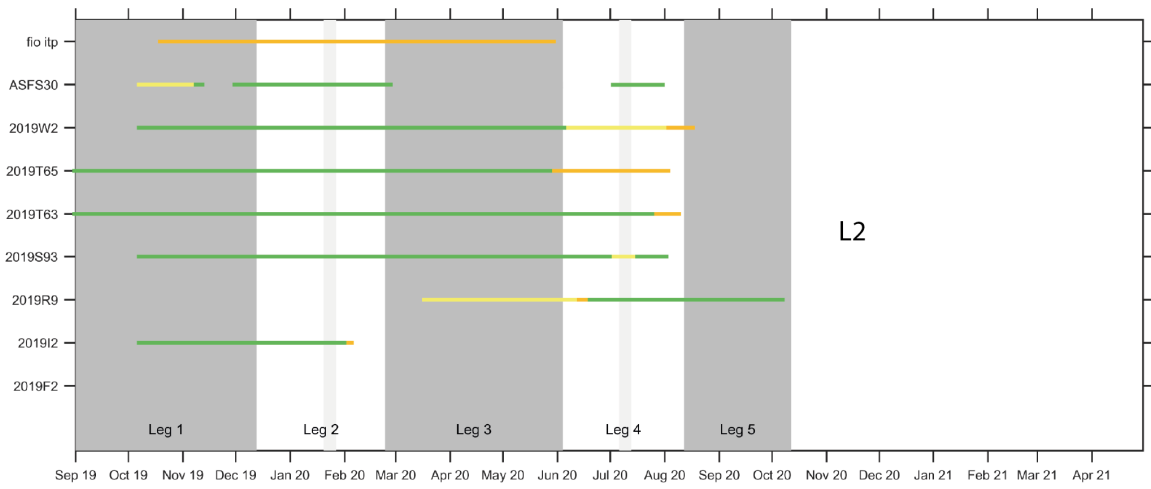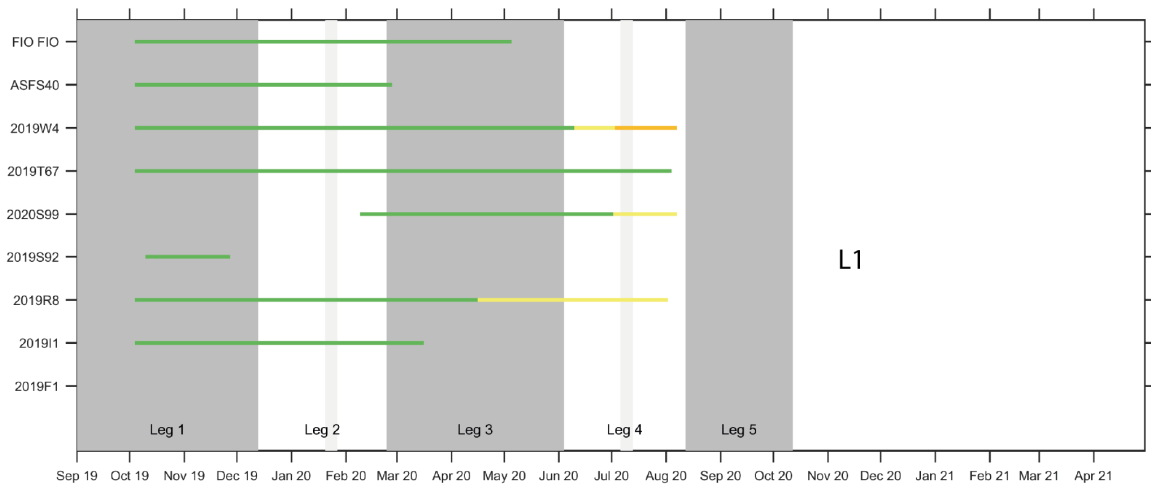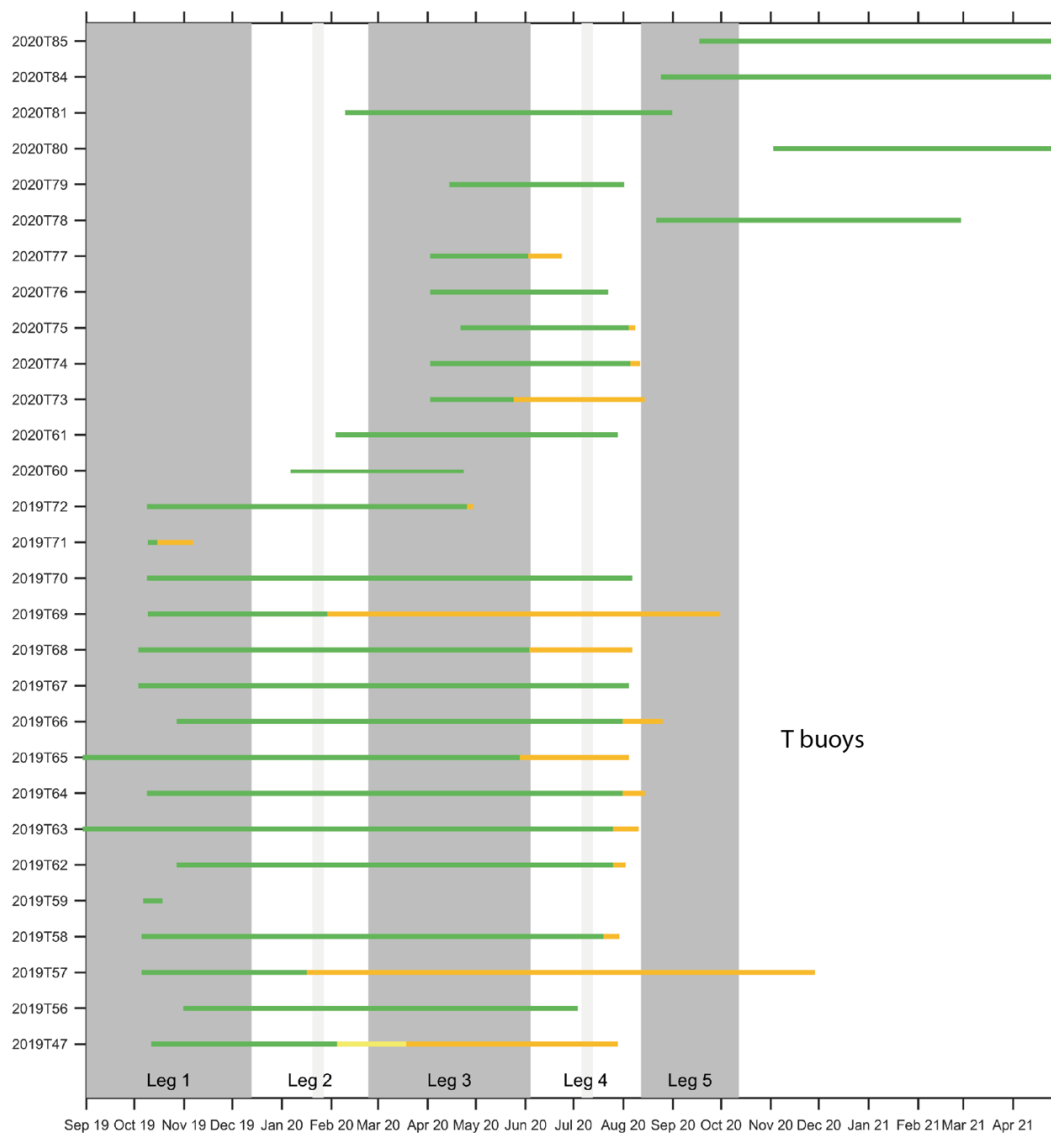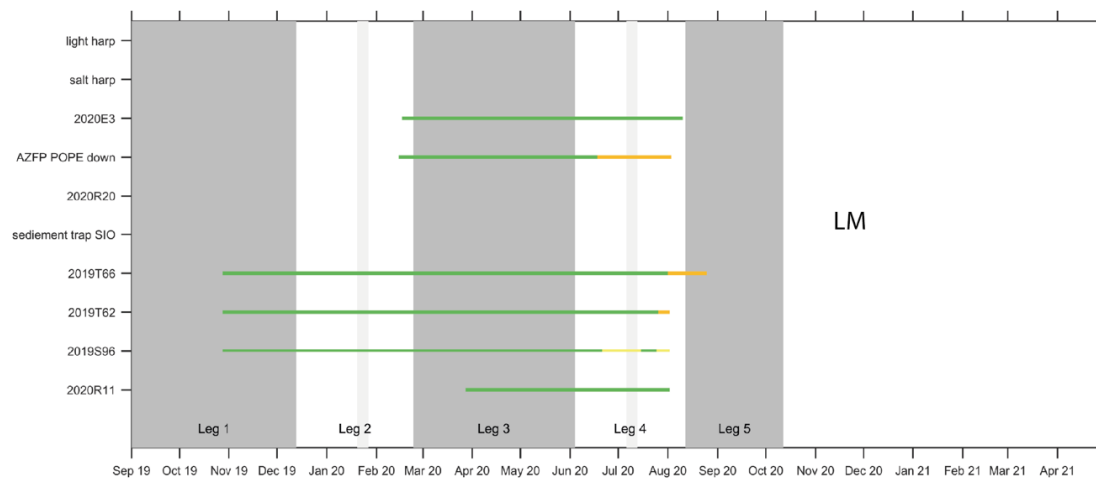
2465

2466   **Figure S5 continued** .

2467

Figure S5 continued.

2469 ## References

2470 *See main manuscript reference list.*